

From galaxies to the cosmic web and back: the interplay of different scales in galaxy formation and cosmic reionization

Dissertation
zur
Erlangung des Doktorgrades (Dr. rer. nat.)
der
Mathematisch-Naturwissenschaftlichen Fakultät
der
Rheinischen Friedrich-Wilhelms-Universität Bonn

von
Enrico Garaldi
aus
Modena

Bonn, Oktober 2018

Angefertigt mit Genehmigung der Mathematisch-Naturwissenschaftlichen Fakultät der Rheinischen Friedrich-Wilhelms-Universität Bonn.

1. Gutachter: Prof. Dr. Cristiano Porciani

2. Gutachter: Prof. Dr. Frank Bertoldi

Tag der Promotion: 11.10.2019

Erscheinungsjahr: 2020

– To Lisa, Alice,
Lorella and Maurizio

Abstract

The evolution of the Universe is primarily governed by gravity, that triggers the development of a complex web-like distribution of galaxies. The latter are embedded in larger structures, called haloes, mainly composed by an exotic form of matter that does not interact with light, and is therefore called dark. Within this cosmic web, astrophysical phenomena occur on a large variety of spatial scales. Although ubiquitous, the interaction between them is often neglected because of the difficulties in their simultaneous modeling. In this Thesis we employ advanced numerical simulations of structure formation in the universe to investigate three cases where this interplay is of primary importance, namely: the assembly bias, the radial acceleration relation and the epoch of cosmic reionization.

Assembly bias denotes the fact that dark matter haloes of the same mass have clustering properties that depend on their formation time. This effect is due to the cosmic environment of such haloes, that halts the accretion of new material in regions where the tidal field exerted by nearby structures is strong. Therefore, the assembly of objects strongly clustered is more efficiently suppressed. In this Thesis, we study the properties of satellite galaxies that reside within haloes with different assembly histories, and therefore cosmic environments. We show that their content is insensitive to the large-scale geometry of the matter distribution. However, the latter has a strong impact on the satellite dynamics, producing a preferentially-radial motion in objects embedded in a knot of the cosmic web, and isotropically-distributed velocities in region within filaments. We apply this knowledge to the satellites of the Milky Way and infer that our Galaxy must reside in a prominent filamentary structure.

Recent observations of a large sample of galaxies unveiled a tight correlation between the total radial acceleration experienced by bodies orbiting around the galactic center and the same quantity inferred only from the galactic baryonic content. Theoretical models of structure formation have been tested against this radial acceleration relation (RAR) only for large structures. Here, we predict for the first time the RAR of small satellite galaxies, opening up the possibility to test our knowledge of galaxy formation mechanisms in an uncharted territory. Additionally, we study the redshift evolution of this relation and its secondary dependence on physical properties of the satellites. We then make use of these results to devise an observational test that can distinguish between the standard cosmological model and one popular alternative theory, the Modified Newtonian Dynamics.

Finally, we study the role of quasars in the reionization of the Universe on the largest scales. We do so by simulating a reionization scenario where the ionizing photons production is dominated by quasars and compare it with one where galaxies are the main source of such photons. We show that, despite the peculiar emission properties of quasars, the former leads to global properties of the inter-galactic medium that are in agreement with observations. Additionally, we produce synthetic absorption spectra and use them to show that, in a quasar-dominated scenario, the properties of helium absorption features are incompatible with available observations. However, we also find indications that a modest contribution from quasars can explain the observed distribution of patches of inter-galactic neutral hydrogen. To unravel these apparently-controversial findings, we identify and investigate two promising methods that, using future observations, will enable a determination of the quasar contribution to cosmic reionization.

Contents

1	Introduction	1
1.1	The standard cosmological model	2
1.1.1	Content of the Universe	4
1.1.2	Problems of the Λ CDM model	6
1.2	Modified Newtonian Dynamics	7
1.3	Structure formation in Λ CDM	9
1.3.1	Dark matter collapse	10
1.3.2	Baryonic collapse	13
1.4	The epoch of cosmic reionization	13
1.4.1	Observational probes	14
1.5	Numerical simulations in astrophysics	19
1.5.1	Gravity	19
1.5.2	Hydrodynamics	21
1.5.3	Radiative transfer	22
1.5.4	Subgrid physics	24
1.5.5	Initial conditions	26
1.6	Open questions addressed in the Thesis	27
1.6.1	The impact of assembly bias on satellite galaxies	27
1.6.2	Prediction of the radial acceleration relation for Λ CDM satellite galaxies	28
1.6.3	The role of quasars in cosmic reionization	28
2	The effect of Halo Assembly on the Satellite Population	29
2.1	Introduction	29
2.2	Numerical Methods	30
2.3	Satellite evolution	33
2.3.1	Trajectories and dynamics	33
2.3.2	Shed material	37
2.4	Subhalo statistics	38
2.4.1	Mass and radial distribution	38
2.4.2	Gas and stellar content	40
2.4.3	Satellite mass fraction	42
2.5	Effects of halo assembly	43
2.5.1	Accretion time	45
2.5.2	Accretion pattern	45
2.5.3	Subhalo kinematic and anisotropy parameter	45
2.5.4	Satellite configuration	48
2.6	Conclusions	53

3	The radial acceleration relation of ΛCDM satellite galaxies	55
3.1	Introduction	55
3.2	Numerical simulations	56
3.3	Method	56
3.4	The RAR at redshift zero	58
3.5	Independency of the RAR on the satellite properties	59
3.6	Time evolution of the RAR	60
3.7	Conclusions	60
4	The effect of quasars on cosmic reionization	63
4.1	Introduction	63
4.2	Numerical Methods	64
	4.2.1 Hydrodynamical simulations	64
	4.2.2 Radiative transfer	65
4.3	Results	68
	4.3.1 Ionized fractions	68
	4.3.2 IGM temperature	72
4.4	Synthetic observations	73
	4.4.1 Effective optical depths	74
	4.4.2 The probability distribution function of optical depths	75
	4.4.3 The column-density ratio	81
4.5	Discussion and Conclusions	82
5	Final remarks	85
5.1	A deeper understanding of assembly bias	85
5.2	The first prediction of the radial acceleration relation for small satellite galaxies	86
5.3	The role of quasars in cosmic reionization	86
	Bibliography	89
	List of Figures	115
	List of Tables	117
	Acknowledgements	119

Introduction

Curiosity has shaped the history of humankind, possibly providing an evolutionary advantage [1]. Among the countless questions that humans, over millenia, have sought answers to, a special place is occupied by our role in the Cosmos. In almost every ancient culture, Earth was placed at the center of the Universe. With the advent of modern science, astronomers and cosmologists started to relegate humankind farther and farther away from this central position. At first, the center of the Universe was moved on the Sun, rendering Earth nothing but one of multiple planets. When telescopes became advanced enough to allow measurements of stellar distances, it rapidly became clear that the position of the Sun was not central, but rather in the outskirts of our galaxy, the Milky Way. Eventually, in the last decades astronomers realized that our Galaxy is not unique at all, but a rather normal celestial body among billions, each one hosting billions of stars and even more planets. This progressive de-centralization of Earth is now embodied in the ‘cosmological principle’ stating that there is no preferential place in the Universe. Such principle is one of the pillars of the current cosmological paradigm, Λ CDM. In this model the Universe has a defined beginning, the Big Bang, where everything comes into being, followed by the inflation, a period of rapid expansion that creates a dense, hot and smooth distribution of matter. From this moment on, the evolution of the Universe is regulated by gravity only, as a consequence of the overall neutral electric charge. Tiny fluctuations in the matter density are amplified into a network of ‘haloes’, i.e. matter clumps, interconnected by filaments running through void regions. Within this cosmic web, galaxies and stars are formed. Following inflation, the Universe keeps expanding at a smaller rate and, consequently, cools down. Roughly 400,000 years after the Big Bang, the temperature is sufficiently low to allow the recombination of protons and electrons. Photons, once trapped by the primordial plasma, are set free, and we now observe them as a Cosmic Microwave Background (CMB) radiation. These photons provide a fossil record of the epoch when they last interacted with matter and carry precious information about the content of the Universe and its evolution. Less than a billion years after the Big Bang, the first stars and galaxies form and start pouring copious amount of radiation in the surrounding gas (called inter-galactic medium, or IGM). These photons are responsible for the last global phase transition in the Universe, i.e. the transformation of the neutral IGM into a highly-ionized plasma. This is the Epoch of cosmic Reionization (EoR). Over the entire cosmic history, the relentless action of gravity keeps driving material toward each other, enhancing the inhomogeneities and building more and more massive haloes.

One of the most important and astonishing findings of the last century is certainly the discovery that ordinary matter is only a very small fraction of the total. The content of the Universe is, in fact, dominated by two unknown components, dubbed ‘dark matter’ (DM) and ‘dark energy’ for lack of better understanding. We discuss them together with the Λ CDM paradigm in Section 1.1, while we present one of the most-discussed alternative cosmological models in Section 1.2. The formation of structures

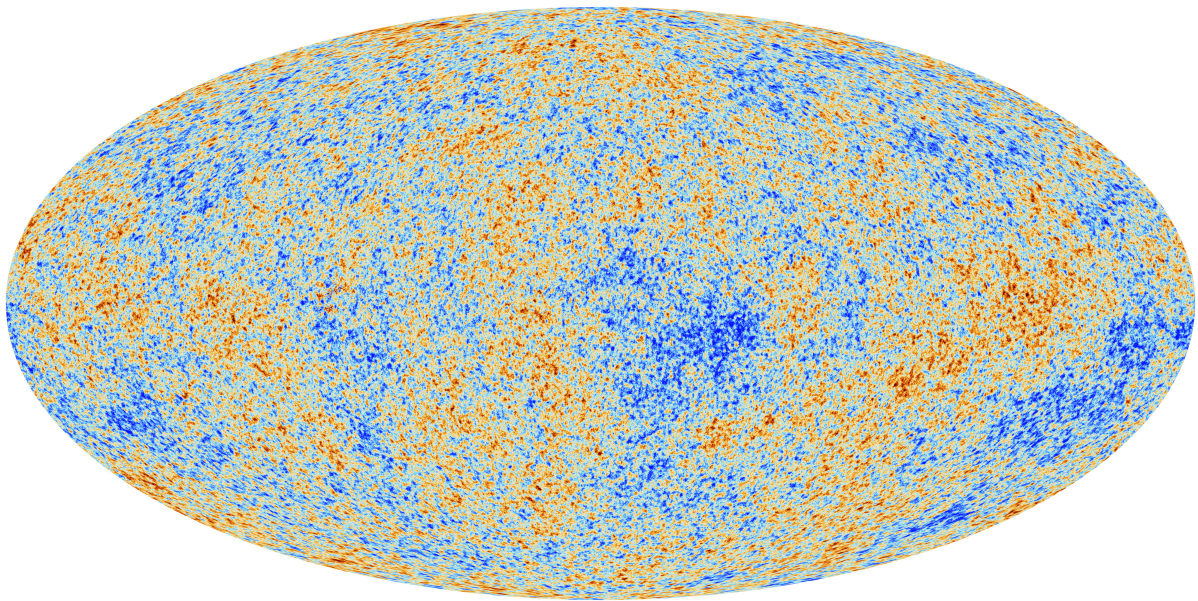


Figure 1.1: Map of the cosmic microwave background as reconstructed by the *Planck* satellite [5].

within the Λ CDM model is addressed in Section 1.3 and the EoR in Section 1.4. Finally we provide a brief overview of numerical simulations, the main tool employed in this Thesis, in Section 1.5.

1.1 The standard cosmological model

During the past century, cosmology has taken a quantum leap and transformed from a philosophical discipline into a modern science. Nevertheless, it remains atypical among natural sciences because of the impossibility to manipulate the experimental setup (i.e. the entire Universe itself). Despite this limitation, in the last decades a concordance model able to explain the majority of available observations has emerged. This is the Λ CDM paradigm and is rooted in the cosmological principle, stating that

The Universe is isotropic and homogeneous on sufficiently-large scales.

At present time, homogeneity and isotropy are found on scales of hundreds of Megaparsecs¹ [e.g. 2–4]. The main evidence in support of the cosmological principle comes from the CMB (Fig. 1.1), which is isotropic and follows an almost-perfect blackbody spectrum with temperature $T_{\text{CMB}} = 2.7$ K. Local deviations from this average spectrum are measured to be of order $\delta T/T \approx 10^{-5}$ [5], providing a measurement of the initial fluctuations in the density field of the Universe and, hence, of the deviation from homogeneity [6].

The CMB constrains the initial state of the Universe but it does not contain information on how the subsequent evolution, which is governed by the theory of General Relativity (GR), developed between 1907 and 1915 by Albert Einstein. This is one of the two pillars in our understanding of fundamental physics, together with the Quantum Field Theory (QFT) describing particles and three of the four fundamental forces, namely the weak, strong and electromagnetic interactions. GR, instead, describes how matter and energy distort space and time (that are not independent entities, but rather the two

¹ The fundamental length unit in cosmology is the parsec (pc), defined as the distance between Earth and a star with annual parallax of one arcsecond, i.e. $1 \text{ pc} \approx 3.1 \times 10^{16} \text{ m}$. $1 \text{ Mpc} = 10^6 \text{ pc}$.

component of the more fundamental spacetime) to produce gravitational interactions and how gravity acts on the matter and energy themselves. The spacetime is described through a metric (i.e. a rank-2 tensor field $g_{\mu\nu}$) that connects infinitesimal variations in the spacetime coordinates to the overall distance ds between the initial and final points

$$ds^2 = g_{\mu\nu} dx^\mu dx^\nu, \quad \mu = \{0, 1, 2, 3\} \quad (1.1)$$

where dx^μ are the components of an infinitesimal four-vector containing both the temporal (index 0) and spatial (indices 1 to 3) coordinates and we employ the Einstein convention for summation, so that repeated indices are summed over. The metric is a function of the spacetime coordinates and is connected with the content of the Universe through Einstein equations [7]

$$R_{\mu\nu} - \frac{1}{2} R g_{\mu\nu} = \frac{8\pi G}{c^4} T_{\mu\nu} \quad (1.2)$$

where the Ricci tensor $R_{\mu\nu}$ and the Ricci scalar $R \equiv R^\mu_\mu$ are functions of the metric $g_{\mu\nu}$ and describe the spacetime geometry, G is the gravitational constant, c the speed of light and $T_{\mu\nu}$ is the energy-momentum tensor describing the matter-energy content of the Universe.

Enforcing the cosmological principle at all scales is sufficient to constrain the metric to a specific form, known as the Friedmann-(Lemaître-)Robertson-Walker (FLRW) metric [8–14]:

$$ds^2 = c^2 dt^2 + a^2(t) \left[dr^2 + f_K^2(r) d\Omega^2 \right] \quad (1.3)$$

where r , Ω and t are the radial, angular and time coordinates, respectively, and $f_K(r)$ is a function of the curvature parameter K (describing the overall geometry of the universe), taking the form (for a simply-connected spacetime)

$$f_K(r) = \begin{cases} \frac{1}{\sqrt{K}} \sin(\sqrt{K}r), & K > 0, \text{ closed universe} \\ r, & K = 0, \text{ flat universe} \\ \frac{1}{\sqrt{|K|}} \sinh(\sqrt{|K|}r), & K < 0, \text{ open universe} \end{cases} \quad (1.4)$$

Finally, the scale factor $a(t)$ describes how the size of the Universe evolves in time and is normalized so that $a(t_0) = 1$ at the current cosmic time t_0 (i.e. today). We can therefore factor out the expansion of the Universe using a and introduce the comoving coordinate \mathbf{x} , related to the physical position \mathbf{r} via

$$\mathbf{r} = a\mathbf{x}.$$

In a similar way, the physical velocity \mathbf{u} is given by

$$\mathbf{u} = \dot{\mathbf{r}} = \dot{a}\mathbf{x} + a\dot{\mathbf{x}} \equiv H\mathbf{r} + \mathbf{v}$$

where a dot denotes a derivative with respect to the cosmic time t and we have defined the peculiar velocity \mathbf{v} , i.e. the velocity after factoring out the Universe expansion. The latter is parametrized by the Hubble parameter $H \equiv \dot{a}/a$.

The geometry of the Universe can be measured using standard rulers (i.e. structures with known length) or standard candles (i.e. phenomena with known luminosity). These two independent methods coherently point to a flat Universe[15–17]. In this special case, $K = 0$ and the FLRW metric reduces to

the Minkowski one [18] at any given fixed cosmic time (i.e. freezing the expansion of the Universe)

$$g_{\mu\nu} = \begin{cases} -c^2, & \mu = \nu = 0 \\ 1, & \mu = \nu = 1, 2, 3 \\ 0, & \text{otherwise} \end{cases} \quad (1.5)$$

that corresponds to the usual (Euclidean) distance *in the spatial dimensions*. The flatness of space constrains the total mass-energy density of the Universe, as we will see in the next Section.

1.1.1 Content of the Universe

The CMB provides us with the ‘initial’ state of the cosmological density field. On the other hand, GR describes its evolution and, crucially, depends on the content of the Universe. Assuming the latter can be described as a perfect fluid, i.e. a fluid fully characterized by its energy density ρ and isotropic pressure p , only two of the Einstein equations 1.2 are non-trivial, namely

$$\ddot{a} + \frac{4\pi}{3}G\left(\rho + 3\frac{p}{c^2}\right)a = 0, \quad (1.6)$$

$$\dot{a}^2 + Kc^2 = \frac{8\pi}{3}G\rho a^2. \quad (1.7)$$

These are known as Friedmann’s equations [8, 9]. The second one can be solved for the curvature parameter K , yielding:

$$K\frac{c^2}{a^2} = H^2\left[\frac{8\pi G\rho}{3H^2} - 1\right] \equiv H^2\left[\frac{\rho}{\rho_{\text{crit}}} - 1\right]$$

where we have defined the critical density $\rho_{\text{crit}} \equiv 8\pi G/3H^2$, that owes its name to the fact that it is the only value of density corresponding to a flat Universe (i.e. $K = 0$). Note that H and ρ_{crit} change with time. In the following, we will use the density parameter $\Omega_x \equiv \rho_x/\rho_{\text{crit}}$ to indicate the density of a generic component x scaled by the critical density of the Universe. The flat geometry of spacetime indicates that the total density is exactly (within the error on the curvature measurements) the critical one, i.e. $\Omega_{\text{tot}} = 1$.

In order to determine the density evolution of the different components in the Universe, we can employ the adiabaticity condition $dU = -p dV$, with U being the internal energy of a closed system and V its (physical) volume. This holds true in a cosmological context because, as a consequence of the cosmological principle, there is no heat, work or mass transfer between different regions of the Universe, that therefore act as closed systems. The value of U is given by the rest mass energy $U = (\rho V)c^2$ (where, again, we are assuming the content of the Universe can be described as a perfect fluid), while the volume can be estimated as $V \approx a^3$ and thus

$$d(\rho a^3 c^2) = -p d(a^3). \quad (1.8)$$

In order to solve for $\rho(a)$, we need to specify the equation of state $p(\rho)$ characterizing the matter-energy component.

Radiation

Radiation is the dominant component in the first few thousands years after the Big Bang. Its energy-density evolution follows from equation 1.8 and its equation of state $p = \rho c^2/3$ [e.g. 19], namely

$\rho_\gamma(a) = \rho_{\gamma,0}a^{-4}$, where we have denoted with $\rho_{\gamma,0} \approx 10^{-5}\rho_{\text{crit}}$ its value today [20]. The evolution is more rapid than the pure dilution $\rho \propto a^{-3}$ because, in addition to it, the energy content of each photon is reduced by the expansion of the Universe. This cosmological redshift z is given by

$$z = \frac{\Delta\lambda}{\lambda_e} = \frac{1}{a_e} - 1 \quad (1.9)$$

where $\Delta\lambda$ is the observed wavelength shift with respect to the emitted photon wavelength λ_e and a_e is the Universe scale factor at the time of emission. The fact that photons travel with constant speed² establishes a univocal relation between the cosmological redshift and the distance of the source. However, inferring z is not trivial. For instance, determining $\Delta\lambda$ requires the knowledge of the emitted wavelength and, additionally, the peculiar velocity of the source produces an additional shift in the observed wavelength (Doppler shift). Moreover, before the CMB epoch (t_{CMB} , i.e. the time when CMB photons interacted for the last time with matter), baryons in the Universe are kept ionized by a swarm of high-energy photons and these, in turn, are trapped by Thomson scattering with the free charges. This scattering erases the information photons were carrying, producing a physical barrier that prevents us from observing radiation from earlier epochs.

Baryonic and dark matter

Baryonic³ matter is produced approximately 3 minutes after the Big Bang, in the form of a hot and highly-ionized plasma. Initially, only photons, electrons and protons are produced. All other elements come from nuclear reactions that occur at later time. During the so-called primordial nucleosynthesis, taking place between ≈ 10 seconds and ≈ 20 minutes after the Big Bang⁴, the majority of helium was produced, together with traces of lithium. After this initial offspring, the primordial gas is composed by an hydrogen and helium mass fractions of $X \approx 75\%$ and $Y \approx 25\%$, respectively, while heavier elements are negligible ($Z \approx 0.01\%$). The relative abundances of these atomic species solely depend on the baryons-to-photons ratio $\eta_{\text{b-p}} \sim 10^{-10}$. However, the precise value of $\eta_{\text{b-p}}$ has little impact on the forecasted abundances, making the predictions from this theory very strong (and, hence, their observational confirmation a powerful evidence in favor of the theory itself). The remaining elements have been produced much later during the life cycle of stars (for light elements) or during binary neutron stars mergers (for heavy elements).

During the second half of the 20th century, however, the existence of invisible mass in the Universe became progressively more clear. Among the first evidence in this direction, the Swiss astronomer Fritz Zwicky observed that the velocity of galaxies in the outskirts of the Coma cluster can only be explained assuming that a large fraction of the total mass is hidden [21]. It soon became clear that this hidden mass, called ‘dark’ since it appears not to interact with electromagnetic radiation, can not be explained by baryons. Further studies of rotation curves in galaxies and galaxy clusters strengthened the early findings of Zwicky. In particular, the circular velocity of stars in galaxies does not decrease with increasing distance from the center, as expected from the distribution of baryonic matter, but remains approximately constant. This has been explained by the presence of a DM halo on scales much larger than the galaxy

² The photon speed across the Universe is not exactly constant since their velocity depends on the traversed matter, but the low density of baryons in the Universe renders the light speed effectively constant.

³ In a cosmological and astrophysical context, this term refers to the entirety of ordinary (i.e. predicted by the standard model of particle physics) massive particles with the exception of neutrinos.

⁴ The onset of primordial nucleosynthesis correspond to the temperature becoming sufficiently low to allow deuterium, necessary for the production of all elements heavier than hydrogen, to survive. The end of it, instead, corresponds to atomic kinetic energies becoming too small to trigger nuclear reactions.

itself [22]. Furthermore, galaxy clusters contain a large amount of hot gas that can be detected using its X-ray bremsstrahlung radiation. The internal energy of such gas (estimated from its temperature) is much larger than the gravitational binding energy provided by the baryonic matter only. Therefore, in order to keep the intra-cluster gas bound, a large amount of DM must be present [23, 24]. In addition to dynamical probes, the CMB radiation as well as gravitational lensing (i.e. the distortions of the photon path as a consequence of gravitational interactions with matter) provide abundant evidence for the existence of DM. The former exhibits features (called Baryonic Acoustic Oscillations, or BAO) that depend on the relative importance of matter that does not interact electromagnetically with respect to the one that does. The BAO not only provide evidence for the existence of DM [17, 20], but also provide a standard ruler (i.e. a absolute scale that can be determined *a priori*) useful in order to constrain the geometry of the Universe. In gravitational lensing, the bending of light from a cosmic structure is sensitive to its total matter content. Combining this mass estimation with the one obtained through electromagnetic probes, it appears clear that visible matter is only a small fraction of the total [25–28]. In the Λ CDM model, DM is assumed to be ‘cold’, i.e. non-relativistic. This is necessary to allow DM to cluster in haloes and host galaxies at their center (see Section 1.3) [29]. Stringent constraints on the non-relativistic nature of DM come from numerical simulation (see Section 1.5) and studies of the Lyman- α forest (see Section 1.4.1). Additionally, the fact that it does not interact through electro-magnetic forces renders it dissipationless (i.e. unable to emit photons to cool down) and collisionless (unless new, unknown, fundamental interactions exists within DM particles). On cosmological scales, matter has typical velocities much smaller than the speed of light, making its pressure negligible compared to its internal energy ρc^2 . Hence, it can be approximated by a pressureless fluid and, from equation 1.8, follows $\rho_m(a) = \rho_{m,0} a^{-3}$. Here we have again denoted with $\rho_{m,0}$ the value of the matter density today. Recent measurements from the ESA satellite *Planck* yield a total matter density of $\Omega_m = 0.308 \pm 0.012$ and a baryonic density $\Omega_b = 0.0493 \pm 0.0005$ [20].

Dark energy

In the late 1990s, two groups independently discovered that the expansion of the Universe is currently accelerating [30, 31]. Baryonic and dark matter alone are unable to explain this behaviour, since gravity is always attractive and, therefore, slows down the expansion of the Universe. The most natural solution to such puzzle is a non-vanishing cosmological constant Λ , i.e. a form of energy with constant density. Equation 1.8 yields in this case a negative pressure $p_\Lambda = -c^2 \rho_\Lambda$ and therefore a repulsive force that, at late times ($z \lesssim 1$), overcomes the gravitational pull and accelerates the expansion of the Universe.

In the left panel of Fig. 1.2 the relative importance of matter, radiation and dark energy as a function of cosmic time is shown. The vacuum energy predicted by quantum field theory has the required properties, but exceeds the observed value $\Omega_\Lambda = 0.692 \pm 0.010$ by ~ 120 order of magnitudes [32] (or ‘just’ ~ 56 if the Higgs rest-mass energy is used as the maximum energy scale where the current QFT is reliable [33]).

1.1.2 Problems of the Λ CDM model

The Λ CDM model is very successful in explaining the properties of the CMB, the measured gravitational lensing, the formation and statistical properties of large-scale structures, and the dynamics of galaxies (see [35] for a review). Nevertheless, there are some problems afflicting the concordance cosmological model, especially at small scales. A first issue emerge when the DM density profiles of simulated haloes are compared to the ones inferred from observations; while the former are typically cuspy (i.e. the density always increases towards the center), observation of small objects suggest that they may have profile that flattens at the center (cored profile) [36–41]. This issue may be solved assuming strong and impulsive ejections of material (e.g. driven by star formation, supernova explosions or AGN feedback, see

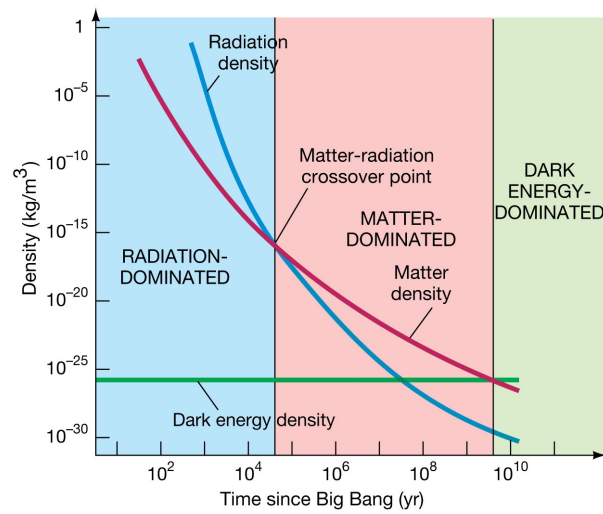


Figure 1.2: Evolution of matter, radiation and dark energy density across cosmic time [34].

Section 1.3), that can flatten the original cuspy profile [e.g. 42], but may also be indicative of a different cosmological model [43]. Another problem, dubbed ‘too big to fail’, is the fact that the number of observed satellite galaxies hosting significant amounts of stars is much smaller than predicted by inferring the stellar mass associated to a DM subhalo via abundance matching [44]. However, including baryons in the simulations shows that, depending on the details of the feedback scheme implemented (see Section 1.5.4), this issue can be solved thanks to quenching mechanisms preventing star-formation [45–48]. In recent years, measurements of the Hubble parameter at different epochs show discrepant results. In particular, the value inferred from the CMB is in tension with the one obtained from some gravitational lensing studies and local probes like supernovae [17, 49–51]. Moreover, the amount of DM inferred to reside in galaxies shows a correlation with the baryonic component [52]. The latest incarnation of this connection is the radial acceleration relation (RAR), that tightly links the observed radial acceleration to the one inferred by solving the Poisson equation for the baryons only [53]. Simulations of Λ CDM can reproduce the observed mean trend RAR but over-predict the scatter [54–60], which is consistent with zero in observations. We will discuss further this issue in Chapter 3. Finally, the nature of dark energy and dark matter (together making up more than 94% of the mass-energy content of the Universe) are still unknown. In particular, DM has so far eluded detection from laboratory experiments across the Globe.

1.2 Modified Newtonian Dynamics

The problems that the Λ CDM model faces at small scales powered the theoretical exploration of alternative cosmological models. A prolific research path has been relaxing some of the assumptions about DM made in the Λ CDM model. For instance, allowing DM particles to interact with each other (Interacting Dark Matter), replacing dark energy with a light scalar field (Quintessence models), assuming multiple species of DM particles (Multiple Dark Matter), introducing a new interaction between DM and dark energy (Interacting Dark Sector), and many more [see 61, 62, for reviews]). A particular model that has gained a fair amount of popularity is the MODified Newtonian Dynamics (MOND). This paradigm assumes that the acceleration of an object is non-linearly related to the force acting on it. In particular,

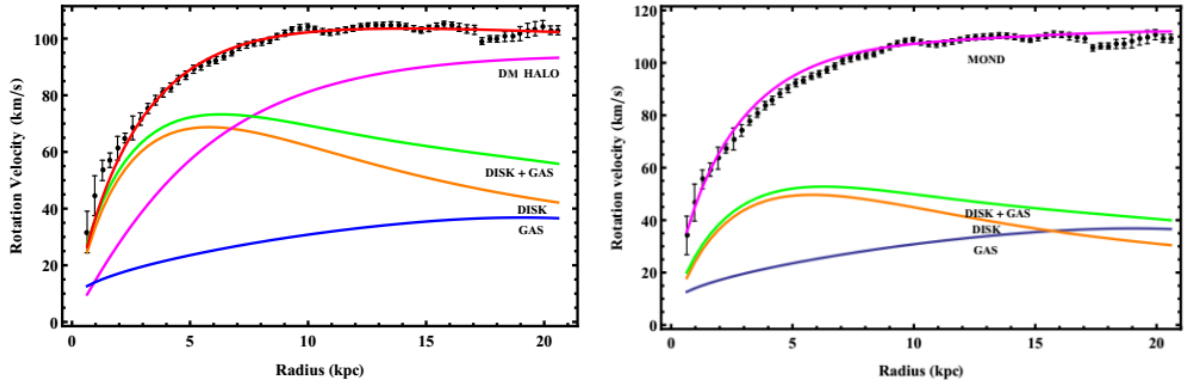


Figure 1.3: Observed rotation curve (points with errorbars) of the galaxy ESO138-G014 and predictions from the Λ CDM (left panel) and MOND (right panel) cosmological models for the gas, stars, DM and total radial profiles. Adapted from [71].

the fundamental relation in MOND is [63]

$$a_{\text{MOND}} \mu(a_{\text{MOND}}/a_0) = a_{\text{N}} \quad (1.10)$$

where a_{MOND} and a_{N} are the predicted accelerations in the MOND and Newtonian theories, and $\mu(x)$ is an interpolation function with the following properties: $\mu(x) \rightarrow 1$ for $x \gg 1$ and $\mu(x) \rightarrow x$ for $x \ll 1$. The MOND relation can be achieved by assuming either a modified gravitational interaction (in the form of a modified Poisson's equation [64]) or a modified inertia of bodies (in the form of a corrected Newton's second law [65]). The value of the new fundamental constant of Nature $a_0 \approx 10^{-10} \text{ m s}^{-2}$ was set so that the MOND theory can reproduce the observed rotation curves of galaxies without the need to invoke the existence of DM [66]. Using the MOND formula for particle accelerations, the circular velocity of a galaxy becomes independent of the radial distance outside of the (baryonic) matter distribution. In Fig. 1.3 the measured rotation curve (points with errorbars) of the galaxy ESO138-G014 is shown together with the Λ CDM (right panel) and MOND (left panel) prediction for the gas, stars, DM and total radial profiles. The asymptotic value of the circular velocity V_{asy} is related to the (baryonic) mass within the galaxy M_{g} by

$$M_{\text{g}} = (G a_0)^{-1} V_{\text{asy}}^4. \quad (1.11)$$

This is known as the baryonic Tully-Fisher relation [67–69] and has been observed over more than four orders of magnitude in mass. The value of a_0 inferred fitting observations to equation 1.11 is consistent with the one needed to reproduce galactic rotation curves [70].

The existence of a universal acceleration scale a_0 implies that the internal acceleration of a composite object (e.g. a galaxy) can not be decoupled from an external constant acceleration field g_e acting on the entire system (as done in Newtonian dynamics by referencing to its center of mass). In this External Field Effect (EFE), if $g_e > a_0$ the system will exhibit a quasi-Newtonian behaviour even when the internal acceleration g_i is below a_0 . Interestingly, if $g_i < g_e < a_0$, the system will again behave in a quasi-Newtonian fashion but with an effective gravitational constant $G_{\text{eff}} = G/\mu(g_e/a_0)$ [70].

Despite the ability to reproduce the galactic circular velocity without DM, the MOND theory is still unsatisfying from many points of view. When applied to clusters of galaxies, it is unable to fully solve the mass discrepancy (i.e. even MOND requires some form of hidden mass [72, 73]). Another issue is related to interacting structures, most notably the Bullet cluster, where a segregation between the baryonic material (observed through X-ray emission of the gas) and the mass distribution (measured

through gravitational lensing) is observed [74–76]. In the Λ CDM theory, this is a natural consequence of the collisionless nature of DM, while no such separation is expected in MOND. In addition, if equation 1.10 is conceived as a modified inertia, it entails that energy, as well as linear and angular momentum are not conserved. On the other hand, if an unconventional gravitational interaction is assumed to be the source of equation 1.10, then conservation laws can be recovered including a_0 in the Lagrangian of Newtonian gravity, in what is known as AQUAL theory [64]. Finally, the major problem of MOND lies in the fact that it is a non-relativistic theory. While this is acceptable in the regime of galaxies, cosmological predictions are inherently relativistic. In order to amend this, many extensions have been proposed. For instance, in the Tensor-Vector-Scalar (TeVeS) theory [77, 78] matter geodesics are sourced by a modified metric (with respect to GR) that includes the contribution from a new scalar and a new vector fields. Theoretical arguments suggest that this theory should mimic the cosmology and gravitational lensing features of Λ CDM, but detailed comparison have yet to be carried out. Remarkably, the recent determination of the gravitational wave speed [79, 80] (which coincides with the speed of light) poses a severe challenge to the TeVeS theory [81, 82].

1.3 Structure formation in Λ CDM

The Universe is characterized by a network of structures ranging from the largest scales to the tiniest ones. Key to understand their formation are the initial conditions from which the network evolved. These are encoded in the temperature fluctuations of the CMB, that carry informations about the density field at the time $t_{\text{CMB}} \approx 3 \times 10^5 t_{\text{H}}$, where $t_{\text{Universe}} = 13.4 \times 10^9 \text{ yr}$ is the age of the Universe today. Since t_{CMB} is such a small fraction of t_{H} , we can effectively assume the density fluctuations reconstructed from the CMB as the initial state for the evolution of structures in the Universe. Remarkably, these fluctuations are coherent over scales that are not in causal contact. Their production mechanism remains unclear, but a widely-accepted possibility is that inflation, a period of exponential expansion following the Big Bang, enhanced primordial quantum fluctuations and stretched them on scales that could not be in causal contact otherwise [19].

From these minuscule fluctuations in the very early Universe, a zoo of objects developed. Slightly overdense region exert a stronger-than-average gravitational pull and therefore attract material from surrounding regions, growing denser in a positive feedback loop. In an idealized situation, an ellipsoidal overdense patch embedded in a uniform background initially collapses along the shortest axes, where gravitational pull is the strongest, forming a so-called sheet. It then collapses along the intermediate axes into a filament and finally along the longest axes into a roundish object usually known as halo [83]. The speed at which this process takes place, and hence the stage reached at the current cosmic time, is set by the density contrast of the collapsing patch with respect to the background, and by its ellipticity. In a realistic universe, the collapse is complicated by the interaction with neighbouring objects, exerting their gravitational pull in the form of tidal forces. Nevertheless, the resulting structures can be fairly well categorized into the classes described above. In this Section, we will revise the theory of gravitational collapse for dark matter and baryons, and outline the statistical properties of the final density field.

Density fluctuations are conveniently described using the overdensity

$$\delta(\mathbf{x}, t) \equiv \frac{\rho(\mathbf{x}, t) - \bar{\rho}(t)}{\bar{\rho}(t)} \quad (1.12)$$

where $\bar{\rho}(t)$ denotes a spatial average over the density ρ and the positivity of mass-energy imposes $\delta > -1$. In order to analytically describe structure formation within the Λ CDM framework some approximations are required. As a first step, we can coarsely divide the forces acting on matter in the Universe in

two categories, namely the gravitational interaction, that is always attractive and therefore enhances primordial fluctuations, and ‘micro-physics’, i.e. all non-gravitational interactions, that affect only baryons and provide a pressure support. This provides us a first approximate way to estimate the collapse, namely comparing gravitational and non-gravitational interactions and defining the Jeans scale [84] where the two are equal. To first approximation, only overdensities larger than the Jeans scale collapse into a structure. To go beyond this coarse estimate, we need a theory describing the evolution of density fluctuations, that we will now briefly describe.

1.3.1 Dark matter collapse

The dominant clustering component of the Universe is dark matter and, therefore, we start by describing the formation of structure in a DM-only universe. Despite the Universe being an inherently relativistic system, for small overdensities (i.e. weak gravitational fields) the GR equations reduce to the Newtonian gravity whenever the overdensity scale is much smaller than the Hubble radius

$$d_H = \frac{c}{H} \quad (1.13)$$

that describes the portion of the Universe in causal contact. Additionally, dark matter can be treated as a fluid as long as its velocity field is uniquely defined in every point. This approximation holds until the late stage of structure collapse, when multiple flows can coexist at locations where, thanks to the collisionless nature of DM, material coming from different directions intersect. Therefore, the fluid approximation is exact only for un-collapsed regions (i.e. at early time and/or large scales). Under this approximation, the dark matter can be described using the (comoving) continuity, Euler and Poisson equations:

$$\frac{\partial \delta}{\partial t} + \frac{1}{a} \nabla_{\mathbf{x}} \cdot [(1 + \delta)\mathbf{v}] = 0 \quad (1.14)$$

$$\frac{\partial \mathbf{v}}{\partial t} + H\mathbf{v} + \frac{1}{a}(\mathbf{v} \cdot \nabla_{\mathbf{x}})\mathbf{v} = -\frac{1}{a}\nabla_{\mathbf{x}}\phi \quad (1.15)$$

$$\nabla_{\mathbf{x}}^2 \phi = \frac{3H_0^2 \Omega_m}{2a} \delta \quad (1.16)$$

where we have dropped the pressure term in the Euler equation since DM is assumed to be collisionless and, hence, pressureless. Here $H_0 = H(t_0)$, $\phi(\mathbf{x}, t)$ is the (comoving) gravitational potential, related to the one in physical coordinates $\phi_{\text{phys}}(\mathbf{x}, t)$ by

$$\phi(\mathbf{x}, t) = \phi_{\text{phys}}(\mathbf{x}, t) + \frac{\ddot{a}a}{2} |\mathbf{x}|^2. \quad (1.17)$$

The system of equations 1.14 – 1.16 has no analytical solution and, therefore, we need to rely on approximated techniques. One of the most successful so far has been the perturbative approach, that is valid whenever the perturbations are small ($|\delta| \ll 1$). Under this condition, any (positive) power of the perturbation is much smaller than the perturbation itself, allowing us to discard high-order terms and simplify the equations. When only the first-order terms are present (a case known as linear theory), the system of equations 1.14 – 1.16 can be combined into a single equation containing no spatial derivatives. Therefore, the solution can be written as a combination of spatial and temporal components:

$$\delta(\mathbf{x}, t) = D_+(t)\Delta_+(\mathbf{x}) + D_-(t)\Delta_-(\mathbf{x}), \quad (1.18)$$

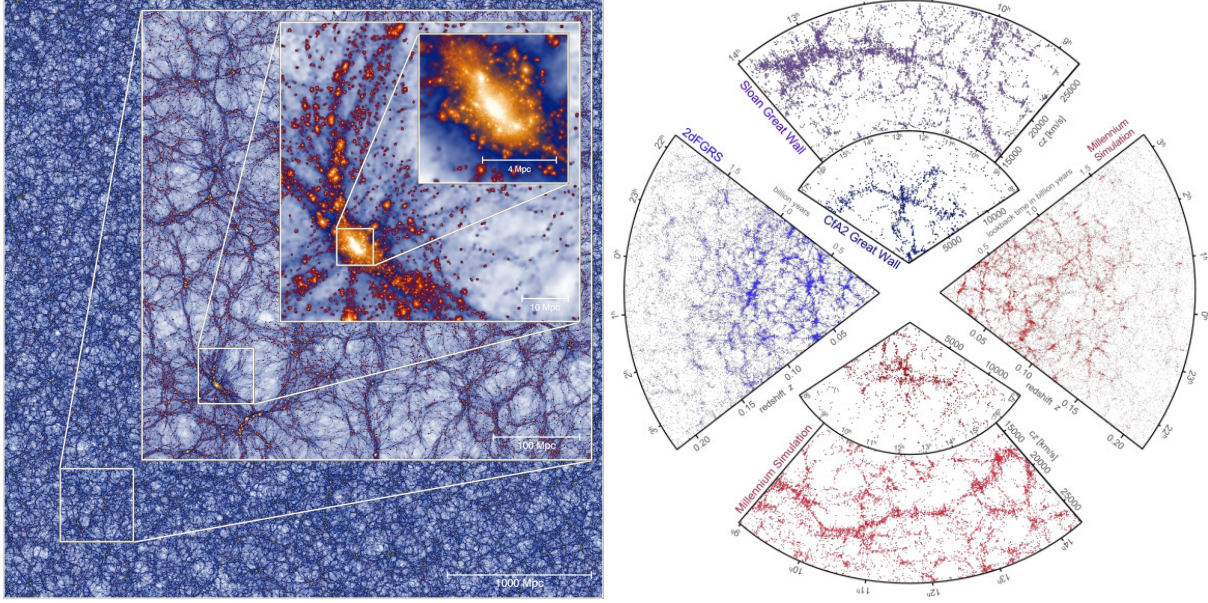


Figure 1.4: Left: Dark matter density in a cosmological simulation [85]. The insets show a series of zoom-ins on a massive DM halo in the simulation. Right: Comparison between simulated (right and bottom slices) and observed (left and top) galaxy distributions [86].

where the spatial parts Δ_{\pm} are unconstrained by the (first-order) perturbative equations. The terms D_{+} and D_{-} represent growing and decaying perturbations, respectively, and depend on Ω_m and $H(z)$. Since we are interested in structure *formation*, only the former is relevant.

As mentioned, the perturbative approach is valid only as long as perturbations are small. In order to extend its validity to larger overdensities, it is possible to include some of the higher-order terms. However, this proved to be difficult and does not remove the underlying assumption of smallness of the perturbations. In fact, whenever a density perturbation is comparable to the background density, it decouples from the Universe expansion and start collapsing only as a consequence of its own gravity, entering in a strongly non-linear regime. Therefore, conceptually different approaches are needed to study the non-linear evolution of original perturbations, that characterize the last stages of structure formation. The most-used tool to tackle this issue are numerical simulations, that will be described in Section 1.5 and will be used throughout this Thesis.

One of the most remarkable features of cosmological structure formation is that the process of structure formation is hierarchical, with small structures forming first and then progressively merging into larger objects during the evolution of the Universe [87]. A complete blending, however, requires a very long time and, hence, small-scale structures remain embedded in larger objects for long. These are typically called dark-matter subhaloes while their baryonic content forms the so-called satellite galaxies. The network of large-scale structures unveiled by numerical simulations is shown in Fig. 1.4.

The statistical properties of the structures in the Universe are often described using the two-point correlation function (2PCF) $\xi(q)$, that describes the excess probability dP of finding pairs of structures at a given separation q with respect to a random Poisson distribution, i.e.

$$dP = (1 + \xi(q)) n dV \quad (1.19)$$

where n is the mean number density of structures and dV is an infinitesimal volume element. Its Fourier

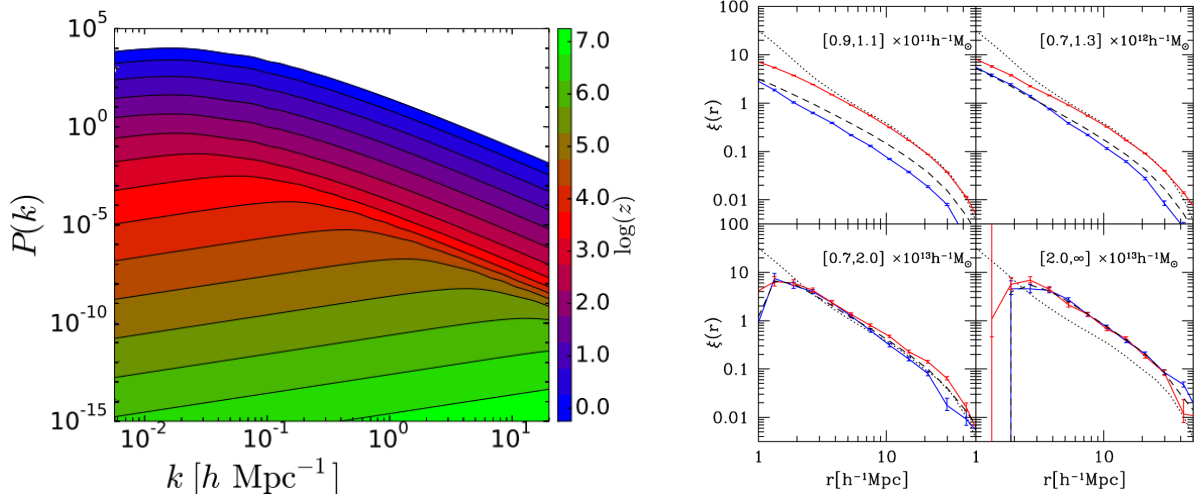


Figure 1.5: Left: Linear power spectrum $P_{\text{linear}}(k)$ of density perturbations as a function of redshift [89]. Right: Two-point correlation function for young (blue lines) and old (red lines) DM haloes in different mass bins (reported in the top right of each panel) [90].

transform is called power spectrum $P(k)$ and describes the relative amplitude of fluctuations as a function of their scale $2\pi k^{-1}$. The isotropy of $\xi(q)$ and $P(k)$ follows from the cosmological principle. In the case of a Gaussian random field (i.e. when the probability distribution of its values is Gaussian and each Fourier mode is statistically independent), $P(k)$ provides a complete description of it together with the mean value of the field. Observationally, the CMB fluctuations are fully consistent with a Gaussian random field [88] and the primordial power spectrum is measured to follow a power-law $P \propto k^n$ with slope $n = 0.961 \pm 0.005$ [20] (consistent with prediction from inflation). Note, however, that the different growth rates of perturbations during the radiation-dominated epoch modifies this shape introducing a broad peak centered at $k \approx 10^{-2}$ Mpc (left panel of Fig. 1.5). Additionally, the (non-linear) process of structure formation produces a highly non-Gaussian (evolved) density field.

Assembly bias

Numerical simulations (see Section 1.5) unveiled that the clustering properties of DM haloes depend on their age, i.e. the time of their collapse [90, 91]. This effect, dubbed ‘assembly bias’, is exemplified in the right panel of Fig. 1.5 through the 2PCF of young (i.e. late-forming, blue lines) and old (i.e. early-forming, red lines) haloes in four different mass bins. While the shape of the 2PCF for these two halo populations is similar, there is a prominent difference in the amplitude at low masses, that progressively disappears for larger objects. This offset reflects the fact that old haloes have a larger clustering, i.e. typically live in denser environments than young ones. Numerical studies demonstrate that a number of halo properties (e.g. concentration, internal velocity dispersion) are correlated with its age [92–97]. The physical mechanism triggering such a difference has been recently investigated in [98], showing that the halo environment modulates the accretion of new material through tidal forces, eventually starving objects. Denser environments are more efficient in this, and hence preferentially host old haloes.

1.3.2 Baryonic collapse

The collapse of dark matter and the consequent formation of proto-haloes provide potential wells that enhance the condensation of the baryonic material. Differently from dark matter, baryons are collisional and therefore, during collapse, undergo strong shocks that increase their temperature and provide pressure support against further collapse. Once the pressure gradient is sufficiently large, it balances the gravitational attraction and the system settles in a hydrostatic equilibrium. However, since gas cooling typically involves two (baryonic) particles, denser regions in the halo cool down more efficiently, losing pressure support and collapsing further into the potential well of the dark-matter halo. This process eventually produces a segregation of the baryonic content, concentrated at the center of the halo, from the dark matter, that remains more diffuse as a consequence of the impossibility to dissipate its energy. Therefore, galaxies are expected to live at the centre of a much-larger dark-matter haloes. Eventually, the gas can reach a density sufficiently large to fragment under its self-gravity and form high-density cores where the gravitational heating from the collapse ignites nuclear hydrogen fusion, forming stars. During their life cycle, different nuclear reactions take place in stars, producing a variety of light elements. Some of them are also produced in supernovae, i.e. the explosion of stars at least 8 times more massive than our Sun, while heavy nuclei are produced when two neutron stars (i.e. one of the possible remnants of supernova explosion) merge. All elements heavier than Helium are collectively called ‘metals’ and their abundance is called ‘metallicity’ (Z). Additionally, stars (especially in their early life and asymptotic giant branch phase) produce outflows, called ‘winds’, that injects material, energy and momentum in the surrounding medium. In a similar fashion, supernovae provide comparable ‘feedback’ that control and quench the formation of new stars by heating up the gas and preventing its collapse. Very massive stars are thought to end their life as black holes, i.e. massive compact objects distorting the surrounding spacetime so strongly that nothing can escape their event horizon. It is now believed that all massive galaxies host a supermassive black hole at their center. The extreme accelerations of material inflowing into the supermassive black hole produce strong friction and heats up the gas to billions of Kelvins, producing copious amount of radiation. This radiative feedback is an additional source of energy and heat for the material in the galaxy [99]. When these black holes are actively accreting, they are called Active Galactic Nuclei (AGN) and, if particularly bright, quasars (QSO, standing for Quasi Stellar Objects).

1.4 The epoch of cosmic reionization

The production of the CMB marks the beginning of the cosmic ‘dark ages’, a period of time characterized by no sources of radiation in the Universe, that ends only much later with the formation of the first stars, galaxies and black holes. These first luminous objects slowly ionize bubbles of gas around them, marking the beginning of the Epoch of Reionization (EoR), but the photoionization is hindered by recombinations taking place within the gas. The flux of ionizing photons decays with increasing distance from the source (more rapidly than the inverse square law because of absorption by intervening neutral gas), preventing the growth of these bubbles. However, the process of gravitational collapse continuously produces new stars, galaxies and black holes, while the gas recombination rate depends on the gas density, that decreases with time as a consequence of the expansion of the Universe. Hence, when the former effect takes over the latter, the number of ionizing photons available becomes sufficient to ionize and keep ionized the gas in the IGM. In denser regions, like protogalaxies, the large gas density is sufficient to maintain recombinations dominant over photoionization, therefore keeping the gas neutral and self-shielded from the radiation field.

In the current leading model of cosmic reionization, the dominant sources of ionizing photons right after the dark ages are small star-forming galaxies. These primeval objects are predicted by simulations of

structure formation, and have now been observed⁵ up to $z \sim 11$ [100]. However, the physical properties of these primeval galaxies are largely uncertain. Of primary importance for the reionization process is the escape fraction f_{esc} , i.e. the fraction of ionizing photons produced by a source that reach the IGM, that is however very challenging to measure even at low redshift. Measurements in the local Universe mostly find percent-level escape fractions, while models of the EoR require $f_{\text{esc}} \gtrsim 10\%$ at high redshift [101, 102, and discussions therein]. Another possible source of ionizing photons are AGNs, that have now been observed up to $z \approx 7.5$ [103] and are expected to be in place as early as $z \approx 12$ [104]. Despite their large luminosity, the AGN number density at $z \gtrsim 4$ is too low to produce a significant contribution to the EoR. This conclusion has been recently challenged by new observations of a large population of candidate faint quasars at $z \sim 6$ and its implications for cosmic reionization are the main topic of Chapter 4.

Primeval galaxies are thought to have also singly ionized the intergalactic helium, together with hydrogen. However, they don't produce enough photons with energy above the (second) ionization threshold of helium, that therefore remains singly-ionized in the IGM. The double reionization of helium (usually called simply helium reionization) occurs approximately at redshift $2.7 \lesssim z \lesssim 4$ [105–107] thanks to the energetic photons produced by AGNs, that increase in density until $z \approx 2$.

The transition from a neutral to an ionized medium is not instantaneous. As mentioned above, current models predict that the first regions to be ionized are the overdensities, where baryons collapse and form stars and galaxies. The detailed topology of reionization mainly depends on the clustering properties of the ionizing sources and therefore provides precious informations on this epoch. However, only in very recent times quantitative studies of the EoR morphology have been enabled by new observations [108, 109].

1.4.1 Observational probes

In studying the cosmic reionization, we have to face many challenges. From a theoretical point of view, detailed modeling of this period is computationally demanding (as described at length in Section 1.5.3) and analytical models are typically too simplistic to properly capture the complex transition between a fully neutral to a fully ionized medium. Observationally, the large distance and the opacity of the high- z IGM to radiation bluer than the Ly α frequency limit the constraining power of current observations. Nevertheless, a number of observational probes, combined with advanced modeling, allow us to set constraints on the EoR properties. We will review the most prominent of them in the following.

Lyman- α absorption

The Lyman- α (Ly α) transition of neutral hydrogen is very sensitive to even small number densities of neutral gas. While this hinders observations deep into the reionization epoch, it provides a powerful probe of its tail-end. The photon-absorption cross section for an electronic quantum transition is sharply peaked at the frequency corresponding to the difference between the initial and final energy levels $E_2 > E_1$, i.e. $\nu_{12} = (E_2 - E_1)/h_p$, where h_p is the Planck constant. As a consequence, each patch of (mildly) neutral hydrogen will produce a sharp absorption feature in the spectrum of a background source at frequency ν_{12} in the patch rest-frame. Since radiation is redshifted during its journey to the observer, the position in the spectrum of the absorption feature is set by the location of the patch along the line of sight. The optical depth (measuring the suppression of incoming radiation, see Section 1.5.3 for a rigorous definition) to

⁵ The galaxies observable with current telescopes at such distance are only the brightest (and typically biggest) ones, not the small objects thought to power the EoR. Nevertheless, the hierarchical model of structure formation (see Section 1.3) predicts the existence of many small objects for each massive one.

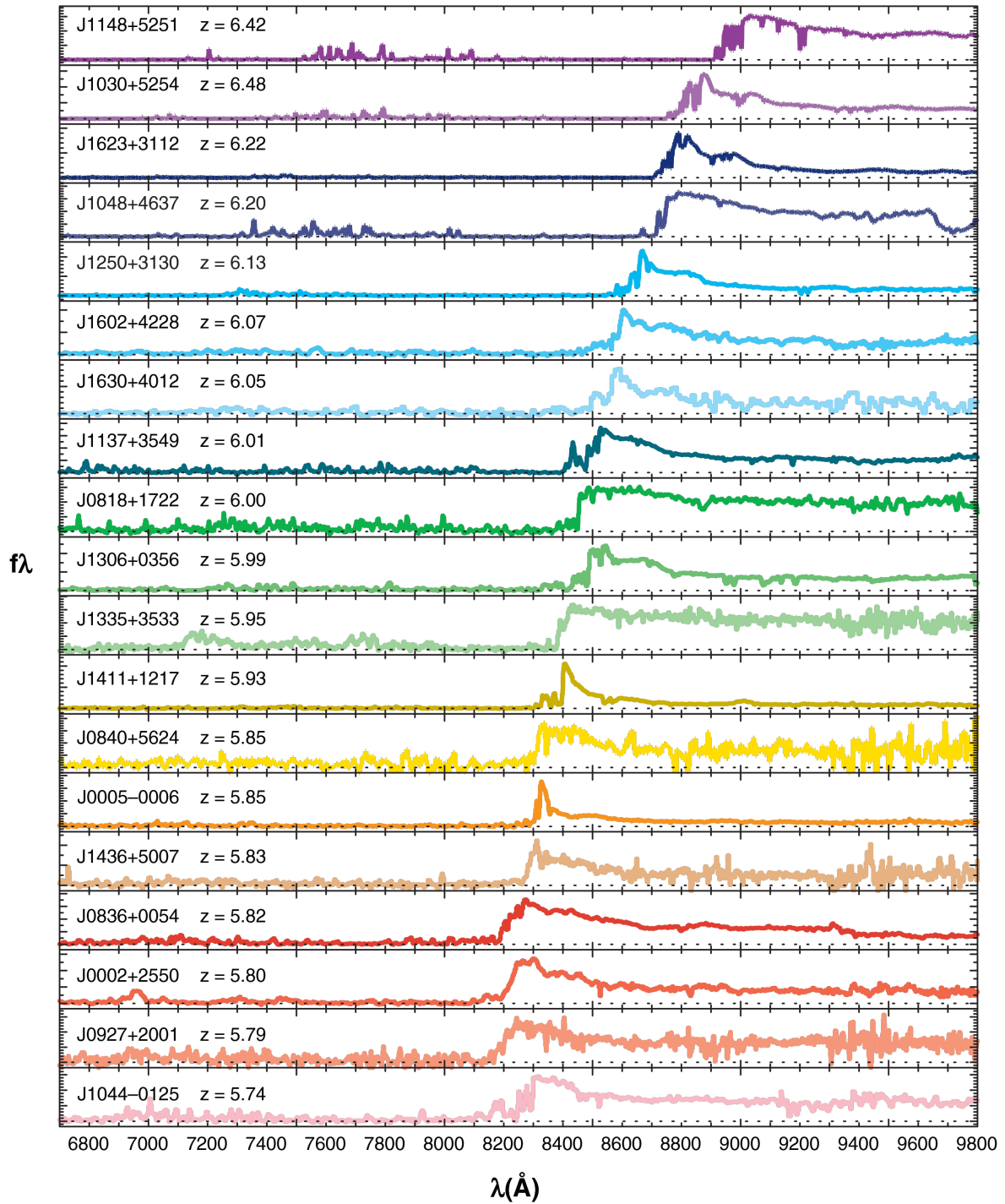


Figure 1.6: Spectra of nineteen SDSS quasars at $5.74 < z < 6.42$ shown in the observer rest-frame and ordered by their redshift (reported in each panel) [110].

Ly α photons is given by [111]

$$\tau_{\text{GP}} = \frac{\pi e^2}{m_e c} f_\alpha \lambda_\alpha \frac{n_{\text{HI}}}{H(z)} \quad (1.20)$$

where e and m_e are the electric charge and mass of the electron, respectively, f_α is the Ly α oscillator strength, $\lambda_\alpha = 1216\text{\AA}$ is its associated wavelength and n_{HI} is the comoving number density of neutral hydrogen. Folding in the cosmological evolution, τ_{GP} for a uniform IGM is given by [110]

$$\tau_{\text{GP}}(z) = 4.9 \times 10^5 \left(\frac{\Omega_m h^2}{0.13} \right)^{-\frac{1}{2}} \left(\frac{\Omega_b h^2}{0.02} \right) \left(\frac{1+z}{7} \right)^{\frac{3}{2}} \left(\frac{n_{\text{HI}}}{n_{\text{H}}} \right), \quad (1.21)$$

where h is the value of H_0 in units of $100 \text{ km s}^{-1} \text{ Mpc}^{-1}$. Even a neutral fraction as small as $x_{\text{HI}} \equiv n_{\text{HI}}/n_{\text{H}} \approx 10^{-4}$ produces complete absorption ($\tau_{\text{GP}} \gtrsim 10$). Hence, Ly α -transmission regions in the spectra of high-redshift bright sources (typically quasars) provide information on the ionization state of the Universe. When a (mildly) neutral patch is extended in space, the superposition of absorptions at each location produces an extended suppression of the background flux. An impressive example of this is shown in Fig. 1.6, where the spectra of quasars are shown (in the observer rest frame) ordered by the source redshift, highlighting the onset of complete absorption due to neutral hydrogen in the IGM just blueward of the Ly α wavelength, the presence of transmission regions at later times (left side of the spectrum, smaller wavelengths), as well as the patchy topology of reionization, where different regions of the IGM are in different reionization states (compare e.g. the 13th and 14th spectra from the top, that refers to quasars at the same redshift but show very different transmission properties, left side of the spectrum).

More generally, equations 1.20 and 1.21 provide a link between τ_{GP} and n_{HI} . In the left panel of Fig. 1.7 we show the effective optical depth (i.e. the optical depth averaged over frequency bins in the QSO spectrum) as a function of redshift for different sightlines. The figure includes also the measurements coming from the Lyman- β (Ly β) and Lyman- γ (Ly γ) transitions of hydrogen, that behave similarly to the Ly α but can probe larger neutral fractions. At $z \lesssim 5.7$, the effective optical depth increases with redshift mostly driven by the $(1+z)^{3/2}$ factor coming from the density evolution. However, at larger redshifts there is a steep surge in τ_{eff} indicating a drastic increase of x_{HI} due to an incomplete reionization. Additionally, the scatter around the mean trend also grows with redshift, implying that different regions of the IGM are in dissimilar ionization states and providing another evidence for a patchy reionization process.

We have discussed so far about the HI Ly α line. However, a similar transition occurs in HeII and therefore can be used in a similar way to constrain the reionization of this species. An example of this is shown in the right panel of Fig. 1.7, where we show the evolution of the HeII Ly α effective optical depth. Both these techniques are intrinsically limited by the availability of background QSOs acting as sources of radiation. In the case of HeII, there is the additional complication of finding suitable sightlines, i.e. with unobscured QSO emission down to the HeII Ly α resonance wavelength and free of intervening HI clouds.

When the neutral fraction is significant ($x_{\text{HI}} \gtrsim 0.1$), the so-called red damping wing of the Ly α transition [113] can be exploited. Essentially, the natural width of the line and its Doppler broadening allow for absorption of photons with wavelength (slightly) lower than the Ly α one. This appears as a damping of the source spectrum (with optical depth $\tau_{\text{dw}} \sim x_{\text{HI}}$) just red-ward of the Ly α break and therefore provides a measurement of the hydrogen neutral fraction at the redshift of the source, provided a reliable knowledge of the original spectrum is available.

The opacity of the IGM to Ly α photons can also be tested using galaxies. For instance, measuring

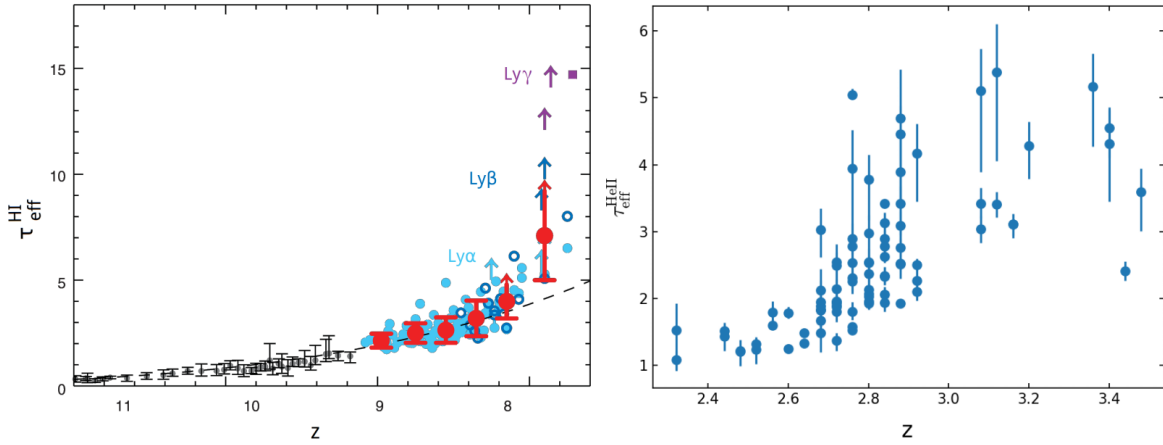


Figure 1.7: Left: Evolution of the HI effective optical depth. Filled circles, empty circles and squares are computed from the spectra shown in Figure 1.6 using the $\text{Ly}\alpha$, $\text{Ly}\beta$ and $\text{Ly}\gamma$ transitions, respectively. Red points with errorbars indicate the mean and standard deviation in each redshift bin at $z > 9$. Black points with errorbars are measurements from [112] (adapted from [110]). Right: Measurements of the HeII effective optical depth from [107].

the number density of $\text{Ly}\alpha$ -selected galaxies as a function of redshift, a sharp drop is seen at $6 \lesssim z \lesssim 7$ [114–119]. This has been interpreted as an evidence of boosted $\text{Ly}\alpha$ absorption from the intervening IGM.

CMB

A completely different type of constraints come from the CMB, through distortions of its original spectrum induced by the medium crossed before reaching the observer. Such alterations are imprinted in both the temperature and the polarization of the CMB, although the two are affected by different mechanisms and therefore act as complementary probes of reionization. Crucially, the CMB can only provide integral constraints on the EoR.

On large angular scales, the Thomson scattering of photons with the free electrons produced during the EoR has the net effect of suppressing the temperature fluctuations by a factor $e^{-\tau_{\text{CMB}}}$ and enhance the CMB polarization. The latter is a cleaner probe of reionization since temperature is affected by a wealth of additional effect, while polarization is not.

Reionization also induces additional small-scale temperature fluctuations as a consequence of the Doppler scattering of CMB photons induced by the relative motion of ionized structures (known as kinematic Sunyaev-Zeldovich effect). Finally, additional anisotropies include non-Gaussian features due to angular fluctuations in the optical depth, small-scales polarization fluctuations and linear-order Doppler anisotropies. These are, however, extremely challenging to detect. See [110] for a review.

Hydrogen spin-flip transition

The probes described above are either limited to single line of sights ($\text{Ly}\alpha$) or integral quantities (CMB). However, there is a promising tool that can enable a tomography of the reionization epoch. This is the hyperfine transition of neutral hydrogen, produced by a spin flip of the electron in the ground state (from aligned to anti-aligned with the proton spin in the case of emission and vice-versa for absorption). Despite being a dipole-forbidden line, the amount of HI available during reionization produces a measurable

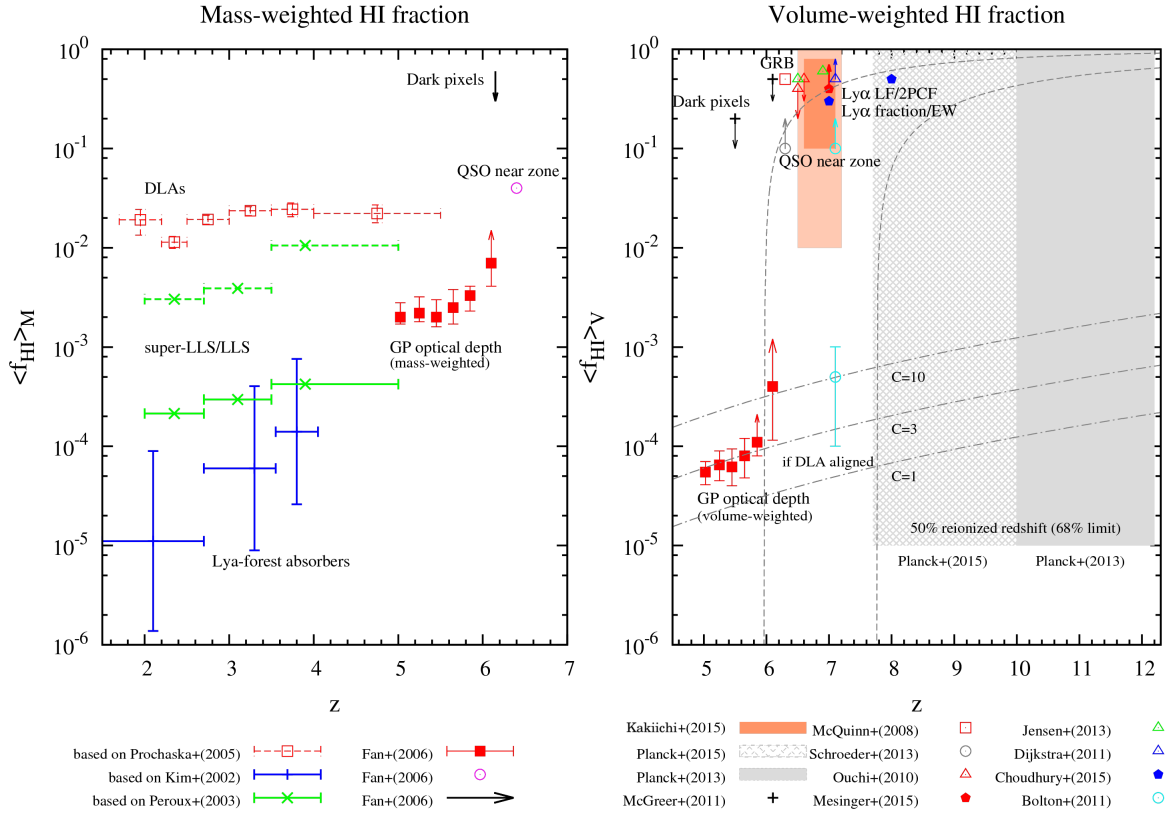


Figure 1.8: Compilation of constraints on the mass-averaged (left) and volume-averaged (right) neutral hydrogen fraction as a function of redshift [125].

signal (with rest-frame wavelength of $\lambda_{\text{hft}} \approx 21\text{cm}$) with very long lifetime $t_{\text{hft}} \approx 10^7$ yr. Interestingly, this line comes only from neutral regions and, therefore, carries important information on the topology of reionization.

Detecting the 21 cm signal from the EoR⁶ is a daunting effort, considering that galactic and extragalactic foregrounds are 4 – 5 orders of magnitude larger than the expected signal, requiring formidable effort and carefulness in removing them. While the Square Kilometer Array (SKA) radio telescope is being built for this purpose, current efforts (including e.g. the LOFAR [120], PAPER [121], MWA [122], SARAS 2 [123] and EDGES instruments) focus on detecting the all-sky average and the power spectrum of the hydrogen hyperfine transition during the EoR. These will provide invaluable information on the first sources of photons, as well as on the temperature of the gas at that epoch. A first tentative detection [124] has sparked a lot of interest for its unexpected features, namely the flattened shape, large amplitude, and frequency range.

In Figure 1.8 we show a compilation of constraints on the hydrogen reionization history coming from CMB [20, 126], Gunn–Peterson optical depth [127], dark pixels [128], Gamma Ray Burst afterglow [129, 130], quasars near zone [131, 132], Ly α luminosity function [125, 133], equivalent width distribution [134, 135], Ly α fraction [136], correlation function [137].

⁶ The 21 cm signal can be either seen in absorption or in emission against the CMB, depending on the relative temperature of the gas and of the CMB photons. Current models predict that, during the onset of the EoR, the 21 cm should appear in absorption.

1.5 Numerical simulations in astrophysics

The equations governing the evolution of dark matter, baryons and radiation, their interactions, as well as the formations of stars and other astrophysical phenomena are complex and no general analytical solution is available. Therefore, we rely on numerical methods to solve them, sampling the different components of the Universe with a finite number of resolution elements. Depending on the problem investigated, as well as the scale and the resolution of the simulations, physical processes occurring on scales smaller than a single resolution element can play an important role and have effects on much-larger regions. In order to be included, these phenomena need to be approximated using ‘sub-grid’ recipes (we describe the ones relevant for this Thesis in Section 1.5.4). Additionally, when dealing with cosmological scales we need to enforce the cosmological principle. This means, in particular, that proper boundary conditions for the simulation box need to be included. A typical choice is to use the so-called periodic boundary conditions (PBC), where each face of the simulation box is attached to the opposite one, producing a torus of the same dimensionality as the simulation box. This corresponds to ideally place infinite copies of the box to fill the space around it, so that material leaving the box from one of its faces gets re-injected from the opposite face. If the box is sufficiently large, distant region will be independent of each other and therefore mimic a infinite universe. Finally, modern codes are parallel, i.e. they distribute the computation across multiple processors in order to speed up the simulation. However, the communication between them is the main bottleneck for their performance. A popular strategy to tackle this issue is to build a space-filling curve (e.g. the Peano-Hilbert one, shown in the left panel of Fig. 1.9) that spans the entire simulation box. Each processor is then assigned all the particles within the volume spanned by a chunk of the curve. This ensures that the communication is, on average, minimal.

In this Thesis, we present simulation runs employing the `GADGET` [138, 139], `RAMSES` [140] and `RADAMESH` [141] codes, and therefore we will point out their characteristics while trying to give a general overview of simulation techniques in astrophysics. Additionally, in the range of phenomena investigated, `GR` plays no role apart from determining the ‘background’ spacetime of the Universe. For this reason, the simulation codes employed utilize a Newtonian approach within an expanding simulation space.

1.5.1 Gravity

Gravity is the dominant force on large scales and the only one acting on dark matter, the main mass component. Therefore, a crucial part of each simulation code is the computation of gravitational interactions. In virtually all cosmological codes (including those employed in this Thesis), dark matter is represented by a series of particles that sample its phase-space distribution.

The most straightforward and accurate method to compute the gravitational force is direct summation. However, this rapidly becomes computationally prohibitive in the case of large (i.e. with many particles) and long (i.e. on cosmological timescales) simulations. A first approximate method is the so-called particle-mesh (PM) algorithm, where the mass of particles is distributed on a grid. This is typically achieved using a cloud-in-cell (CIC) algorithm [142] (although alternative algorithms are available), where each particle is associated with a volume V_p equal to a grid cell and its mass is distributed on the grid according to the fraction of V_p that overlaps with each neighbour cell. The gravitational potential is computed on the grid by solving a discretized Poisson equation (in Fourier space for efficiency purposes). Finally, the gravitational force at each particle position is reconstructed by interpolation from the gridded potential. The major shortcoming of this method is that its resolution is limited by the size of the grid cells. In order to overcome this limitation, it is possible to rely on direct summation only for particles within the same grid cell, in what is called ‘particle-particle/particle-mesh’ (P^3M) approach [143]. Alternatively, a set of grids with increased resolution is placed in the regions of larger density and the Poisson equation

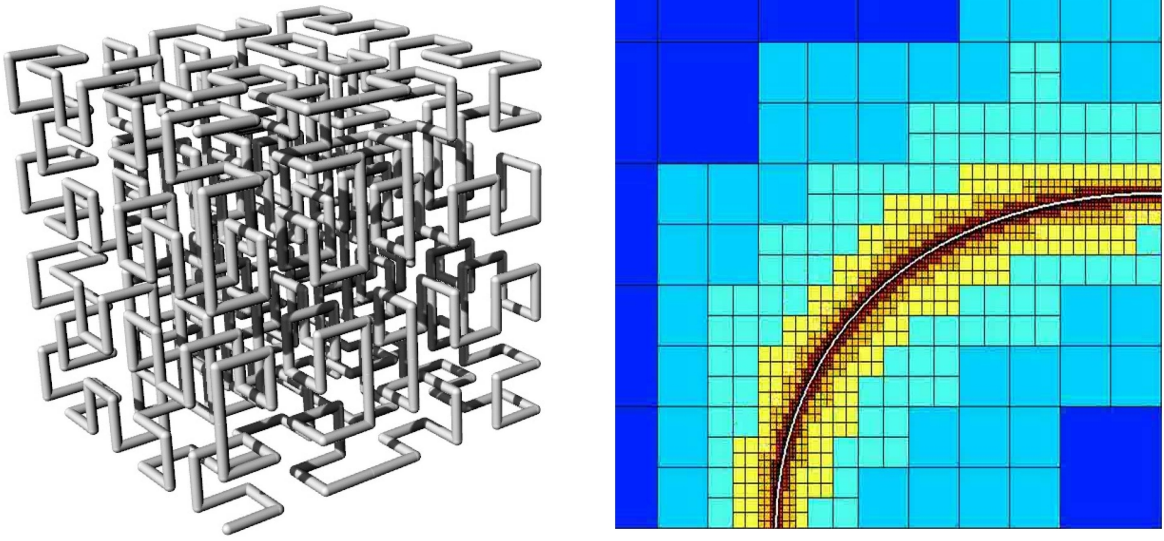


Figure 1.9: Left: example of Peano-Hilbert space-filling curve in 3D. The curve recursively fills the entire space. For visualization purposes, this is shown after the third iteration only. Right: 2D example of AMR structure, with cell color reflecting the refinement level, from low (dark blue) to high (white).

is solved on each level employing the Dirichlet boundary conditions imposed by the parent grid. The RAMSES code implements the latter with the additional feature that the high-resolution grids are adaptively changed during the simulation in order to follow the evolution of high-density region (an approach called Adaptive Mesh Refinement, or AMR, and exemplified in two dimension in the right panel of Fig. 1.9, [144]).

An alternative approach to the force calculation is provided by the hierarchical tree algorithm [145]. In this case, particles are grouped together in nodes. This is done recursively, starting from the root node containing all particles in the simulation and until each (leaf) node contains only one of them. The force acting on a given particle is obtained by direct summation over pseudoparticles representing entire nodes. The level of the nodes contributing to the sum, i.e. how many subdivision of the root node should be considered, is determined by the ratio between the node size and its (center of mass) distance to the particle, that should be smaller than an opening parameter. The shortcoming of this approach is the relatively large amount of memory required to store the tree information and the overhead time required to build, update and traverse the tree. Additionally, the implementation of periodic boundary conditions is not straightforward.

In the GADGET code, the long-range accuracy, speed and memory-efficiency of the PM algorithm is combined with the short-range precision and dynamical range of the hierarchical tree approach. This is achieved by smoothing the gravitational potential ϕ_{PM} computed by the PM algorithm with a Gaussian filter with radius R_{TPM} . The short-range potential coming from the hierarchical tree ϕ_{Tree} is compensated accordingly. This correspond to an exponential transition in Fourier space between the long- and short-range potential, i.e.

$$\tilde{\phi} = \tilde{\phi}_{\text{long}} + \tilde{\phi}_{\text{short}} = \tilde{\phi}_{\text{PM}} e^{-k^2 R_{\text{TPM}}^2} + \tilde{\phi}_{\text{Tree}} \left(1 - e^{-k^2 R_{\text{TPM}}^2} \right) \quad (1.22)$$

where a tilde indicates Fourier-transformed quantities.

Once the gravitational force is computed, the particle positions need to be updated. In both `GADGET` and `RAMSES`, this is achieved using a variant of the so-called kick-drift-kick Leapfrog algorithm, where the evolution over a timestep Δt is achieved by evolving the velocities for $\Delta t/2$, advance the positions for the full timestep and recompute the gravitational potential, and finally evolve the velocities for the remaining $\Delta t/2$ using the newly-computed potential. Both `RAMSES` and `GADGET` employ individual particle timesteps to focus the computational effort where is needed. In `GADGET`, individual timesteps are computed from the particle acceleration as a fraction of the global timestep set by the long-range forces (that vary on slower timescales). In `RAMSES`, the timestep follows the nesting level of the (innermost) grid each particle belongs to. The timesteps for each grid are computed using a Courant-Friedrich-Lewy condition that ensures the propagation of information within a cell is properly resolved, i.e. the timestep is smaller than the time information takes to cross the entire cell. The Leapfrog scheme provides significant advantages over similar-purpose algorithm. Being a second-order scheme, it is very fast but, when compared to schemes of the same order, it turns out to be more stable to numerical perturbations. This is due to its symplectic nature, that ensures no non-Hamiltonian perturbation (that can change the long-term behaviour of the system) is introduced⁷ [146].

Finally, the collisionless nature of dark matter allows particles to be indefinitely close, producing an unphysical⁸ divergent gravitational attraction. It is therefore customary to introduce a softening length ϵ that is added to the particle distance, so that the force between particles converge to a finite value for vanishing distance. This can be interpreted as treating each particle as a Plummer sphere⁹ with radius ϵ .

1.5.2 Hydrodynamics

Virtually all astrophysical phenomena involve baryons. Hence, a second crucial part of simulation codes is the solution of hydrodynamical equations. The governing (Euler) equations are:

$$\frac{\partial \rho}{\partial t} + \nabla \cdot (\rho \mathbf{v}) = 0 \quad (1.23)$$

$$\frac{\partial}{\partial t}(\rho \mathbf{v}) + \nabla \cdot (\rho \mathbf{v} \otimes \mathbf{v}) + \nabla p = -\rho \nabla \phi \quad (1.24)$$

$$\frac{\partial}{\partial t}(\rho e) + \nabla \cdot [\rho \mathbf{v}(e + p/\rho)] = -\rho \mathbf{v} \cdot \nabla \phi \quad (1.25)$$

where e is the specific energy of the fluid element. Additionally, p and e are related to the other properties via characteristic equations of state, that define the type of fluid. In principle, the effects of electric and magnetic fields, as well as radiation can be included, but they are often neglected since, in the majority of phenomena studied by means of cosmological simulations, have limited impact but significantly increase the computational cost of the simulation.

There are two conceptually different approaches to solve the Euler equations. In the Eulerian approach, the space is discretized and the fluid equations are solved for each grid point using a finite differences method, conceptually following the evolution of the fluid properties in a set of fixed spatial locations. Eulerian approaches provide a natural way to adaptively increase the resolution in high-density region

⁷ This is strictly true only when the timesteps of individual particles are equal. However, numerical tests show this is approximately true also for unequal timesteps [see e.g. 139]

⁸ This behavior is unphysical since each simulation particles is merely a sampler of the phase-space. In a particle-based interpretation of dark matter, each simulation particle represents a myriad of real particles, occupying a finite volume that prevent divergent interactions at the scale of the simulation particles.

⁹ The Plummer sphere model was originally devised to model globular clusters and features a spherically-symmetric density profile $\rho(r, \theta, \phi) = \frac{3M}{4\pi a} \left(1 + \frac{r^2}{a^2}\right)^{-\frac{5}{2}}$, where M is the total enclosed mass and a is the radius.

during the simulation run. However, the advantages of an adaptive grid comes at the price of large memory requirements and a complicated output format. This is the approach employed by the `RAMSES` code through an AMR structure. In the Lagrangian approach, the fluid is discretized and each resolution element is followed throughout the simulation solving the Euler equations for each individual element. Continuous quantities Q can be obtained using a smoothing kernel W as

$$Q(\mathbf{r}) \approx \frac{\sum_i^{N_{\text{nb}}} Q(\mathbf{r}_i) W(|\mathbf{r} - \mathbf{r}_i|) m_i}{\sum_i^{N_{\text{nb}}} W(|\mathbf{r} - \mathbf{r}_i|) m_i} \quad (1.26)$$

where N_{nb} is the number of neighbour particles considered, \mathbf{r} is the position where Q is evaluated, while \mathbf{r}_i and m_i are the position and mass of the i -th neighbour. The most common Lagrangian technique is named smoothed particle hydrodynamics [SPH, 147, 148] and is employed by `GADGET`. Lagrangian approaches don't require numerical derivatives, since any derivative is propagated to the smoothing kernel (see equation 1.26), which is an analytical function. The price for these features is that in SPH it is much harder to resolve shocks and underdense regions (e.g. the IGM) since the number of resolution elements is directly proportional to the density. Additionally, there is no easy way to adaptively increase the resolution during a simulation. In recent years, a hybrid approach has been investigated and successfully implemented. In moving-mesh codes, the grid over which the fluid equations are solved is allowed to deform following the motion of the fluid, naturally adapting to the evolution of fluid properties.

1.5.3 Radiative transfer

The effect of radiation on the gas is neglected (or very-coarsely modeled) in the majority of cosmological simulations. However in the study of specific phenomena (e.g. cosmic reionization), radiative-transfer effects play a major role and need to be properly accounted for. The governing equation of this process (often called the radiative-transfer equation) reads

$$\frac{dI_\nu}{ds} = -\alpha_\nu I_\nu + j_\nu + \frac{\mu_s}{4\pi} \int p(\hat{\mathbf{n}}_{\text{in}}, \hat{\mathbf{n}}_{\text{out}}) I_\nu(\hat{\mathbf{n}}_{\text{in}}) d\hat{\mathbf{n}}_{\text{in}}. \quad (1.27)$$

Here, I_ν is the specific intensity (or brightness), i.e. the radiant energy dE that crosses in time dt and with frequency ν an infinitesimal area dA subtending a solid angle $d\Omega$, while j_ν is the energy spontaneously emitted per unit volume, solid angle, time and frequency by matter traversed by the photon path ds through e.g. thermal emission, bremsstrahlung and decays of excited atomic states. Incident photons can trigger the production of additional identical photons in the process of stimulated emission, while radiation of the right frequency can be absorbed by electrons (that convert the photon energy into potential energy to transition into a higher-energy quantum state). The quantum probability for these processes is proportional to the specific intensity of the incoming radiation through the absorption coefficient α_ν , that is typical of the material and changes with frequency. Conventionally, α_ν is positive when absorption dominates and negative when stimulated emission is the prevailing mechanism. Finally, the integral term on the right-hand side represents photon scattering through a material-dependent coefficient μ_s and a phase function $p(\hat{\mathbf{n}}_{\text{in}}, \hat{\mathbf{n}}_{\text{out}})$ describing the change in the direction of photons from an incoming direction $\hat{\mathbf{n}}_{\text{in}}$ to an outgoing direction $\hat{\mathbf{n}}_{\text{out}}$.

Radiation traversing a medium where only absorption is relevant gets exponentially damped by a factor $e^{-\tau_\nu}$, where the optical depth is defined as $\tau_\nu \equiv \int_{s_0}^s \alpha_\nu(x) dx$. For a given frequency, a medium is said to be optically thin (or transparent) when the value of τ_ν over a typical path is smaller than unity. Conversely, if $\tau_\nu > 1$, the medium is optically thick (or opaque). The typical path a photon can travel

without being absorbed is called mean free path λ_{mfp} and, in a homogeneous medium, this equals $1/\alpha_\nu$. The optical depth can be expressed as a function of the column density $N = \int n \, ds$ (i.e. the number of atoms per unit area along its path) and the absorption cross section σ_ν , namely $\tau_\nu = N \sigma_\nu$.

The radiative transfer equation 1.27 can be solved analytically only in highly idealized cases. In realistic scenarios, we have to rely on numerical solutions. One of the most-accurate approaches is the Monte Carlo¹⁰ technique, where rays are propagated from the sources in random direction and they are used to compute the correct angular distribution of radiation in each resolution element of the simulation. The drawback of this method is that the number of rays required (i) increases rapidly with distance from the source, rendering them unsuited for cosmological application, and (ii) is determined by the smallest resolution element, resulting in a waste of computational time for multi-resolution simulations.

The RADAMESH code, used in Chapter 4, overcomes these issues by exploiting the time-reversal symmetry of physical laws. In particular, instead of isotropically propagate rays from the sources (ray-by-ray approach), it ‘back-propagates’ rays from every resolution element to each source (cell-by-cell approach) using an extension of the Amanatides and Woo[149] algorithm to the AMR structure employed by the code. This is repeated for multiple positions within each cell (ensuring a uniform sampling of the solid angle subtended by the cell through a rejection algorithm) until the physical properties converge. Additionally, this expensive Monte Carlo scheme is applied only to cells that require high precision, e.g. those where the medium properties change on small time scales, while other cells are processed through approximate numerical schemes¹¹. The code explicitly conserves the number of photons and employs a non-equilibrium solver to compute the chemical state of six different species (HI, HII, HeI, HeII, HeIII, e^-) as well as the IGM temperature. Cells are allowed to have individual timesteps, calculated as a fixed fraction of the minimum cell ionization time (obtained from equation 1.29 below). The grid structure is (de-)refined where needed following the recursive clustering algorithm of [150] and a refinement criterion involving the local photoionization rate, neutral fraction and optical depth. Finally, since scattering processes are relevant only at densities much larger than the one found in the inter-galactic medium, they are ignored in the cosmological radiative transfer.

Whenever an atomic species i interacts with radiation, it can be ionized if the photon energy $E_{\text{ph}} = h_p \nu$ is larger than its ionization threshold $E_{i,\text{thr}}$. The amount of such events per unit time and unit volume is given by the photoionization rate

$$\Gamma_i(\mathbf{x}) = \int_0^{4\pi} \int_{E_{i,\text{thr}}/h_p}^{\infty} \sigma_i(\nu) \frac{I_\nu(\mathbf{x})}{h_p \nu} \, d\nu \, d\Omega, \quad (1.28)$$

where $\sigma_i(\nu)$ is the ionization cross-section. The photon energy in excess of the ionization threshold is converted into kinetic energy of the unbound electron, that therefore heats up the medium. The rate of heating due to this process is quantified by the photoheating coefficient $\mathcal{G}_i(\mathbf{x})$. In radiative transfer simulations these quantities are evaluated for each resolution element starting from the radiation intensity field at its location. These values are used to compute the evolution of the atomic species fraction ($x_i \equiv n_i/n_{i,\text{tot}}$, where $n_{i,\text{tot}}$ is the number density of atoms of the same element as i regardless of their

¹⁰ These methods employ random numbers to build a statistical estimation of physical quantities. They are named after the town of Monte Carlo, famous for hosting the Grand Casino, where randomness is the rule.

¹¹ In particular, whenever the optical depth in one of the traversed cells is below a minimum threshold the Monte Carlo calculation is replaced by a faster optically-thin approximation. Similarly, a maximum threshold in optical depth determines when the traversed cell should be considered optically thick and treated assuming $\tau_{\text{cell}} \approx \infty$. Finally, the total column density is first evaluated on the cell vertices and, in case the difference between these 8 values is small, a fast linear interpolation is used in place of the full ray-casting algorithm.

ionization state). This can be done (iteratively) solving

$$\frac{dx_i}{dt} = -x_i\Gamma_i - n_e x_i \beta_i C + n_e x_{i+1} (\alpha_i + \epsilon_{i,\text{diel}}) C \quad (1.29)$$

where $i + 1$ is an abuse of notation indicating the ion obtained removing an electron from species i (if possible, otherwise $x_{i+1} = 0$), n_e is the number density of free electrons, $C \equiv \langle n^2 \rangle / \langle n \rangle^2$ is the gas clumping factor and β_i , α_i and $\epsilon_{i,\text{diel}}$ are (temperature-dependent) radiative recombination, collisional ionization and dielectric recombination¹² coefficient, respectively. The photoheating contribution of all species acts as an additional source of heat, that is evaluated together with the cooling function (see Section 1.5.4) to determine the temperature evolution of the gas.

1.5.4 Subgrid physics

Often in numerical simulations, phenomena taking place on sub-resolution scales affect much larger (resolved) regions. A familiar example is the star-formation process. Stars form in high-density cores that are typically much smaller than the resolution element of cosmological (or galaxy-scale) simulations, but the radiation they produce and the material they eject can travel relatively-long distances and affect large regions of the interstellar medium. Other examples of subgrid processes include supernova explosions, metal diffusion, chemistry, and cooling. In the following, we will describe their numerical treatment.

Star formation

Star formation is ubiquitous in the Universe. Unfortunately, the scales where it takes place are too small to be resolved in cosmological (or galactic) numerical simulations. It is customary to approximate this process employing an empirical three-dimensional variant of the Kennicutt-Schmidt [151, 152] relation, that observationally relates the gas surface density (Σ_{gas}) to the star formation rate (SFR) per unit area, i.e. $\Sigma_{\text{SFR}} \propto \Sigma_{\text{gas}}^n$, with $n \approx 1.4$. In particular, resolution elements with temperature below an adjustable threshold, density above a user-defined parameter, and lying within a convergent flow (i.e. $\nabla \cdot \mathbf{v} < 0$) can (potentially) undergo star formation. The effective conversion from gas to stars occurs stochastically with probability proportional to the star-formation rate per unit volume, given by [153]

$$\dot{\rho}_{\text{SFR}} = \eta \sqrt{4\pi G \rho^3}. \quad (1.30)$$

The dimensionless parameter η sets the efficiency of star formation per free-fall time. Whenever the conversion occurs, part of the gas is transformed into a stellar particle, representing an entire population of stars with the same age and chemical composition, inherited from the parent gas. The properties of the stellar particle and its feedback on the surrounding medium are computed in a statistical way assuming an initial mass function (IMF) for the population.

Supernova feedback and stellar winds

Stars with a mass at least 8 times larger than the Sun end their life in a supernova explosion. The rate of such events as well as their energy and metal injection in the medium are computed for each stellar particle using its IMF and stellar population synthesis models.¹³ The total energy injected by supernovae

¹² Note that this coefficient vanishes whenever an atomic species contains only one bound electron.

¹³ An exception is represented by supernovae Ia, whose origin is still debated. For this reason, approximate models have been developed.

is split into a kinetic part that increases the medium velocity and a thermal contribution boosting the temperature. Energy and metals are distributed in the surrounding medium with a kernel peaked at the stellar particle position.

Even before exploding as supernovae, stars strongly influence the surrounding environment, especially during the asymptotic giant branch and OB phases, through stellar winds, i.e. material outflowing from their surface and depositing energy, momentum and metals in the medium. The effect and properties of stellar winds are computed in a similar fashion as the supernova feedback.

Metal diffusion

The exchange of metals between neighbour resolution elements is approximated using a model for turbulent diffusion [154] that implements a diffusion equation for the metal concentration.

Cooling

Atoms and molecules act as cooling agents, radiating away the thermal energy of the gas. However, self-consistently including this effect in the simulations is impractical from a numerical point of view. Therefore, gas cooling is typically implemented using a cooling function Λ . This is, essentially, a multidimensional grid of cooling rates for different combinations of gas density, temperature and metallicity, pre-computed using a large number of atomic and molecular species and assuming local equilibrium between recombination and collisional ionization. During the simulations, the cooling rate for each resolution element is obtained from Λ through interpolation. Note that heating processes are included in Λ , so that it represents a *net* cooling and can assume negative values. Additionally, to ease the calculations, the so-called nebular approximation is employed, where any excited state is always followed by a rapid radiative cascade into the ground electronic state, so that all species are assumed to always be in the ground electronic state.

Radiation

Stars and AGNs are sources of copious radiation during their life, that transports energy and momentum on long distances, potentially changing the dynamics of the gas. However, the fraction of photons escaping into the surrounding medium strongly depends on the small-scale dense structures around the source. These are usually unresolved in cosmological simulations. Additionally, radiative-transport is very computationally expensive. For these reasons, the overall emission from sources is approximated using a spatially-uniform background with time- and frequency-dependent intensity that is calibrated against observations (and therefore independent on the unresolved dense gas). Additionally, since the vast majority of gas in the Universe is composed by hydrogen and helium, only frequencies close to the ionization thresholds of HI, HeI and HeII are relevant for gas heating¹⁴ and therefore only the ultra-violet (UV) part of the background is relevant.

Using a UV background (UVBG) to model the radiation from all sources in the box is a valid approximation only when the mean free path of photons is much larger than the average distance between sources, so that spatial variations in the source distribution are smoothed out. This correspond to assuming all the gas in the Universe is optically thin. In the case of UV photons, this occurs only when the majority of the Universe is highly ionized. If this is not the case, photons are absorbed very close to their source.

¹⁴ Ionizing photons deposit the energy in excess of the ionization threshold as electron kinetic energy that, through collisions, increase the temperature of the gas. However, the cross section for ionization is peaked at the ionization energy and, hence, only radiation with frequency close to the ionization frequency of the gas significantly contributes to the photoheating.

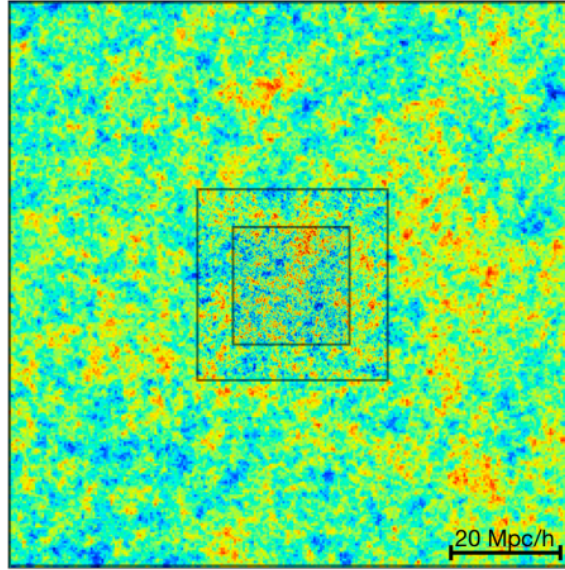


Figure 1.10: Example of nested initial conditions generated with the music code [155]. The resolution increases from the outer envelope toward the innermost patch.

Therefore, a UVBG can not be a good approximation during the Epoch of Reionization, where the UV radiation field is highly inhomogeneous. On the other hand, after it the UV field is well approximated by a uniform background. For this reason, we have employed a UVBG model for the simulations presented in Chapters 2 and 3, where the details of the EoR can be neglected, while in Chapter 4 we employed more sophisticated techniques for the treatment of the radiation field, that are described in the Chapter as well as in Section 1.5.3.

1.5.5 Initial conditions

We have, so far, described how to numerically evolve dark matter, gas and stars in a realistic setting. However, a crucial ingredient for simulations are the initial conditions. In a cosmological context, one would ideally start the simulation from the Big Bang. Unfortunately, we do not have a full comprehension of such event and, therefore, it is currently impossible to safely characterize the state of the Universe at that epoch. The earliest source of information we have access to is the CMB (see Section 1.3). However the angular resolution of current CMB experiments (first and foremost, the *Planck* satellite) corresponds to physical scales of approximately 15 kpc (comoving), while simulations aim at modeling also much smaller scales. For this reason, we employ the information encoded in the CMB to reconstruct the statistical properties of the fluctuations on smaller scales. In particular, we use our knowledge of the content and forces at play in the (early) Universe to construct a set of random initial conditions that are statistically compatible with the observed CMB, but extend to much smaller scales.

From a practical point of view, the initial (i.e. produced by inflation) matter power spectrum is evolved until the desired initial redshift of the simulation z_{ic} (typically in the range $z_{\text{ic}} \approx 100 - 50$, a trade-off between accuracy and computational efficiency). Then, the Fourier modes of the density are computed on a grid by sampling two Gaussian distributions (for the real and imaginary part of the modes, respectively) with zero mean and variance equal to the power spectrum at the corresponding k . The (Fourier-transformed) density, is used to compute the potential ϕ on the grid and to determine

the displacement $\mathbf{L}(\mathbf{x}, t)$ of an uniform, isotropic set of particles (with pre-initial position $\mathbf{x}(0) = \mathbf{q}$ and peculiar velocities $\mathbf{v}(0) = 0$) that uniformly sample the simulation space. Conceptually, evolving a distribution of particle in a potential is a simulation in itself. However, at such high redshift the density perturbations are very small and therefore the first-order Lagrangian perturbation theory (or 1LPT, see Section 1.3) is a very good approximation, and hence:

$$\mathbf{x}(t) = \mathbf{q} + \mathbf{L}_{1\text{LPT}}(\mathbf{q}, t) = \mathbf{q} - D_+(t)\nabla_{\mathbf{q}}\phi(\mathbf{q}, t), \quad (1.31)$$

$$\mathbf{v}(t) = \frac{d}{dt}\mathbf{L}_{1\text{LPT}}(\mathbf{q}, t) = \frac{d}{dt}\left[-D_+(t)\nabla_{\mathbf{q}}\phi(\mathbf{q}, t)\right]. \quad (1.32)$$

The accuracy of 1LPT declines with decreasing z_{ic} , since perturbations grow and the perturbative approximation progressively breaks down. In order to extend this approach to smaller z_{ic} and, hence, save computational time, it is possible to include the next-to-leading order (the so-called 2LPT), i.e.

$$\mathbf{L}_{2\text{LPT}}(\mathbf{q}, t) \simeq -D_+(t)\nabla_{\mathbf{q}}\phi(\mathbf{q}, t) + \left[\frac{3}{7}D_+(t)\right]^2 \nabla_{\mathbf{q}}\Phi(\mathbf{q}, t) \quad (1.33)$$

$$\nabla_{\mathbf{q}}^2\Phi(\mathbf{q}, t) = -\frac{1}{2} \sum_{i,j} \left[\left(\frac{\partial^2 \phi}{\partial q_i \partial q_j} \right)^2 - \frac{\partial^2 \phi}{\partial q_i^2} \frac{\partial^2 \phi}{\partial q_j^2} \right]. \quad (1.34)$$

The procedure described produces initial conditions with uniform resolution. While this is ideal for studying phenomena taking place throughout the simulation box, in some cases it is useful to focus the computational effort in a single region of interest (e.g. a single galaxy). In this ‘zoom-in’ simulations, the initial conditions have boosted resolution in a patch of the simulation box. In order to reduce numerical artifacts produced by the discontinuity in the resolution, a smooth transition is created by producing a set of nested layers with intermediate resolution around the region of interest. An example of of this configuration is shown in Fig. 1.10. Zoom-in initial conditions are produced by recursively applying the algorithm described above with suitable boundary conditions.

1.6 Open questions addressed in the Thesis

The main focus of this Thesis is the interplay between large and small astrophysical scales. In particular, we focus on two problems, namely the assembly bias effect on the formation of structures and cosmic reionization. In the former, the cosmic web influences the internal properties of single DM haloes and galaxies, while in the latter small sources change the properties of the IGM on very large scales through radiative feedback. Additionally, we also provide the first-ever prediction for the radial acceleration relation of Λ CDM satellite galaxies.

1.6.1 The impact of assembly bias on satellite galaxies

The assembly bias is an effect inherent to DM haloes and, therefore, has historically been investigated using DM-only simulations. For this reason, its effect on the galaxies hosted by these haloes has not been investigated until recent times [156]. In Chapter 2 we start by revising the typical evolution of satellite galaxies (Section 2.3) and then move on to statistically compare the properties of satellite population embedded in haloes with different formation time (Section 2.4). Finally, we investigate the effect of the environment on satellite galaxies, describing how they can be used to observationally unveil the assembly history of the parent DM halo (Section 2.5).

1.6.2 Prediction of the radial acceleration relation for Λ CDM satellite galaxies

Satellite galaxies are observationally found to deviate from the RAR followed by more-massive objects [53]. In Chapter 3 we thoroughly investigate the predictions of the Λ CDM model (Section 3.4). We additionally exploit numerical simulations to examine secondary dependence of the RAR and make use of this knowledge to devise an observational test able to tell apart the Λ CDM and MOND models (Section 3.5). Finally, we unveil the mechanisms establishing such relation and governing its evolution with time (Section 3.6).

1.6.3 The role of quasars in cosmic reionization

The recent detection of a large number of candidate faint quasars questions their role in hydrogen reionization. In Chapter 4 we employ hydrodynamical simulation post-processed with a radiative-transfer code (Section 4.2) to study the effect of an enhanced QSO contribution at high-redshift on the global properties of the EoR (Section 4.3). Additionally, we produce synthetic observations of the Ly α forest of HI and HeII and use them to devise ways to gauge the contribution of high- z faint QSOs (Section 4.4).

The effect of Halo Assembly on the Satellite Population¹

2.1 Introduction

The standard model of cosmology is based on conventional physics and assumes that the dominant terms of the stress-energy tensor are a cosmological constant and cold dark matter. In this Λ CDM scenario, self-gravitating structures form hierarchically through mergers of smaller units. The end product of this process is a collection of dark matter haloes containing a large amount of substructures that are the vestiges of the merging process. In fact, these ‘satellites’ enter, orbit and get progressively stripped of their outer layers while inside the host halo.

It was originally thought that substructures would be quickly erased but the advent of high-resolution N -body simulations revealed that this is not the case [e.g. 158–160]. Comparing the computer models with the population of Milky-Way satellites posed several challenges to the Λ CDM model [see e.g. 161–163, for a review]. Recent studies have characterized the detailed statistical properties of the surviving satellites [164–166] and shown that they are very sensitive to gas and star-formation physics [e.g. 167–173].

This article is the last in a series of three introducing a numerical project named Zooming On a Mob of Galaxies (ZOMG). ZOMG uses a suite of zoom N -body plus hydrodynamical simulations to study how the cosmic environment regulates the evolution and properties of galaxy-sized dark-matter haloes as well as of their baryonic content and substructures. It is well known that haloes of the same mass show different clustering properties depending on their formation history, a process usually dubbed ‘assembly bias’ [90, 91, 174–176]. A long-standing challenge in theoretical cosmology has been to understand the origin of this phenomenon, especially for galaxy-sized haloes. Building upon the early work by [177], in [98, hereafter paper I], we have shown that haloes stop growing in mass once they are embedded in prominent filaments of the cosmic web that are thicker than the halo diameter. The dark matter (DM) in these haloes preferentially follows tangential orbits due to the gravitational pull of the filament that alters the trajectories of the infalling material before it reaches the halo. Conversely, haloes sitting at the knots of the cosmic web (the regions towards which numerous thin filaments converge) grow by accreting material from the surroundings along quasi-radial orbits. The accretion history and the internal

¹This chapter has been published in [157]. The notation has been adapted to match the rest of this Thesis.

dynamics of galaxy-sized haloes are thus intimately related to the halo location within the cosmic web, hence the assembly bias. It is natural to ask whether the fate of the gas component also depend on the halo assembly history and position. In [156, hereafter paper II], we have addressed this question showing that the properties of the central galaxy are largely insensitive to the collapse time of the host, with the exception of the thickness and age of its stellar disc (both increasing for haloes with stalled growth in filaments). Finally, in this work, we investigate the impact of the halo assembly history (and thus of cosmic environment) on the properties of the satellite population.

Several related lines of research have been recently pursued using numerical simulations. Although they have identified the existence of deep interrelationships between halo environment, matter accretion and the final characteristics of the substructures, a clear picture has not yet emerged. The connection between cosmic filaments and the kinematics of substructures has been particularly explored in the literature. Infall along filaments seem to produce groups of subhaloes whose orbital angular momenta align with the halo spin in both possible rotating directions [178]. Even the survival lifetime of substructures seem to depend on whether they have been accreted along a filament or not [179]. It has been concluded that the ordered accretion of substructures along filaments is the prime reason for the existence of flattened configurations of satellite galaxies which are coherently rotating [178, 180, 181]. Some authors, however, argue that such layouts can only exist when at most two filaments feed the host halo [182]. Others find that thin planes of satellites are only hosted by haloes with very concentrated mass density profiles which form early on when filaments are narrower and accretion is thus more focused [183]. In general, the spatial distribution of the satellites seem to align (to some extent) with the large-scale distribution of matter surrounding the host halo and even with the halo shape [184]. In fact, substructures preferentially fall in along the main principal axis of the inertia tensor [185].

In this paper, we use the high-resolution simulations presented in paper I and paper II to study how the population of satellite galaxies is influenced by the halo assembly history. The article is structured as follows. In Section 2.2, we describe the main features of the ZOMG simulations and the analysis performed for this work. The detailed time evolution of a few substructures is described in Section 2.3 while, in Section 2.4, we study the statistical properties of the satellite populations providing comparisons with previous numerical studies and observations. In Section 2.5, we tackle the issue of how the process of halo assembly impacts the kinematics and the final spatial configuration of the satellites. A summary of our results and conclusions are presented in Section 2.6.

2.2 Numerical Methods

We summarize here the main properties of the ZOMG simulations and discuss the substructure analysis which forms the main focus of the paper. Further details can be found in papers I and II.

The ZOMG project includes a set of high-resolution N -body and hydrodynamical simulations that follow structure formation in a model universe with $\Omega_m = 0.308$, $\Omega_\Lambda = 0.692$, $\Omega_b = 0.0481$ and $h = 0.678$ [126]. Linear density perturbations are characterized by the spectral index $n = 0.9608$ and the power-spectrum normalization $\sigma_8 = 0.826$. All simulations cover the same periodic cubic box with a side of $50 h^{-1}$ Mpc. Initial conditions are generated at redshift $z = 99$ using the music code [155] and employing second-order Lagrangian perturbation theory to shift particles from a uniform Cartesian grid.

To isolate the host haloes of present-day L_* galaxies, we make use of a parent N -body run containing 512^3 identical particles and select a few objects with masses $M_h \sim \text{few} \times 10^{11} h^{-1} M_\odot$ at $z = 0$ that we then re-simulate at very high-resolution using the multimass zoom technique. On top of the mass selection, we apply a further criterion based on the assembly history of the haloes that we characterize in terms of the ‘collapse time’ introduced in [187]. In brief, we trace the particles that form a halo at $z = 0$

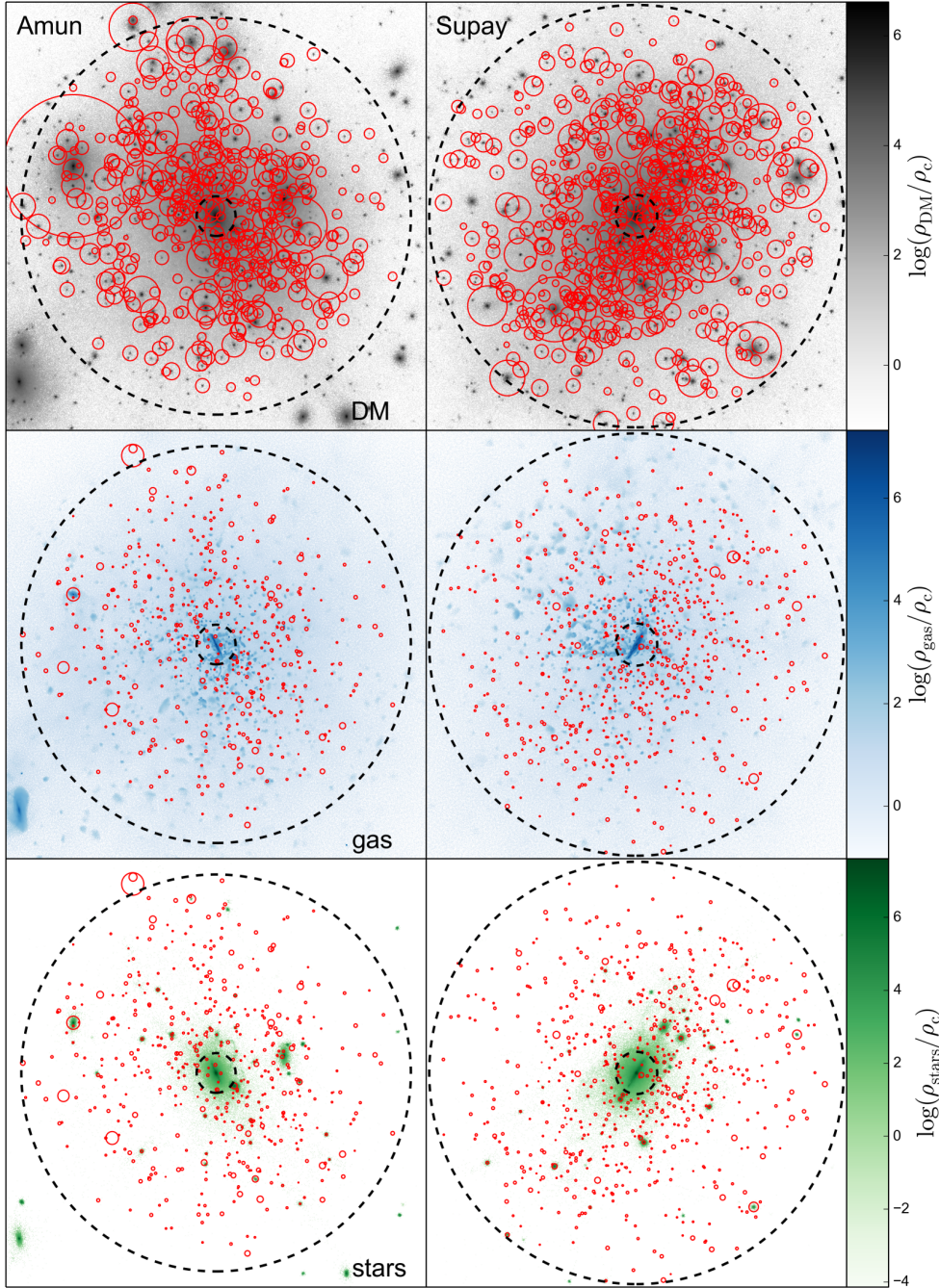


Figure 2.1: Dark-matter, gas and stellar distributions (from top to bottom) for two of our re-simulated haloes at $z = 0$. Each panel shows the projection along one axis of the simulation particles contained within a cube of side $310 h^{-1}$ kpc centred on the corresponding halo. Particles are colour-coded according to the local density computed using a standard SPH-like kernel with 64 neighbours (of the same species), normalized by the critical density of the universe ρ_c . The outer and inner dashed circles indicate the halo radius R_h and the radius of the central galaxy R_g , respectively. Substructures are highlighted with solid red circles whose radius reflects the subhalo radius found by AHF (top panels) or the location of the maximum circular velocity (middle and bottom panels). Note that dense DM clumps that are not surrounded by a red circle are located outside the halo radius although they might give the impression to be within R_h due to projection effects.

Table 2.1: Properties of the re-simulated haloes at $z = 0$. From left to right, the columns give: the name, the mass (M_h), the radius (R_h), the scale radius (r_s) obtained fitting the radial mass-density profile with the Navarro-Frenk-White (NFW) formula [186], the expansion factor at collapse time (a_c), the total number of substructures (N_{sh}), the number of substructures with gas (N_{gas}), the number of substructures with stars (N_*), the fraction of M_h in substructures (f_{sh}), the mean fraction of the baryonic content of substructures identified at $z = 2$ that migrates to the central galaxy by $z = 0$ ($\langle f_{disc} \rangle$) and the colour associated to the halo throughout the paper.

Halo name	$M_h [10^{11} h^{-1} M_\odot]$	$R_h [h^{-1} \text{kpc}]$	$r_s [h^{-1} \text{kpc}]$	a_c	N_{sh}	N_{gas}	N_*	f_{sh}	$\langle f_{disc} \rangle$	colour
Abu	4.1	151	3.13	0.968	382	4	52	0.109	0.03	—
Amun	3.5	144	7.41	>1.00	477	4	73	0.100	0.05	—
Supay	4.3	153	5.05	0.404	647	3	97	0.067	0.09	—
Siris	2.3	124	3.02	0.333	228	1	32	0.067	0.03	—

back in time and compute the evolution of their tensor of inertia. Given the inertia ellipsoid, we rigidly rescale it so that it always contains the final mass of the halo and we calculate its volume $V(t)$. This procedure was conceived to follow the evolution of the outermost matter shell forming the halo at $z = 0$, the collapse of which ultimately determines the halo assembly time. The function $V(t)$ initially increases due to the Hubble expansion, reaches a maximum (that can be used to define the epoch of turnaround) and generally decreases afterwards until it starts oscillating around a constant value indicating virialization (actual examples are shown in Fig. 1 of paper I). The collapse time of a halo, t_c (or the corresponding redshift z_c and expansion factor a_c), is defined as the moment at which the volume stabilizes (see paper I for details regarding the practical implementation of this calculation). Haloes with fixed mass in the parent run show a broad range of collapse times. To maximize the differences among the re-simulated haloes and better recognize the effects of their assembly histories, we only pick objects in the tails of the distribution. For the N -body (DM-only) runs (see paper I), we thus randomly pick 5 ‘stalled’ ($z_c > 1$) and 2 ‘accreting’ ($z_c \lesssim 0$) objects among the haloes of the selected mass identified in the parent simulation at $z = 0$. For the much more time consuming hydrodynamical simulations (see paper II), instead, we only consider 2 haloes for each class. We adopt the nomenclature of papers I and II where each re-simulated halo is named after an ancient god, sharing the initial letter of its name with the class it belongs to (i.e. ‘S’ for stalled and ‘A’ for accreting haloes).

The re-simulations are carried out using a modified version of the tree-particle-mesh smoothed particle hydrodynamics (SPH) code PGADGET-3 [139]. Our hydrodynamic runs include radiative cooling, star formation and stellar feedback, galactic winds, a multi-phase interstellar medium [188] and an ultraviolet background active from $z \sim 11$ that reionizes hydrogen in the intergalactic medium by $z \sim 6$ [189]. In all cases, we achieve an effective resolution of 4096^3 computational elements in the region of interest (roughly extending up to three times the halo radius), corresponding to particle masses of $m_{DM} = 1.31 \times 10^5 h^{-1} M_\odot$ and $m_{gas} = 2.43 \times 10^4 h^{-1} M_\odot$ for DM and gas, respectively. Each gas particle can experience up to two episodes of star formation, in each of which a mass $m_{gas}/2$ is converted into a stellar particle. Our runs extend to $z = 0$. We save a few snapshots at early times plus one every 20 Myr after redshift $z = 9$, for a total of 682 output files.

We identify gravitationally bound objects and their substructures using the AMIGA HALO FINDER [AHF, 190, 191]. This software initially defines haloes as spherical regions with a mean matter density of 200 times the critical density of the universe, $\rho_c(z)$, and then iteratively purges them of the (unbound) particles that move faster than 1.5 times the escape velocity. The halo radius, R_h , and mass, M_h , are defined using the smallest sphere enclosing all the bound particles. We conventionally identify the ‘central galaxy’ of each halo with the innermost region of radius $R_g = 0.1 R_h$ [e.g. 192]. Following [193], we also consider

a second definition for the halo boundary by locating a sharp steepening of the radial mass-density profile. [194] and [195] argued that such radius correspond to the first apocentre of recently accreted matter and therefore dubbed it as the ‘splashback radius’, R_{spl} . Contrary to the halo radius, R_{spl} is parameter free and does not suffer from pseudo evolution due to change of ρ_c with time.

We use the built-in function of AHF to construct halo merger trees. The main progenitor of a halo is selected maximizing the merit function $N_{i \cap j}^2 / N_i N_j$, where N_i and N_j denote the number of particles in the progenitor and the descendant in two consecutive snapshots and $N_{i \cap j}$ is the number of particles they share.

AHF automatically detects substructures as density peaks within a main halo. Their edge is initially determined as the minimum of the radial density profile and then adjusted to the radius of the smallest sphere enclosing all bound particles. Note that we do not consider higher levels of (nested) substructures (i.e. sub-subhaloes are not distinguished from their host subhaloes). Substructures are dynamic entities that continuously accrete and loose material. When studying their evolution, we follow all the particles they are made of at the time they reach their maximum mass (typically, right before entering the host).

Fig. 2.1 gives a visual impression of two of our re-simulated haloes and of their substructures. The main properties of the four haloes analyzed in this paper are listed in Table 2.1. These data are extracted from the hydrodynamic simulations, corresponding results for the N -body runs can be found in Table 1 of paper I.

2.3 Satellite evolution

In this section, we exploit the excellent time- and mass-resolution of the ZOMG simulations to describe the evolutionary path of a few typical substructures. This study helps the reader recognize the complex phenomenology of satellite-host interactions and us introduce several key concepts that will be used in the remainder of the paper. Ultimately, we determine the amount of material that satellites shed to their host halo and its central galaxy.

2.3.1 Trajectories and dynamics

We conventionally define the accretion redshift of a satellites, z_{ac} , by identifying the instant when, for the first time, AHF associates it with a host halo. The subsequent fate of the satellite is regulated by the interplay between several physical mechanisms [e.g. 196–198, and references therein]. Gravitational interactions between the satellite and the diffuse material that makes up the host produce a net drag known as dynamical friction. As a result, the satellite loses energy and angular momentum and its orbit decays towards the central region of the host where the gravitational potential reaches its minimum value. Along the way, the satellite constantly loses matter from its outer parts due to the action of tidal forces (tidal stripping). The ejected material initially forms leading and trailing streams stretching for large distances compared with the core of the satellite. Later on, these tidal tails evolve into approximately spherical shells and eventually phase-mix with the diffuse component of the host halo. In the CDM scenario, most satellites accrete on to their hosts following highly eccentric orbits and thus experience time-varying tidal forces. At each pericentric passage, when tides become particularly strong, the satellite expands, gains kinetic energy and rearranges its internal structure (tidal heating). Its lower binding energy makes it prone to further mass loss via tidal stripping (and ram pressure stripping for the gas component). Since the orbital decay rate depends on the satellite mass, all these effects are highly interconnected. The detailed evolution thus depends on the initial mass and concentration as well as the orbital parameters of the satellite.

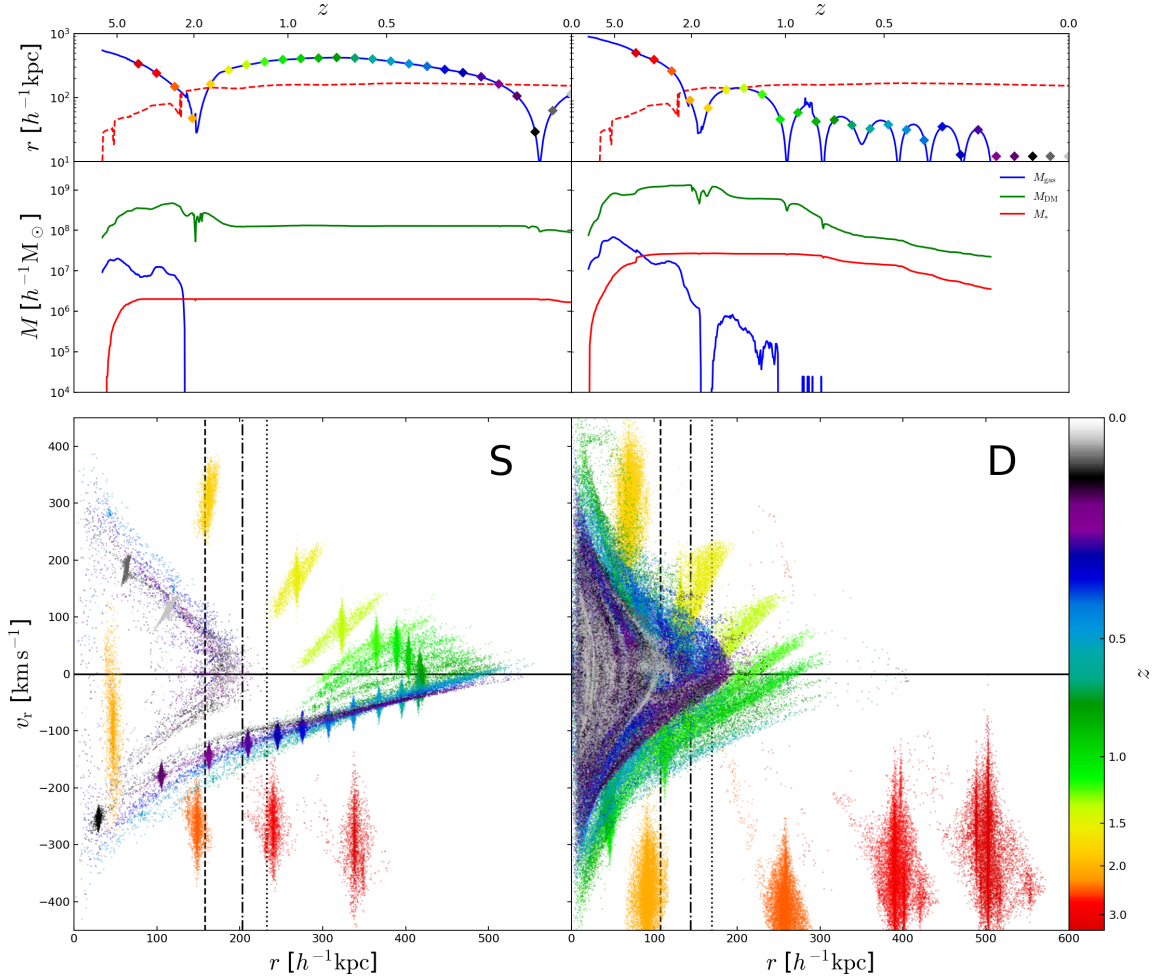


Figure 2.2: Evolution of different properties in two of the most massive subhaloes in our simulation suite (the left one belongs to Supay while the right one is part of Amun). Top: evolution of the distance r from the host. The dashed red line denotes the host radius. The diamond symbols indicate the redshift of the steps plotted in the bottom panels. Middle: evolution of the DM, gas and stellar mass of the substructure (green, blue and red line, respectively). Bottom: radial phase space distribution of all particles. The colour encodes the redshift, in steps of 500 Myr. The substructure in the left panel has survived until $z = 0$ while the one in the right panel has been totally disrupted. The halo radius, the splashback radius and its predicted (median) n value for haloes with the same mass and accretion rate [following 195] are shown at the redshift of the first apocentre using dashed, dot-dashed and dotted lines respectively.

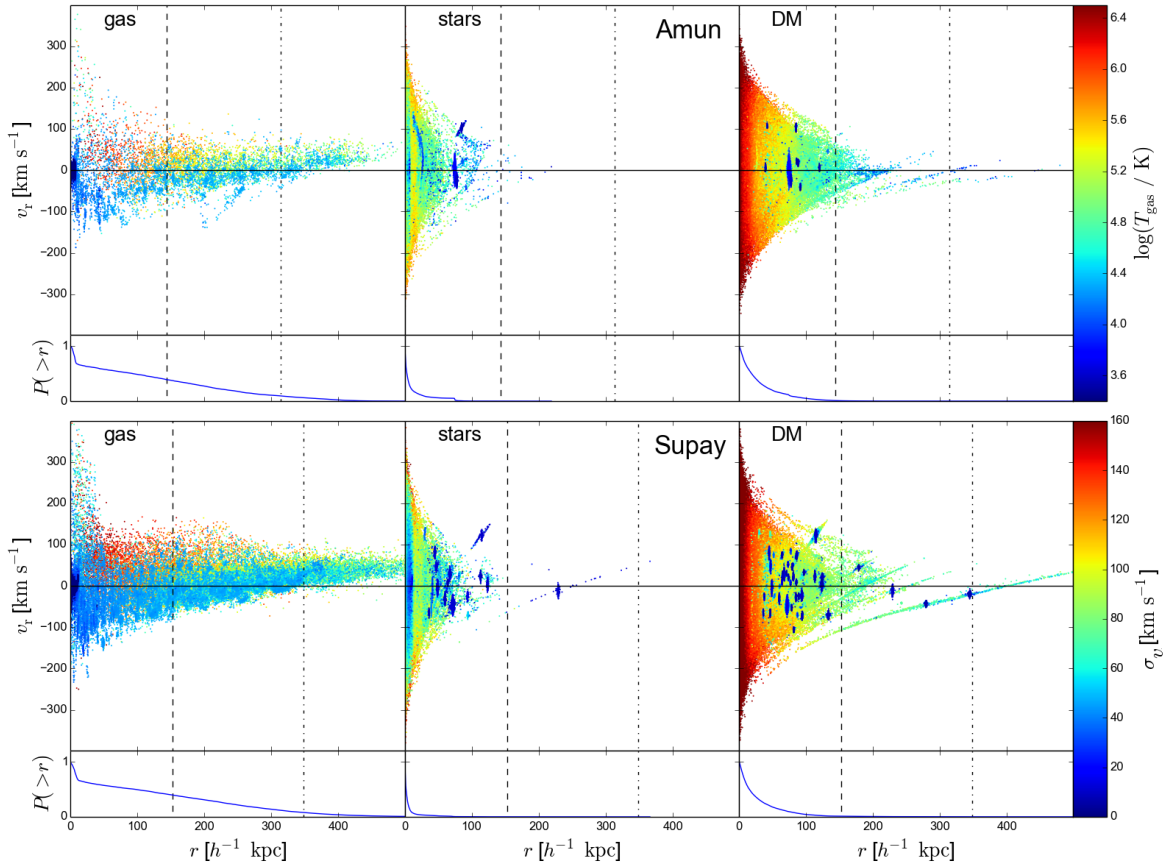


Figure 2.3: Radial phase space distribution at $z = 0$ of particles of different species belonging to the 100 most massive subhaloes identified at $z = 2$ in Amun (top) and Supay (bottom). The particles are colour-coded according to the temperature of the gas (left) and the velocity dispersion of stars (middle) and DM (right). The inset on the bottom of each panel shows the cumulative probability distributions of finding a particle at a distance *larger* than a given radius. Note that the cold gas with high (positive) radial velocities at very small radii is due to the numerical treatment of supernova feedback in the central galaxy.

In order to provide a few representative examples, in Fig. 2.2 we consider two rather massive substructures extracted from our simulations. Although they both have $z_{\text{ac}} \approx 2$, one of them survives till the present time while the other is completely disrupted (meaning that AHF cannot identify it any longer at late times against the background of the host halo). For this reason, we dub them S-Sat and D-Sat, respectively. S-Sat (shown on the left-hand side) is part of Supay while D-Sat (displayed on the right-hand side) is hosted by Amun, although this is not important as similar examples are present in every re-simulated halo. In the top panels, we show the distance of the satellites from the centres of the corresponding hosts as a function of time. The curves start well before the satellites first ‘enter’ their host and follow their radial trajectories until the present time. S-Sat follows a very eccentric orbit and only experiences two pericentric passages while D-Sat describes a series of fast-decaying orbits and completes many pericentric passages. At accretion, S-Sat and D-sat are characterized by similar relative velocities with respect to the host although the impact parameter of D-Sat is three times larger than for S-Sat.

In the central panels, we show the time evolution of the satellite mass in DM (green), gas (blue) and stars (red). At accretion, S-Sat has a (total) mass of $M_{\text{ac}} = 2.9 \times 10^8 h^{-1} M_{\odot}$ which progressively reduces to $M_{\text{sh}}(z = 0) = 8.7 \times 10^7 h^{-1} M_{\odot}$. D-Sat is initially much more massive, with $M_{\text{ac}} = 1.3 \times 10^9 h^{-1} M_{\odot}$. The stellar and DM masses remain fairly constant until late times when the satellites reach the densest regions of the host haloes and are tidally stripped. On the other hand, the gas component follows a very different evolutionary path. Even before z_{ac} , gas is stripped off the (yet to be) satellites. This is due to the combined action of two mechanisms: heating caused by the ultraviolet background radiation and interactions with an increasing environment density. After the reionization of the intergalactic medium is completed at $z \sim 6$, photo-heating affects low-density gas which is not self-shielded. As a consequence, the gas reservoir of haloes that are below the atomic cooling mass limit [199, 200] can be completely depleted [201, 202]. Simultaneously, as the low-mass haloes approach their final more-massive host, they find themselves in denser and denser environments of the cosmic web and can loose their gas via ram pressure stripping [203]. Both S-Sat and D-Sat are massive enough to retain a substantial amount of gas at z_{ac} . However, after they accreted on to their hosts, they are completely deprived of gas within the first few pericentric passages [see also 204].

A more detailed view of the fate of a substructure is provided by the radial phase space plots in the bottom panels of Fig. 2.2. Here we show the location of the simulation particles (DM, gas and stars) that form S-Sat and D-Sat from $z = 3.5$ to $z = 0$ with time steps of 500 Myr. The particles are colour-coded based on redshift and, to facilitate understanding, symbols of the corresponding colours are also shown in the top panel. The effect of tidal interactions is clearly noticeable in the bottom-left panel. Particles start being stripped off S-Sat during its first pericentric passage. The debris form tidal tails that eventually fall on to the host along a very extended stream. At $z = 0$, the original subhalo has been split in three different components: the material stripped during the first orbit lying inside the halo; the recently-disrupted material, as distant as $400 h^{-1}$ kpc, being slowly accreted by the main halo, and the surviving subhalo orbiting around the host. Each pericentric passage ends up generating a dynamically coherent structure in which positions and velocities are strongly correlated. One of these ‘tidal caustics’ [e.g. 205] is clearly noticeable in the radial phase-space diagram for S-Sat as a symmetric distribution of loose particles with a uniform colour and a characteristic bell shape. Note that tidal caustics have a finite width and density (contrary to genuine caustics that are generated by a perfectly cold distribution of particles with the same energy). The build up of tidal streams and caustics is particularly evident in the bottom-right panel. Due to its larger mass, D-Sat experiences stronger dynamical friction than S-Sat. Consequently, it orbits much closer to the centre of the host and with a shorter period, resulting in a rapid disruption. A series of tidal caustics corresponding to the multiple orbits of the satellite are in fact noticeable in the phase-space diagram of the loose material at $z = 0$.

Fig. 2.2 shows that, after its first pericentric passage, S-Sat reaches a distance of $\sim 415 h^{-1}$ kpc from its

host halo while some of the stripped debris stretch out to more than $500 h^{-1}$ kpc of separation. Note that S-Sat travels across its first apocentre at $z_{\text{ap}} = 0.8$ when the radius of Supay is $R_h = 160 h^{-1}$ kpc (dashed line in the bottom-left panel). This phenomenon is quite common [see also 206, and Fig. 8 in Paper I] and makes it interesting to compare the apocentric distance of the satellite with the splashback radius of the host halo which is generally assumed to mark its physical outer boundary. We first estimate R_{spl} by locating the minimum of the logarithmic derivative of the spherically averaged mass density profile [195]. Our result at z_{ap} is shown with a dot-dashed line. Since numerical derivatives are noisy, we also make use of the SHELLFISH code [207] to reconstruct the full three-dimensional shape of the splashback surface and derive R_{spl} as the radius of the sphere with the same enclosed volume. In all cases, this estimate differs by less than 4 per cent from the previous one. Finally, we obtain a third value for R_{spl} by using a fit to the median splashback radius of haloes with a given mass and accretion rate [averaged over time scales comparable with the halo crossing time, see equation (5) in 195] and providing the appropriate input for S-Sat. The resulting R_{spl} (dotted line) is always larger than our previous estimates but still substantially lower than the apocentric distance of S-Sat. Although we have presented in detail only one specific example, the same conclusions can be reached after studying the evolution of a very large number of satellites. We find that the first apocentric distance lies beyond the splashback radius for nearly 40 per cent of the satellites, regardless of the host halo. It is worth stressing that two distinct concepts have been mixed up under the name of splashback radius [194, 195]. In practical calculations, R_{spl} is defined as the location at which the halo mass-density profile presents a sudden steepening of its slope. On the other hand, based on spherical models of collisionless secondary infall, R_{spl} is interpreted as the position of the outermost density caustic and, by extension, as the radius at which newly accreted matter reaches its first apocentre. Our results indicate that, in realistic cases, these two concepts do not perfectly match and the practical definition of R_{spl} needs to be further refined in order to make them compatible. A step forward in this direction has been made by [208] who used N-body simulations to investigate the relation between R_{spl} and the first apocentric distances of DM particles that are not part of substructures. Our complementary study, instead, follows the orbits of satellite galaxies in haloes of lower mass. Further understanding is also required to optimise the strategy for the observational detection of the splashback radius in galaxy clusters using their member galaxies [209, 210].

2.3.2 Shed material

We now focus on the material that was originally locked in substructures and later became part of the host halo and its central galaxy (this study completes the analysis presented in paper II). For example, in Fig. 2.3, we consider the 100 most massive substructures identified at $z = 2$ in Amun (top) and Supay (bottom) and plot the radial phase space distribution of their original constituents (gas, stars and DM) at $z = 0$ (similar conclusions can be drawn selecting Abu and Siris, as well as halving or doubling the sample of substructures). Particles are colour-coded according to their temperature (for the gas) or velocity dispersion (for stars and DM) computed using the 64 nearest neighbours of the same species. The inset on the bottom of each panel shows the cumulative probability distribution $P(> r)$ of finding a particle of the given species at distances larger than r . The phase-space distribution of the gas extends to larger radii with respect to the bulk of the collisionless components. While stars and DM show clumps associated with surviving satellites, virtually all the gas has been stripped off of the substructures. Shock-heating and feedback mechanisms have ejected a good fraction of this gas outside the main halo from where it can rain back in once it has cooled down. However, the cooling time can be quite long depending on the local metallicity and density. It is worth stressing that only half of the gas that was part of substructures at $z = 2$ is still found within R_h at $z = 0$ (see also the discussion about recycled material in paper II). This effect might not be accurately captured by certain ‘semi-analytic’ models of galaxy formation that make

too simplistic assumptions concerning gas stripping from satellites and stellar feedback [see also 211].

Baryonic material that was at first part of substructures also migrates to the central galaxy and its disc. By approximating the latter as a cylinder with height and radius corresponding to three times the scale values derived in paper II, we determine the fraction f_{disc} of the original baryonic mass of a $z = 2$ substructure that is found in the galaxy at $z = 0$. This quantity increases with M_{sh} since massive subhaloes are more affected by dynamical friction and retain a larger gas reservoir until disruption. Although f_{disc} shows a lot of scatter, its mean value for each of the ZOMG haloes is rather small, ranging between 3 and 9 per cent (see Table 2.1). The halo assembly time does not seem to have an influence on $\langle f_{\text{disc}} \rangle$. However, this quantity is substantially larger for Amun and Supay that host central galaxies with a prominent disc component (see paper II). This is not only reflecting the larger disc size but is also a consequence of the deeper potential well that alters the orbits of the satellites [212]. Consistently, the (baryonic) mass fraction of the present-day disc that was inside substructures at $z = 2$ amounts to 32 and 8 per cent for Supay and Amun, respectively, while is smaller for Siris (3 per cent) and in particular for Abu (0.5 per cent). Note that only a few massive substructures with large f_{disc} determine the value for Supay.

2.4 Subhalo statistics

After having described the phenomenology and the main physical mechanisms of satellite evolution, we investigate the statistical properties of the surviving substructures. The goal of this section is twofold. First, we show that our simulations are in agreement with many observations and previous numerical studies. At the same time, however, we try to isolate possible distinctive features characterizing stalled and accreting haloes. Since observation of satellites are only possible in the local universe, we exclusively present results at $z = 0$ (unless explicitly stated otherwise).

2.4.1 Mass and radial distribution

In the bottom panel of Fig. 2.4 we show the distribution by mass of satellites in each of the ZOMG haloes (within R_{h} and at $z = 0$, commonly dubbed subhalo mass function, or sHMF) together with the slope of the corresponding best-fitting power law of the form

$$\frac{dN(M_{\text{sh}})}{dM_{\text{sh}}} \propto M_{\text{sh}}^{\alpha} \quad (2.1)$$

(note that, while we show the cumulative sHMF, we perform the fit using the differential distribution of M_{sh} in order to avoid highly correlated errors). In the fit, we weigh the binned counts according to their Poisson errors and, to limit incompleteness due to resolution effects, we only consider satellites containing at least 100 DM particles (this mass limit is indicated in Fig. 2.4 with a vertical shaded region). The best-fitting slopes for the different ZOMG haloes are compatible within the errorbars (the actual values are reported in Fig. 2.4). Overall, they are in good agreement with the value of $\alpha \simeq -1.9$ generally found in high-resolution N -body [160, 213–218] and hydrodynamical [169, 219, 220] simulations (dot-dashed line). This is also consistent with observational estimates based on strong [221, for the substructure in galaxy-sized haloes] and weak [222, for the Coma cluster] gravitational lensing.

In the top panel of Fig. 2.4, we show the probability distribution of the satellite masses at accretion for each ZOMG halo. This unevolved sHMF is usually averaged over all main haloes present at a given time and includes the satellites accreted at any previous time. Numerical studies found it can be well

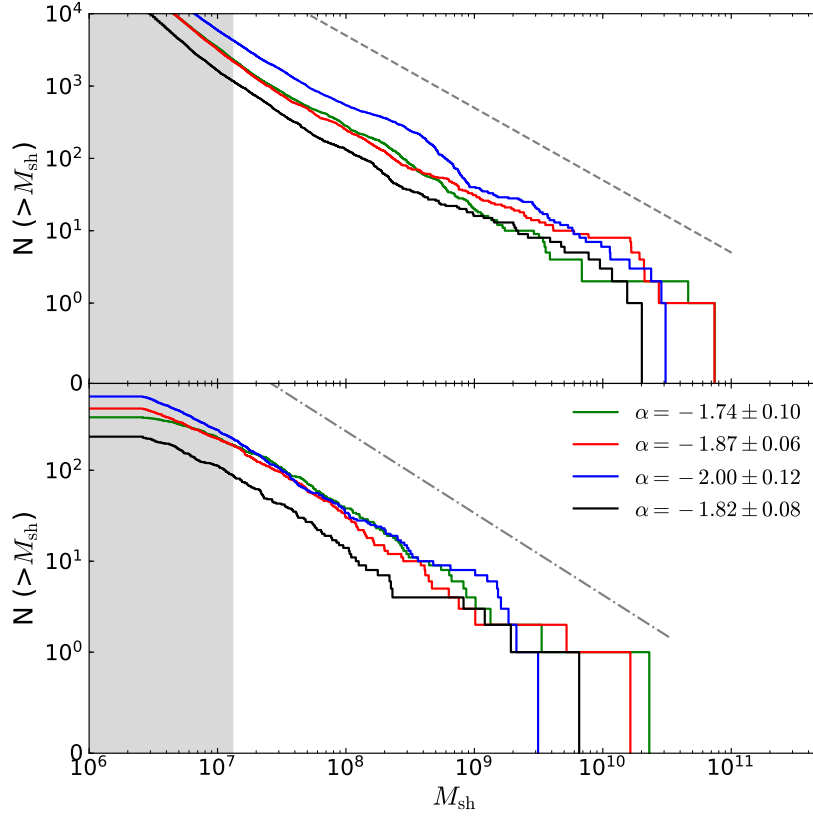


Figure 2.4: Uninvolved (top) and evolved (bottom) cumulative subhalo mass functions. The gray vertical shaded region corresponds to subhalo masses smaller than 100 DM particles. The dashed and dot-dashed lines are used as a reference and correspond to a power law with slope $\beta = -1$ and $\alpha + 1 = -0.9$, respectively. In the bottom panel the slope of the best-fitting power law for each host are reported.

approximated by a power-law

$$\frac{dN(> M_{ac})}{dM_{sh}} \propto M_{sh}^{\beta} \quad (2.2)$$

with slope $\beta = -1$ [215, 223, 224]. Such relation (dashed line) is in good agreement with our results for single haloes.

Within R_h , the spherically averaged mass density profiles of the ZOMG haloes are well described by the NFW function

$$\rho(r) = \frac{4\rho_s}{(r/r_s) [1 + (r/r_s)^2]} \quad (2.3)$$

where r_s and $\rho_s = \rho(r_s)$ denote a characteristic radius and density. This is shown by the dashed lines in Fig. 2.5 where we have appropriately rescaled the horizontal and vertical axes so that the different curves should coincide if the mass profiles exactly follow equation (2.3). The corresponding values of R_h are indicated by vertical segments (see also Table 2.1). We now compare the radial distribution of the satellites in accreting and stalled haloes at $z = 0$ (solid lines in Fig. 2.5). All the hosts show the same pattern: the satellite distribution traces the matter profile for $r \gtrsim 0.7 R_h$ but flattens out at smaller radii where substructures are more easily disrupted. Similar findings have been originally reported for

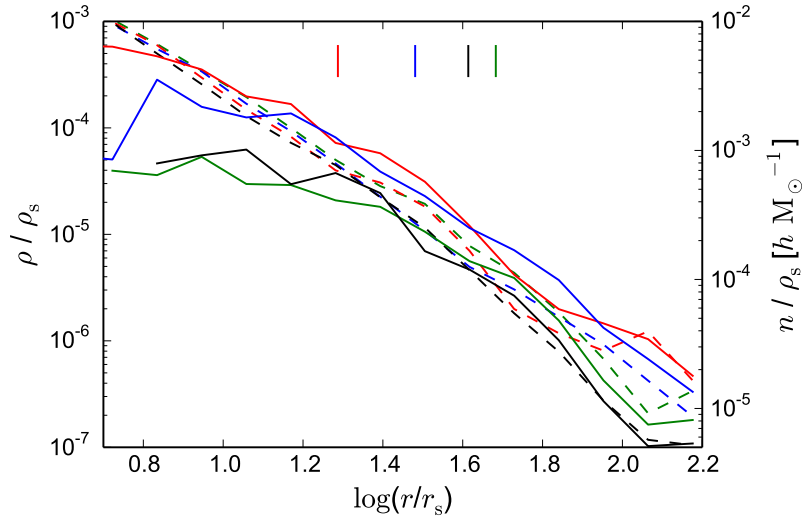


Figure 2.5: Radial distributions of substructures (solid) and matter (dashed) within and around the ZOMG haloes at $z = 0$. Note the different vertical scale for the two profiles, which are rescaled by the best-fitting value of ρ_s . Similarly, r , the distance from the host centre, is normalized by the scale radius r_s . Vertical segments indicates the radius of each halo.

cluster-sized haloes [216, 225] and, later, on galaxy scales based on dark-matter-only [e.g. 224] and hydrodynamical simulations [e.g. 170, 226, 227].

2.4.2 Gas and stellar content

We now delve into the analysis of the stellar and gas content of substructures. In Fig. 2.6, we plot the maximum circular velocity, V_{\max} , of a subhalo against its total baryonic mass, M_b . Observationally, these quantities are tightly correlated and the corresponding power-law relation is known as the baryonic Tully-Fisher (BTF) relation [67–69]. Since [228] showed that central and satellite galaxies follow consistent relations, we compare our data to their fit for both populations (solid gray line). The simulated substructures are in good agreement with the observed mean relation and no difference is noticeable between the different ZOMG haloes. It is worth noticing that the simulations overpredict the scatter in the BTF relation, especially at low V_{\max} . This is a long-known issue with the standard scenario of galaxy formation (e.g. 231 and 232, but see 233 and 234).

In Fig. 2.7 we show scatterplots of the 1D stellar velocity dispersion (top) and the stellar mass fraction (bottom) against the total mass of the substructures are shown. The four populations are well mixed and no segregation with z_c is found. In the common mass range, they match data from Milky Way (MW) dwarf spheroidal satellites [229, 230, black triangles].

Only a minority of the substructures have a stellar counterpart (see e.g. the eighth column of Table 2.1 and Fig. 2.1) which typically formed between redshift 5 and 6. Most satellites, in fact, are below the atomic cooling mass limit and are completely sterilized during the epoch of reionization. Nevertheless, a significant number of massive and concentrated subhaloes is able to retain some gas that, sooner or later, contributes to the gas reservoir of the host halo (see Fig. 2.3) and, possibly, of its central galaxy (paper II). Notably, a relevant portion of the satellites containing some gas at $z = 0$ have not just accreted on to their hosts (in some cases $z_{\text{ac}} \sim 1$). Overall, the fraction of substructures with gas in the ZOMG

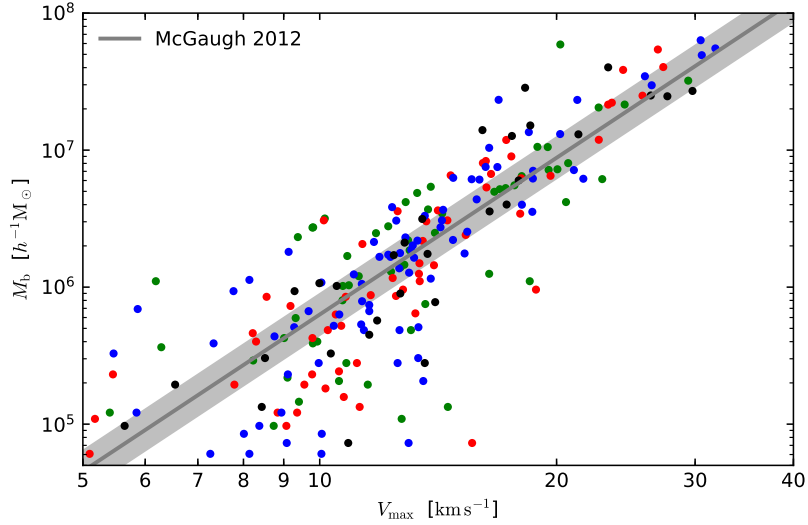


Figure 2.6: Baryonic Tully-Fisher relation for the ZOMG subhalo populations. The solid line and the shaded region denote the best-fitting power law and the maximum estimated scatter for the observational data, respectively [228].

project is consistent with previous hydrodynamical simulations of cluster-sized haloes [e.g. 167, 235]. Comparing with observations, we note that the gas content measured in Milky Way satellites² [237–240] is well below our mass resolution and thus compatible with our gas-naked substructures.

Finally, we assess the presence of star-forming satellites at $z = 0$, defined as substructures containing at least two stellar particles formed in the last 200 Myr. Interestingly, they are found only in accreting haloes (Amun contains two of them and Abu one). In particular, they are the most massive subhaloes at $z = 0$ ($M_{\text{sh}} \gtrsim 5 \times 10^9 h^{-1} M_{\odot}$) although their stellar mass is relatively low ($M_{*,\text{sh}} \approx 10^6 h^{-1} M_{\odot}$). They have already experienced one or two pericentric passages and their star-formation rates (SFR) lie in the range $4 \times 10^{-3} < \text{SFR} \lesssim 1.1 \times 10^{-2} M_{\odot} \text{yr}^{-1}$. Interestingly, a satellite with similar characteristics (in terms of mass and number of pericentric passages) is hosted by Supay and did not experience any star formation in the last 200 Myr. At late times, accreting haloes increase their mass at a faster rate than stalled haloes (paper I). Therefore, they are more likely to host substructures that are massive enough to sustain star formation up to $z = 0$. We provide further evidence supporting this conjecture in section 2.4.3.

Galactic conformity

The term ‘galactic conformity’ denotes the tendency of neighbouring galaxies to exhibit similar colours and SF properties. Originally, conformity was detected between galaxies in a single DM halo [241] although the signal might extend well beyond the virial radius of the host [242]. In particular, it has been shown that passive (star-forming) central galaxies tend to be surrounded by passive (star-forming) satellites. This trend becomes more and more prominent with decreasing mass of the host halo [e.g. 241, 243, 244]. In order to extend the theoretical predictions to lower halo masses, we check if the specific SFR (sSFR, i.e. the SFR per unit stellar mass) of our satellite galaxies reflects the value found

² An obvious exception is provided by the Magellanic Clouds. However, since similar configurations are rare in the Λ CDM cosmology [e.g. 236], it is not surprising that we do not find any in our relatively small simulation suite.

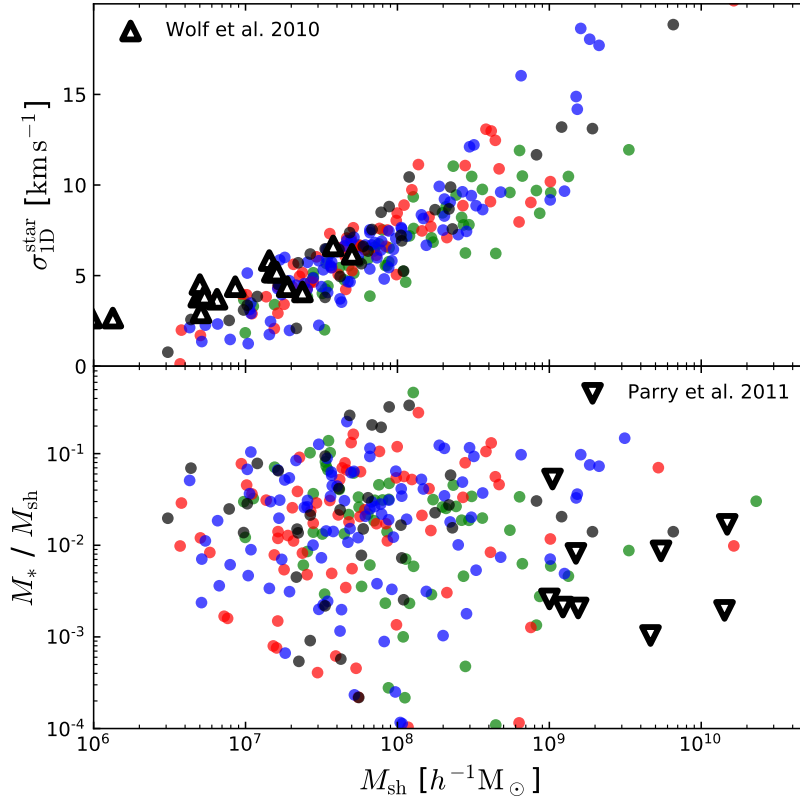


Figure 2.7: Top: 1D velocity dispersion for stellar particles ($\sigma_{\text{ID}}^{\text{star}}$, computed assuming isotropy) as a function of subhalo mass. The triangles represent data from [229] for Milky Way dwarf spheroidal satellites. Bottom: fraction of mass in stars as a function M_{sh} . Black triangles show data from Milky Way satellites [230].

for the primary galaxy in each ZOMG halo. We follow the strategy of [241] and classify our galaxies as ‘quenched’ or ‘star forming’ using a threshold value for the sSFR of 10^{-10} yr^{-1} . According to this criterion, all the central and satellite galaxies in our simulations are labelled as quenched at $z = 0$, although three of the primaries lie on the star-forming main sequence (see Fig. 17 in paper II). For the satellites, the classification is independent of the stellar mass, the time interval used to evaluate the SFR and the distance from the central galaxy. In fact, the bulk of the satellites do not experience any SF in the last few Gyr. We conclude that the small ZOMG sample shows perfect conformity.

2.4.3 Satellite mass fraction

We compute the fraction of M_{h} contributed by (resolved) subhaloes, i.e. $f_{\text{sh}} \equiv \sum_i M_{\text{sh},i} / M_{\text{h}}$. At $z = 0$, in accreting haloes this quantity is 1.6 times larger than in their stalled counterparts (see Table 2.1) and its evolution is shown in Fig. 2.8 as a function of the expansion factor. Vertical dashed lines mark a_c for each halo. This evolution typically shows many ‘spikes’ where f_{sh} sharply increases and then gradually falls off. These peaks correspond to mergers that bring massive satellites inside the main halo (indicated by arrows in the figure), sensibly increasing f_{sh} . Their subsequent drop reflects the mass eroded from the satellite that becomes part of the main halo. Fig. 2.8 shows that stalled haloes have almost no recent ($a < 0.5$) merger, while accreting haloes undergo many merger events in the same period. This difference

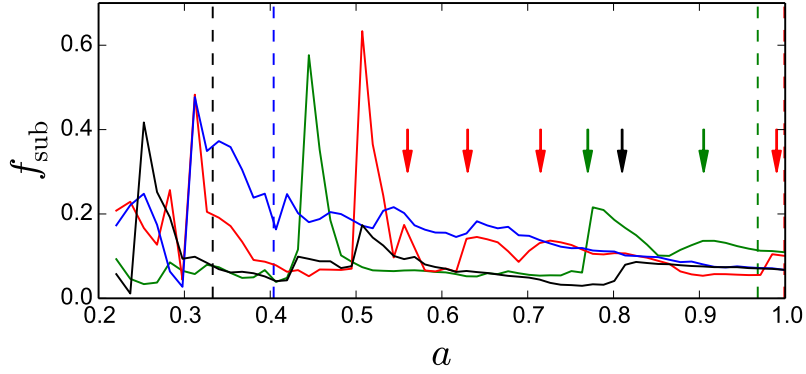


Figure 2.8: Fraction of the host mass contained in resolved substructures (f_{sh}) as a function of expansion factor a for the ZOMG haloes. Dotted lines denotes the a_c of the host. Arrows highlight when the sharp increase in f_{sh} can be attributed to a massive merger (shown only for $a > 0.5$).

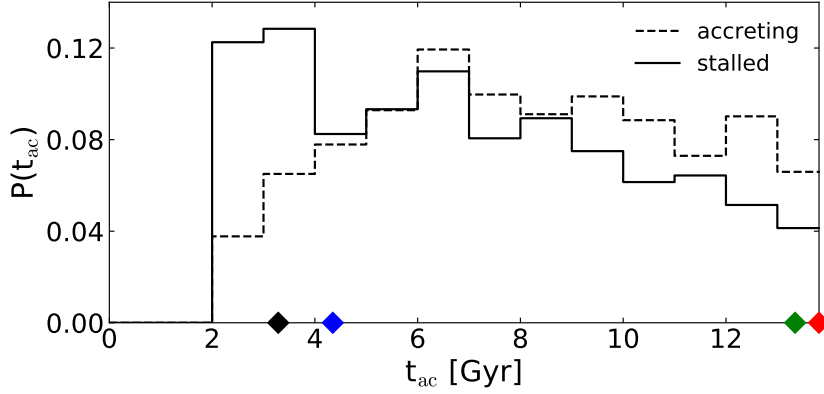


Figure 2.9: Distribution of accretion times of all the substructures with $M_{\text{sh}} \geq 100 m_{\text{DM}}$ that were ever identified within the host. Solid and dashed lines correspond to stalled and accreting haloes, respectively. Diamond symbols show the assembly time of the ZOMG haloes.

reflects their accretion properties, investigated in paper I and II.

The results illustrated above suggest that accreting and stalled haloes host similar subhalo populations at $z = 0$ and would be difficult to distinguish observationally. Possible exceptions are: i) the presence of star-forming satellites that only appear in accreting haloes, although in small numbers; ii) the different subhalo mass fractions. In the next section, we investigate the assembly history of the subhalo populations and correlate them with the large-scale environments in which accreting and stalled haloes reside.

2.5 Effects of halo assembly

In paper I we show that stalled haloes reside within prominent filaments of the cosmic web which distort the matter flow in their surroundings and impact their assembly history and internal dynamics. On the other hand, accreting haloes populate knots of the web and are fed by multiple streams running along

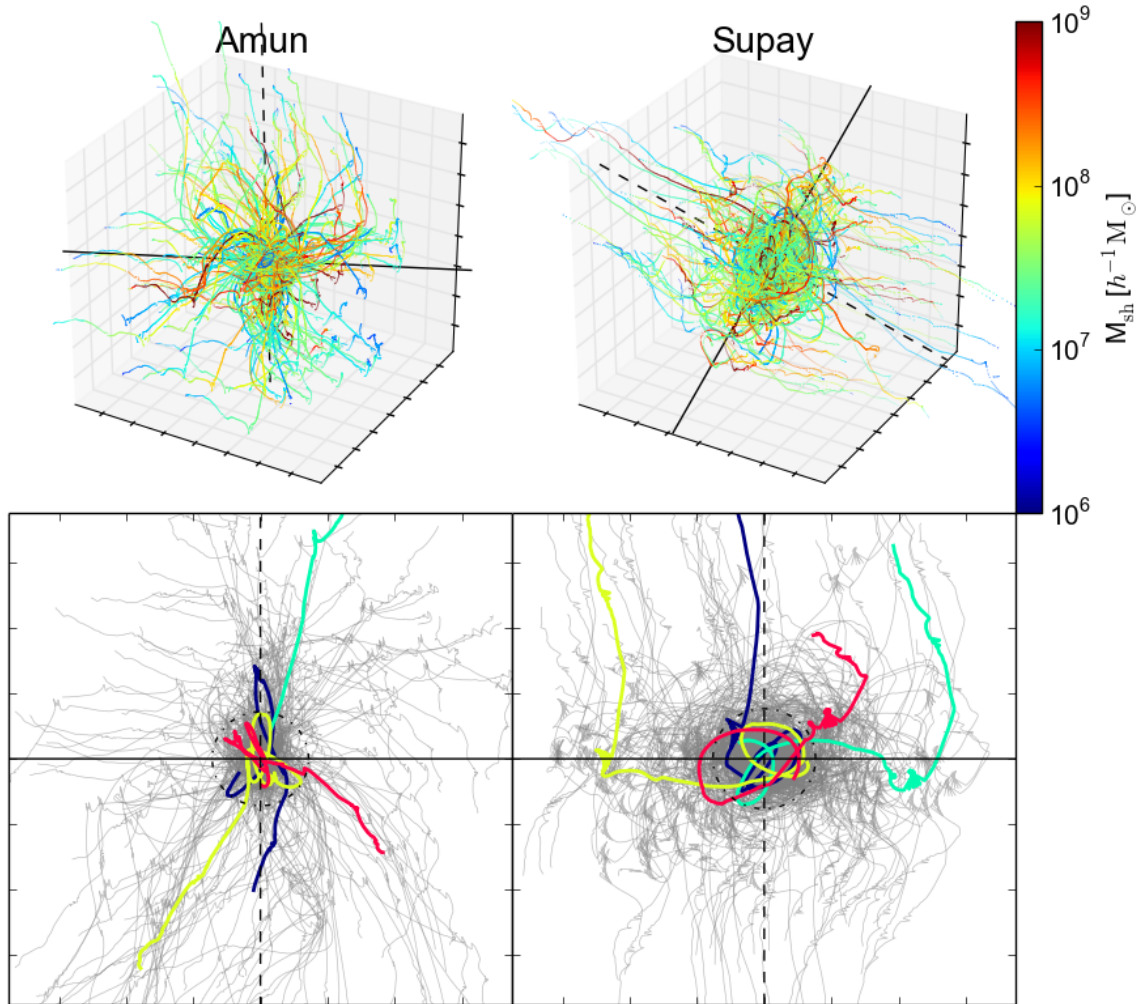


Figure 2.10: Top: Trajectories of all the substructures identified at $z = 0$ in two haloes of the ZOMG suite. The trajectories are in the host rest frame and colour-coded with respect to the subhalo mass. The black solid and dashed lines correspond to the directions of minimum (\hat{e}_3) and maximum (\hat{e}_1) compression, respectively (see Section 2.5.2 for details on how they are determined). For Supay, \hat{e}_1 corresponds to the direction of the filament it is embedded in. Each panel is $1.5 h^{-1} \text{Mpc}$ wide in each dimension. Bottom: The same as the top panels but projected on the plane defined by \hat{e}_1 and \hat{e}_3 . For visual clarity a random subsample of trajectories have been highlighted using different colours. The dot-dashed circle denotes R_h .

thinner filaments. It is then reasonable to expect that their different accretion patterns might impact the infall of satellite and their final configuration.

2.5.1 Accretion time

In Fig. 2.9 we show the distribution of accretion times (t_{ac}) for all surviving and disrupted substructures with $M_{\text{sh}} \geq 100 m_{\text{DM}}$. For comparison, we also mark on the x -axis the collapse time of the ZOMG haloes using diamond-shaped symbols. Stalled haloes (solid line) show an enhanced accretion of satellites at very early times ($t_{\text{ac}} \leq 4\text{Gyr}$) with respect to accreting hosts (dashed line) that present a more prominent tail at late epochs ($t_{\text{ac}} \geq 9\text{Gyr}$). The distribution of t_{ac} is thus consistent with the description of halo collapse discussed in paper I. Interestingly, however, the amount of satellites accreted at late times by accreting haloes is only marginally larger than in stalled hosts.

2.5.2 Accretion pattern

We now investigate if the accretion of satellites follows the same spatial pattern as the DM. The top panels of Fig. 2.10 show the trajectories (in the rest frame of the host) of all satellites identified at redshift $z = 0$ within Amun (left panels) and Supay (right panels) – no significant difference is noticeable in Abu and Siris. The colour-coding reflects M_{sh} as indicated in the bar on the right-hand side. The black solid and dashed lines highlight the directions of the minor ($\hat{\mathbf{e}}_3$) and major ($\hat{\mathbf{e}}_1$) axes of inertia for the Lagrangian patch out of which the halo forms (see paper I for further details). This region is maximally compressed along $\hat{\mathbf{e}}_1$ due to tides. For stalled haloes, $\hat{\mathbf{e}}_3$ instead coincides with the orientation of the filament they are embedded in. The bottom panels of Fig. 2.10 show the projection of the orbits on the plane defined by these two directions. For clarity, a few random trajectories are highlighted using coloured lines. The accretion pattern is different in the two classes of haloes. In stalled hosts, substructures first fall in to the filament along $\hat{\mathbf{e}}_1$ and then on to the main halo following curved trajectories. This secondary infall can only take place within a small region of the filament immediately surrounding the halo. Beyond this patch, velocities recede from the host along $\hat{\mathbf{e}}_3$. It is exactly this configuration that ultimately suppress matter infall and makes the halo stalled. We also note that the gravitational field of the filament bends the trajectories of the infalling satellites with respect to the radial orbits predicted by many idealized collapse models (paper I). On the other hand, accreting haloes have a more isotropic accretion pattern and their infalling substructures reach the host along approximately radial orbits. We conclude that the accretion of satellites and DM are regulated by the same dynamics which is manifestly different in accreting and stalled haloes. Since the distribution and the kinematics of substructures can be constrained with observations, this phenomenon provides us with a chance to distinguish accreting and stalled haloes in the local universe. With this perspective in mind, we explore a number of potential proxies for z_c .

2.5.3 Subhalo kinematic and anisotropy parameter

The velocity orientation of substructures at accretion reflects the different infall pattern of accreting and stalled haloes. The solid lines in Fig. 2.11 show the probability density function (PDF) of the normalized radial velocity component v_r/v at accretion for the ZOMG haloes classified based on their collapse time. In accreting haloes (red), the bulk of the satellites accrete on to their hosts along nearly radial orbits. Conversely, the tangential component is more prominent in stalled haloes (black) where the distribution of v_r/v is uniform. The Kolmogorov–Smirnov (KS) test rules out the null hypothesis that the two samples of subhalo velocities are extracted from the same population at a very high confidence level (the corresponding p -value is $p < 10^{-300}$).

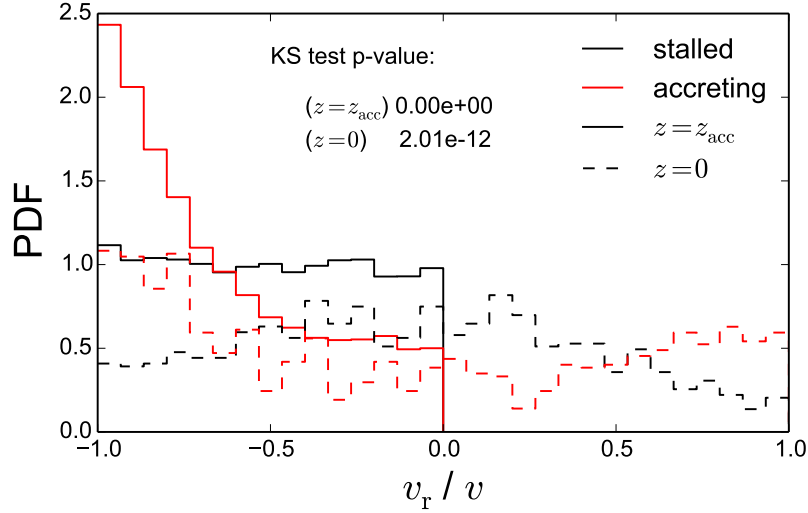


Figure 2.11: Probability density function (PDF) of the (normalized) radial velocity at the time of accretion (solid lines) and at $z = 0$ (dashed lines) for substructures hosted by stalled (black lines) and accreting (red lines) haloes. Distributions referring to the same time are compared using a Kolmogorov–Smirnov test and the resulting p -value is reported.

In order to understand if this difference persists with time (and is potentially observable), we analyse the distribution of the satellite velocities at $z = 0$ (dashed lines). The PDFs at $z = 0$ are much flatter than at accretion as a consequence of the orbit randomization that takes place within the hosts. Nevertheless, accreting haloes still present an excess of satellites on radial orbits (both infalling and outgoing) whilst the substructures of stalled hosts show a small preference for tangential motion ($v_r/v \approx 0$). Even in this case it is very unlikely that the samples are drawn from the same underlying population (the p -value of the KS test is 2×10^{-12}).

From an observational point of view, determining the state of motion of a population of satellites around a central galaxy is challenging as it requires proper motion measurements. So far this has been possible only for the closest substructures within the Milky Way halo but the *Gaia* mission and other future space-based facilities might help us extending the measurements to the outer Galaxy and Andromeda [e.g. 246, 247]. Using 10 satellites with proper motion measurements (the 11 classical satellites with the exception of Sextans), [245] conclude that Milky Way satellites show a prominent excess of tangential orbits which is quite unusual within the Λ CDM paradigm. Interestingly, in paper I, we point out that DM motion in the stalled haloes of the ZOMG suite presents enhanced tangential motions triggered by the gravitational effects of the filaments they are embedded in. In order to connect all these findings, we consider the anisotropy parameter of the satellites

$$\beta = 1 - \frac{\sum_i v_{\text{tan},i}^2}{2 \sum_i v_{\text{rad},i}^2} \quad (2.4)$$

where $v_{\text{tan},i}$ and $v_{\text{rad},i}$ are the tangential and radial components of the velocity of the i -th satellite with respect to the centre of the host halo and the sum runs over the substructures that fulfill a given selection criterion. The value of β provides a simple parameterization of the satellite dynamics: $\beta = 0$ corresponds

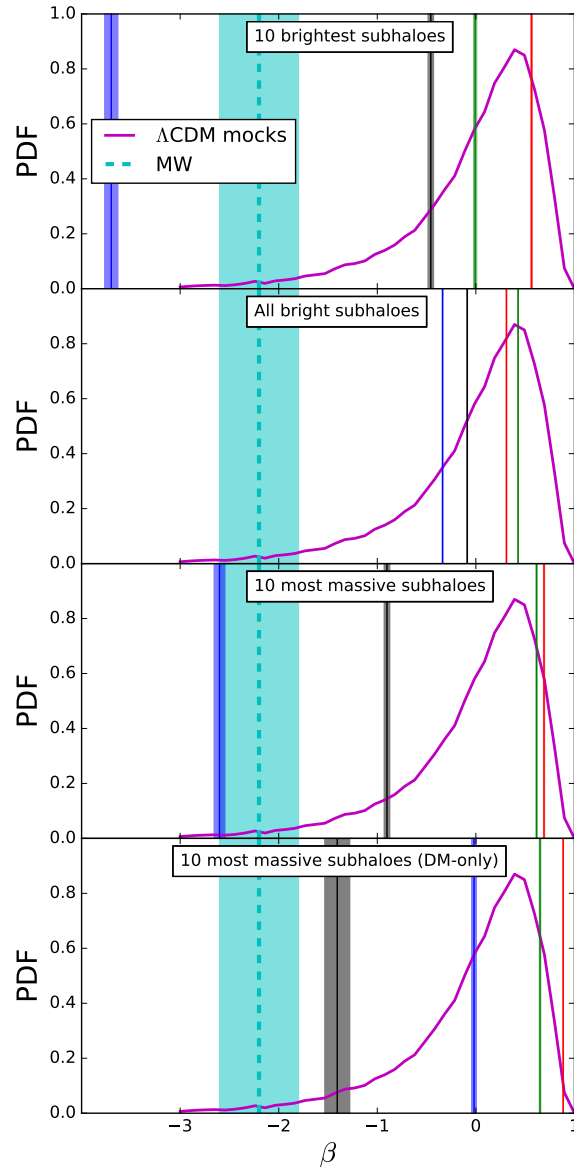


Figure 2.12: Anisotropy parameter β computed for our halo sample (solid vertical lines, the shaded region around indicates the bootstrap error). The dashed vertical cyan line (and its shading) shows the results for the MW classical satellites from [245], while the magenta profile shows the probability distribution function computed by the same authors using a semi-analytical model applied to MW-type DM-haloes. The four panels show different subsets of satellites used to compute the anisotropy parameter, namely (from top to bottom) the ten with largest stellar mass, all bright satellites with at least one stellar particle, the ten most massive in the hydrodynamical runs and in the DM-only ones.

to isotropic orbits while positive and negative values indicate the predominance of tangential and radial orbits, respectively. In Fig. 2.12, we compare the ZOMG simulations to the results presented in [245]. The wide vertical shaded band with a dashed line in the middle indicates the measurement and the uncertainty reported for the 10 MW classical satellites. The underlying curve shows the PDF of β expected in the Λ CDM scenario. This has been extracted from an N -body simulation whose haloes have been populated with galaxies using a semi-analytical model. To build the PDF, [245] first select MW-type haloes and then consider only the 10 satellites with the largest stellar mass for each halo. Note that only 2.9 per cent of the Λ CDM haloes are associated with a more extreme value of β than the MW. The values we obtain for the four ZOMG haloes are shown with vertical solid lines surrounded by a shaded band which indicates the corresponding jackknife errors. To explore the dependence of β on the satellite sample we repeat the measurements using four different selection criteria: the ten satellites with the largest stellar mass ('brightest', top), all the subhaloes containing at least one stellar particle ('all bright', upper centre), the ten most massive satellites in the hydrodynamic simulations ('most massive', lower centre) and in the DM-only runs (bottom). It is worth noticing that, in the hydrodynamic simulations and when we select the 10 most massive subhaloes (either based on the stellar or the total mass), Supay has a more extreme value of β than it is measured for the MW.

Although the precise values of β vary significantly with the sample, stalled (accreting) haloes invariably show negative (positive) values of β . This is a consequence of the large difference in the radial velocities at accretion time (see Fig. 2.11), which is preserved until $z = 0$. Additionally, substructures in accreting haloes tend to have larger t_{ac} than in stalled hosts (see Fig. 2.9, we check that this holds true for all the selection criteria employed) that are therefore more affected by orbit randomization.

The results presented in this section suggest a way forward to link observable properties of satellites to the assembly time of their host DM halo. They represent an evidence that satellite dynamics is strongly affected by the environment, which in turn determines the collapse time of the halo (paper I). Hence, if the proper motion of sufficiently numerous satellites can be measured (e.g. in the local universe), stalled and accreting DM haloes can in principle be distinguished. Additionally, in paper II we show that stalled haloes are found to host central galaxies with thicker stellar discs and older stellar populations with respect to accreting haloes. By considering a large sample of haloes, a dedicated numerical effort could then determine a precise relation between all these characteristics and t_c .

Based on our results, it is tempting to classify the MW halo as a stalled structure. In fact, the anisotropy parameter of its bright satellites is significantly negative. Consistently, the stellar disc of the Galaxy is found to be relatively thick and old [248, 249]. Something to bear in mind is that, contrary to naive expectations, plenty of gas can still accrete on to the central galaxy of a stalled halo and sustain regular star formation (see paper II).

The dependence of the anisotropy parameter on t_c might help shedding new light on another intriguing observational finding. Investigating the satellite kinematics in the Sloan Digital Sky Survey, [250] infer that the satellites of red galaxies tend to have a positive β . Taken at face value, this result might suggest that red central galaxies are preferentially hosted by accreting haloes. In the ZOMG simulations, no obvious correlation has been found between the central galaxy type and the halo accretion history (paper II). However, the ZOMG suite is too small to detect subtle statistical trends and substantially larger numerical samples are required to draw strong conclusions regarding the interpretation of the observational data.

2.5.4 Satellite configuration

The brightest substructures of the MW lie within a flattened region which is almost perpendicular to the Galactic disc [251, 252]. Proper motion measurements of the classical satellites suggest that most of

Table 2.2: The spatial flatness of a given set of substructures can be determined by computing the ratio between the lengths of their minor and major axes of inertia (c/a). Below we report the values of c/a obtained applying different selection criteria for the satellites. Namely, MM refers to the ten most massive satellites, MB to the ten brightest, AB to all the substructures with at least one stellar particle, and DM to the ten subhaloes with the largest M_{sh} in the DM-only run. We repeat each calculation three times, using different weighting schemes: uniform, $w = r^{-1}$ and $w = r^{-2}$, where r denotes the distance of a satellite from the centre of its host halo.

	$w = 1$	$w = r^{-1}$	$w = r^{-2}$	$w = 1$	$w = r^{-1}$	$w = r^{-2}$
	Abu			Supay		
MM	0.09	0.19	0.33	0.52	0.61	0.33
MB	0.17	0.26	0.32	0.14	0.18	0.20
AB	0.43	0.49	0.53	0.44	0.46	0.44
DM	0.12	0.20	0.33	0.12	0.19	0.22
	Amun			Siris		
MM	0.12	0.15	0.14	0.48	0.45	0.38
MB	0.06	0.10	0.17	0.44	0.52	0.40
AB	0.25	0.29	0.34	0.45	0.39	0.33
DM	0.14	0.18	0.20	0.30	0.37	0.41

them orbit within this ‘plane’ [253]. Likewise, nearly half of Andromeda’s satellites form a thin planar structure [254]. The existence of similar features has also been reported for M81 [255] and Centaurus A [256]. In addition, the dwarf galaxies within the NGC 3109 association form a filamentary structure which is well ordered in phase space [257]. Within the Λ CDM paradigm, a few mechanisms have been invoked to explain the presence of these dynamically coherent features. Among these, for instance, are the hypothesis that substructures accrete on to the host while they are part of clustered groups [258, 259] or that cosmic filaments imprint a preferential direction for the infall of satellites [178, 260]. It is difficult to conciliate this scenario with the observations in a quantitative way [e.g. 261]. As an alternative, it has been proposed that the planes of satellites in the MW and in Andromeda might originate from the tidal tail of a violent galaxy interaction that took place long ago in the Local Group [e.g. 262, and references therein]. Although a consensus has yet to be reached on this issue, it is anyway interesting to further explore the implications of the standard cosmological model for the spatial distribution of the satellites. For instance, the different accretion modes of stalled and accreting haloes could play a key role in shaping more or less flattened collections of substructures at $z = 0$. Therefore, we investigate the planarity of the satellite distributions in the ZOMG haloes.

Spatial distribution

We first focus on the satellite positions at $z = 0$ for the four subsamples we already used in Section 2.5.3 although a more general analysis will be presented in Section 2.5.4. We compute the tensor of inertia (ToI) of the substructures employing three different weighting schemes (uniform, r^{-1} and r^{-2} where r is the radial distance from the halo centre). We compute the eigenvalues of the ToI and denote by $a \geq b \geq c$ their square roots. The degree of planarity of the satellite distribution is quantified using the ratio c/a . Our results are presented in Table 2.2. Although the measurements sensibly depend on the sample and the weighting scheme, the brightest (or most massive) satellites in accreting haloes tend to lie within

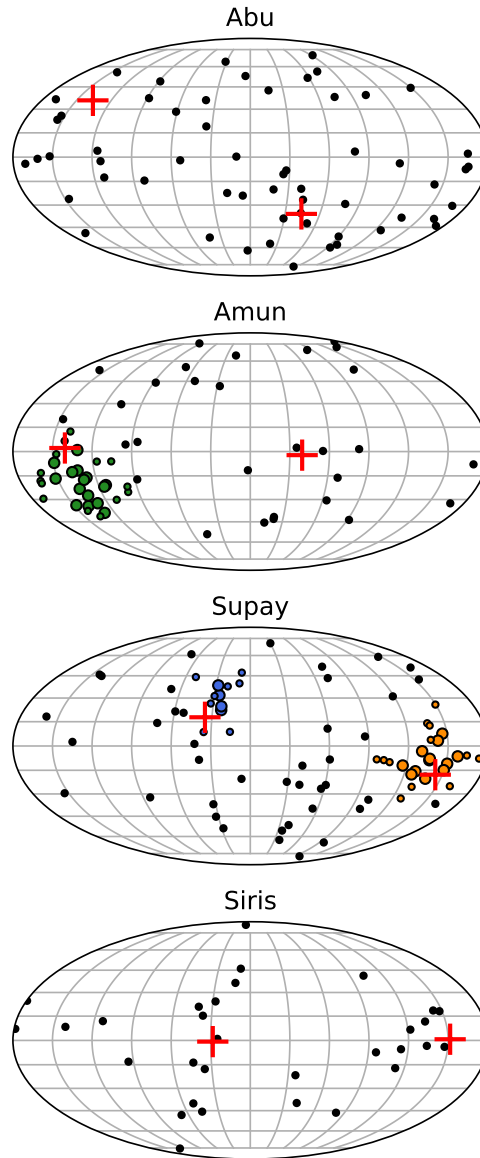


Figure 2.13: Mollweide maps showing the direction of the orbital angular momentum for our simulated satellite galaxies with $M_* > 10^5 h^{-1} M_\odot$. Each L -cluster identified by DBSCAN is highlighted with a different colour while black symbols denote unclustered satellites. The red crosses indicate the smallest principal axis of the ToI for the ‘all bright’ subsample evaluated with uniform weights.

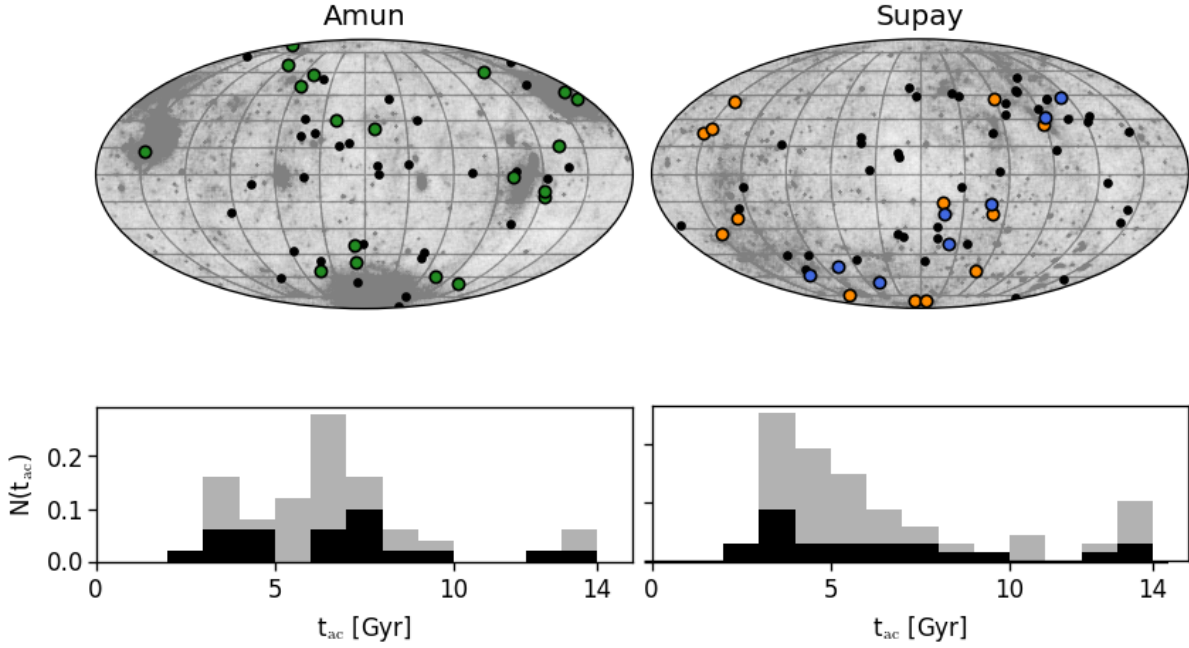


Figure 2.14: Top: Mollweide map of the angular position at accretion time of the satellites with $M_* > 10^5 h^{-1} M_\odot$ in Supay and Amun (circles, colour-coded as in Fig. 2.13). In the background, we show the matter distribution at R_h evaluated at $z = 0$ (darker regions correspond to higher surface densities). The few thin filaments that converge in Amun are easily seen whereas the filament embedding Supay is not noticeable because it is much thicker than R_h . Bottom: Probability distribution of t_{ac} for all satellites with $M_* > 10^5 h^{-1} M_\odot$ (gray) and for the satellites in the L -clusters (black). For Supay both L -clusters have been combined together.

flatter spatial configurations with respect to those in stalled hosts. However, given the variability of the results, it is difficult to draw solid conclusions based on our small sample. In many cases, the values of c/a extracted from the simulations are comparable with the estimates³ found for the MW which range between 0.18 [266] and 0.3 [180].

We now test whether the flattened satellite distributions in the ZOMG haloes are dynamically stable. If this is the case, the angular momenta of the satellites should be well aligned (or anti-aligned) with the normal, $\mathbf{\hat{n}}$, to the ‘plane’. We therefore compute the angle θ_i between the orbital angular momentum of a substructure and the smallest principal axis of the ToI (a proxy for $\mathbf{\hat{n}}$). In many cases, only a few of the satellites that have been used to identify $\mathbf{\hat{n}}$ actually have $|\cos(\theta_i)| \sim 1$. This suggests that the planar structures determined with the ToI are short lived and probably due to chance alignments. In some haloes, however, 60-70 per cent of the selected satellites have $|\cos(\theta_i)| > 0.75$ and can orbit in the flattened structures for longer times. This happens, for instance, for both the accreting haloes when we consider the most massive substructures (based on the KS test the difference with the stalled haloes is significant at 99 per cent confidence level) and for Abu and Supay when we select the brightest satellites. Interestingly, c/a is rather low in these cases.

³ [263, 264] find that estimates of c/a are not stable and argue against the existence of a plane of satellites in the MW. [265] strongly criticize this claim and emphasize the lack of a proper statistical analysis to reach it. Our work consists of a theoretical investigation on the impact of the assembly history on the substructure properties. Drawing conclusions about the MW satellites is outside the scope of this paper and, in any case, our simulation suite would be too small to conduct such an investigation.

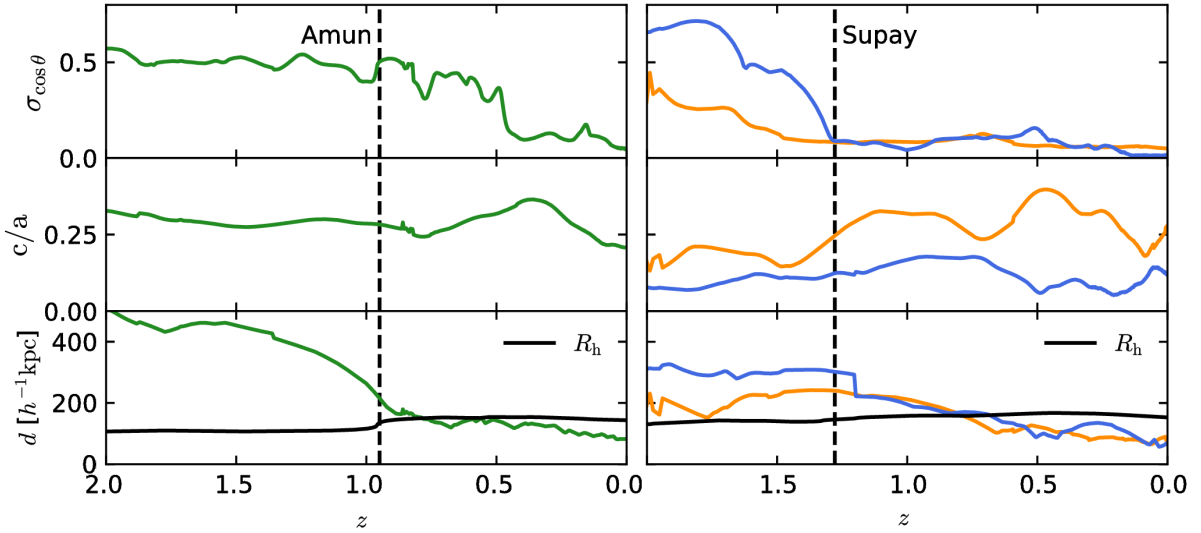


Figure 2.15: The degree of alignment of the orbital angular momenta ($\sigma_{\cos\theta}$, top), the level of planarity (c/a , centre) and the median distance from the host centre (d , bottom) are plotted as a function of time for the satellites that at $z = 0$ form the L -clusters in Supay and Amun. Each L -cluster is denoted by the colour used in Fig. 2.13. The vertical dashed lines indicate the redshift of the last major merger for the host haloes. For each snapshot we only consider substructures containing at least 20 DM particles.

Clustering of angular momenta

To generalize the results presented in the previous section, we now look for groups of substructures with aligned orbital angular momenta without pre-selecting the satellites based on their structural properties, as we did before to compare with previous work. We only require the stellar mass to be $M_* > 10^5 h^{-1} M_\odot$ to approximately match the observational limits. Coherently rotating groups are identified by applying a clustering algorithm to the directions of the orbital angular momenta. We use the method named Density-Based Spatial Clustering of Applications with Noise [DBSCAN, 267] and make sure that our analysis does not depend on its tunable parameters. The resulting L -clusters are shown in Fig. 2.13 (coloured filled circles) together with all the unclustered satellites (black circles). The angular momenta of the substructures in Abu and Siris are consistent with a random distribution. On the other hand, Amun shows a prominent L -cluster composed of 25 objects and Supay presents two of them containing 9 and 21 satellites. Interestingly, these two groups orbit in opposite directions in the plane perpendicular to the vector $\hat{\mathbf{n}}$ identified for the ‘all bright’ subsample (red crosses). It is worth noticing that Amun and Supay are the only two haloes in our simulations that host a grand-design spiral galaxy (paper II). Hence, it is not inconceivable that related physical mechanisms lie at the origin of both the galactic disc and the satellite plane. We have checked that the same L -clusters are also present in the DM-only simulations suggesting that baryons do not play a key role in their formation process. Despite the ZOMG sample is only formed of four central galaxies, two of them are surrounded by evident planes of satellites which are dynamically coherent. Our results thus suggest that the occurrence of these structures in the Λ CDM paradigm is not unlikely.

In the remainder of this section, we investigate the possible origin of the planar satellite configurations found in Amun and Supay. In the top panels of Fig. 2.14 we correlate the satellite position at accretion time (circles) with the matter distribution at R_h (gray background). Substructures are colour-coded as in

Fig. 2.13. Although satellites tend to accrete preferentially from high-density regions, the members of each L -cluster do not come from the same direction. Moreover, the distribution of their accretion times fairly traces that of all the luminous satellites (bottom panels in Fig. 2.14). These results do not support filamentary and/or clustered accretion as an explanation for the formation of the planar structures.

In order to understand if the L -clusters are short- or long-lived, we study their time evolution in Fig. 2.15. We characterize their degree of coherence using the rms value ($\sigma_{\cos\theta}$) of $\cos\theta$ defined with respect to their mean orbital angular momentum ($\sigma_{\cos\theta} = 3^{-1/2} \simeq 0.577$ for a random distribution while $\sigma_{\cos\theta} = 0$ for a perfectly coherent cluster). Simultaneously, we use c/a (employing uniform weights for the ToI) to describe their flatness and compute the median distance (d) of the cluster members from the host. For both galaxies, $\sigma_{\cos\theta}$ decreases significantly with time while c/a stays approximately constant. Note that the redshift range covered in Fig. 2.15 extends well beyond the accretion time of the substructures. As a reference, we indicate the time of the last major merger (determined from the mass accretion history) using a vertical dashed line. The L -clusters in Supay are already identifiable at early times (even for $t < t_c$, at least for the smaller one) when most of the substructures are still beyond R_h . This is also noticeable in Fig. 2.14 where the angular positions at accretion time of most cluster members lie within a very flattened region. Based on timing arguments, the formation of the L -clusters in Supay appears to be connected with the final stages of assembly of the host halo. On the other hand, the dynamically coherent group in Amun rapidly forms at much later times ($z \sim 0.4$), when more than 50 per cent of its members are already within the host halo. This might possibly reflect the delayed evolution of accreting haloes with respect to stalled ones.

2.6 Conclusions

We have exploited the high mass and temporal resolution of the ZOMG simulation suite (paper I, paper II) to study the substructure evolution of four haloes with masses of a few $\times 10^{11} h^{-1} M_\odot$ at $z = 0$. Abundance matching shows that haloes of this size have most efficiently converted baryons into stars and host L_* galaxies at the present time. We have characterized the assembly history of the haloes in terms of their collapse redshift, z_c , defined as the epoch at which the physical volume enclosing the halo material first becomes stable. Galaxy-sized DM haloes identified at $z = 0$ show a broad distribution of z_c (see Fig. 2 in paper I). In paper I, we have shown that z_c correlates with the cosmic environment surrounding the halo: stalled haloes are embedded within prominent filaments of the cosmic web that inhibit further infall of matter while accreting haloes are located at the knots of the web and are fed by a number of thinner filamentary structures. In order to study which properties of the haloes (and of the galaxies within them) depend on z_c , we have selected targets for zoom hydrodynamic simulations by sampling the tails of this distribution. We thus ended up considering two ‘accreting’ haloes ($z_c \lesssim 0$) named Abu and Amun and two ‘stalled’ haloes ($z_c \gtrsim 1$) dubbed Siris and Supay.

Our analysis reveals that many properties of the substructures are insensitive to the assembly history of the host halo. We list these features below.

1. At $z = 0$, more than 80 per cent of the surviving substructures do not contain stars (consistently with the effect of reionization) and more than 99 per cent are stripped off of their entire gas content (in agreement with observations of dwarf spheroidal satellites of the Milky Way).
2. Based on our feedback scheme, roughly half of the gas brought in the main halo by satellites is subsequently ejected and remains outside R_h until $z = 0$.
3. The fraction of baryonic mass in the satellites (identified at $z = 2$) that ends up in the disc of the central galaxy at $z = 0$ correlates with the disc size and M_{sh} . This reflects both the strength of the

gravitational field generated by the disc [212] and the increased ability to retain a gas reservoir that can be then deposited in the central galaxy by the most massive substructures.

4. The first apocentre of nearly 40 per cent of the satellites is located beyond the ‘splashback radius’ of the host halo identified as a sudden steepening of the mass density profile. This indicates that further work is needed to connect R_{spl} with the orbits of recently accreted material.
5. The evolved (i.e. at $z = 0$) and unevolved (i.e. at accretion time) mass functions, the radial distribution, the spread of the stellar mass fraction and of the velocity dispersion of the substructures are insensitive to the collapse time of the halo.
6. Based on their sSFR at $z = 0$, all the central and satellite galaxies are classified as ‘quenched’ according to the criterion of [241]. The ZOMG sample therefore shows perfect conformity between the SF properties of primary and satellite galaxies and confirms the trend previously found for larger halo masses.
7. Two of our resimulated haloes (Amun and Supay) contain large clusters of satellites with aligned orbital angular momenta that form a flattened structure in space. The very same features are present in the zoom N -body simulations of the haloes thus suggesting that baryonic physics does not play a major role in their formation. Contrary to other studies, we found that these clusters do not collect satellites that fell in along a specific direction or as a coherent group. Intriguingly, Amun and Supay are the only haloes in our sample that host a grand-design spiral galaxy at their centre thus suggesting a possible connection between the physics of disc formation and the assembly of planar configurations of satellites.

On the other hand, additional properties of the substructures clearly depend on the assembly history of the host halo. Most of them are related to the spatial and temporal pattern of satellite accretions that directly reflect the different cosmic environments hosting accreting and stalled haloes. They can be summarized as follows.

8. The fraction of halo mass locked in substructures at $z = 0$ is substantially larger in accreting haloes. Concurrently, stalled (accreting) haloes accrete a larger fraction of satellites at early (late) times.
9. The epoch at which the planar structures of satellites are formed (see item (vi) above) seems to be connected with the assembly time of the host haloes.
10. Substructures fall in towards accreting haloes following nearly radial trajectories. On the contrary, satellites initially orbit the filament that embeds the stalled haloes before falling on to their hosts. For this reason, they have a large tangential velocity component at accretion time.
11. Although maximal at infall, the different balance between the radial and tangential components of the satellite velocities in accreting and stalled haloes is clearly noticeable also at later times. For instance, the velocity anisotropy parameter of the satellites at $z = 0$ is positive for accreting haloes and negative for stalled haloes. This finding parallels the result found in paper I for the DM particles and provides a tool to determine the formation time of a halo based on the kinematic properties of its satellite galaxies. [245] have recently measured a strong tangential excess for the classical MW satellites corresponding to an anisotropy parameter of $\beta = -2.2 \pm 0.4$. It is thus tempting to tentatively categorize the MW halo as stalled. Further support to this conjecture comes from the thickness and age of the stellar disc (paper II).

Future work will aim to extend the approach presented in this work to a larger sample of haloes covering a wider range of halo masses and collapse times.

The radial acceleration relation of Λ CDM satellite galaxies¹

3.1 Introduction

The standard Λ CDM model of cosmology relies on the theory of general relativity and assumes that the energy budget of the universe is dominated by cold dark matter and a cosmological constant. The cosmic microwave background, gravitational lensing, and galactic dynamics provide abundant evidence for mass discrepancies which are usually interpreted as manifestations of particle dark matter (DM). However, its basic constituents have so far eluded direct detection. Furthermore, tight empirical relations are observed between the luminous and dark components of galaxies [52, 269–271]. These remarkable and intriguing correlations might appear ‘unnatural’ in the Λ CDM model. For this reason, some authors elevated them to fundamental laws of Nature and developed alternative scenarios without DM. In the theory of Modified Newtonian Dynamics (MOND) [63], for instance, the observed acceleration a is given by $a \mu(a/a_0) = a_N$, where a_N is the Newtonian acceleration, a_0 is a new fundamental constant of Nature, and μ is an interpolation function such that $\mu \rightarrow 1$ for $x \gg 1$ and $\mu \rightarrow x$ when $x \ll 1$. In the non-relativistic case, the MOND equation can be achieved by changing either the Newton’s second law (modified inertia, [65]) or the Poisson’s equation (modified gravity, [272]).

The debate was recently revived when [273] and [53] concluded that the (centripetal) radial acceleration (g_{bar}) generated by the visible baryonic matter in galaxies and the actual (centripetal) radial acceleration derived from kinematic measurements (g_{tot}) strongly correlate over the range $10^{-12} < g_{\text{bar}} < 10^{-8} \text{ m s}^{-2}$. In terms of the characteristic acceleration $g_{\ddagger} = [1.20 \pm 0.02 (\text{rnd}) \pm 0.24 (\text{sys})] \times 10^{-10} \text{ m s}^{-2}$, the spatially-resolved data for 240 galaxies of different sizes and morphological types scatter around the mean radial acceleration relation (RAR)

$$g_{\text{tot}} = \frac{g_{\text{bar}}}{1 - e^{-\sqrt{g_{\text{bar}}/g_{\ddagger}}}}, \quad (3.1)$$

i.e. $g_{\text{tot}} \simeq g_{\text{bar}}$ for $g_{\text{bar}} \gg g_{\ddagger}$ while $g_{\text{tot}} \simeq \sqrt{g_{\text{bar}}g_{\ddagger}} \gg g_{\text{bar}}$ for $g_{\text{bar}} \ll g_{\ddagger}$. Eq. (3.1) is inspired by the interpolation function of MOND and the existence of the RAR could be invoked as direct evidence for this alternative theory of gravity (basically, the empirical parameter g_{\ddagger} embodies a_0). However, numerical

¹This chapter has been published in [268]. The notation has been adapted to match the rest of this Thesis.

simulations of galaxy formation in the Λ CDM framework reproduce the overall shape of the observed correlation [54–57] (see, however, [60] for an exception). Here, the RAR emerges from the dissipative collapse of baryons within DM halos and is less influenced by the feedback of stars and active galactic nuclei. For disc galaxies forming at the centre of their host halos (central galaxies), the RAR reflects: i) the narrow range of the host virial masses; ii) the self-similar acceleration profiles of CDM haloes; iii) the tight correlation between baryonic mass, galaxy size and halo mass [54, 58]. However, simulated RARs tend to overpredict the value of g_{\ddagger} regardless of the adopted subgrid feedback model (except possibly [56]). Furthermore, the scatter around the RAR for late-type galaxies ($\lesssim 0.13$ dex) is dominated by observational uncertainties, which is difficult to reconcile with simulations which show an intrinsic spread of comparable magnitude [59].

This Letter focuses on the low g_{bar} regime which has the potential to distinguish between the two competing scenarios described above. By analyzing a set of satellites of Andromeda and the Milky Way, [53] found that dwarf spheroidal galaxies (dSphs) do not follow Eq. (3.1) if g_{\ddagger} is chosen to fit the data for more massive objects. Instead of dropping as $g_{\text{tot}} \propto \sqrt{g_{\text{bar}}}$, the total acceleration stays approximately constant, $g_{\text{tot}} \simeq 10^{-11} \text{ m s}^{-2}$, for $g_{\text{bar}} \lesssim 9 \times 10^{-12} \text{ m s}^{-2}$. It is currently impossible to draw conclusions based on this finding. In fact, the expected signal in Λ CDM has only been computed for central galaxies that probe larger accelerations than faint dSphs. Moreover, as extensively discussed in [53], it is still unclear whether the observed flattening of the RAR is physical or due to observational artifacts. The inferred masses (or, equivalently, the values of g_{tot}) for faint dSphs are based on velocity-dispersion measurements [229] and are plagued by considerably larger uncertainties than measurements of rotation curves for late-type galaxies. Since dSphs have low velocity dispersions and their estimates are often based on a handful of observable stars, current results might be severely affected by unresolved binary systems [274]. Both this effect and out-of-equilibrium dynamics tend to inflate the measured velocity dispersions [275].

This situation provides us with a unique opportunity to predict the expected behavior of the RAR for satellite galaxies in the Λ CDM scenario.

3.2 Numerical simulations

We use the ZOMG hydrodynamical simulations that have been comprehensively described in [98, 156, 157]. These runs follow the process of galaxy formation zooming in on a set of DM haloes with masses $M_h \approx 3 \times 10^{11} h^{-1} M_{\odot}$, where h denotes the present-day value of the Hubble parameter in units of $100 \text{ km s}^{-1} \text{ Mpc}^{-1}$. The background cosmology and the linear power spectrum of density perturbations match the best-fit *Planck*+WP+highL+BAO model in [126]. The mass resolution is $m_* = m_{\text{gas}}/2 = m_{\text{DM}}/10.8 = 1.21 \times 10^4 h^{-1} M_{\odot}$ for stars, gas and DM, respectively. The simulations employ a supernova-feedback model and the resulting central galaxies closely match the stellar mass-halo mass and stellar mass-star formation rate relations observed at redshift $z = 0$ [156]. Similarly, the satellite galaxies are consistent with the observed baryonic Tully-Fisher relation, subhalo mass function, stellar fraction and stellar velocity dispersion [157].

3.3 Method

DM haloes and their substructures are identified using the `AMIGA HALO FINDER` code [190, 191]. We associate a ‘main central galaxy’ (MCG) with each of the resimulated central DM halos by simply considering a spherical region extending for 10 per cent of the halo radius. All substructures with a stellar component that lie within the splashback radius of the main halo (identified with the abrupt steepening of

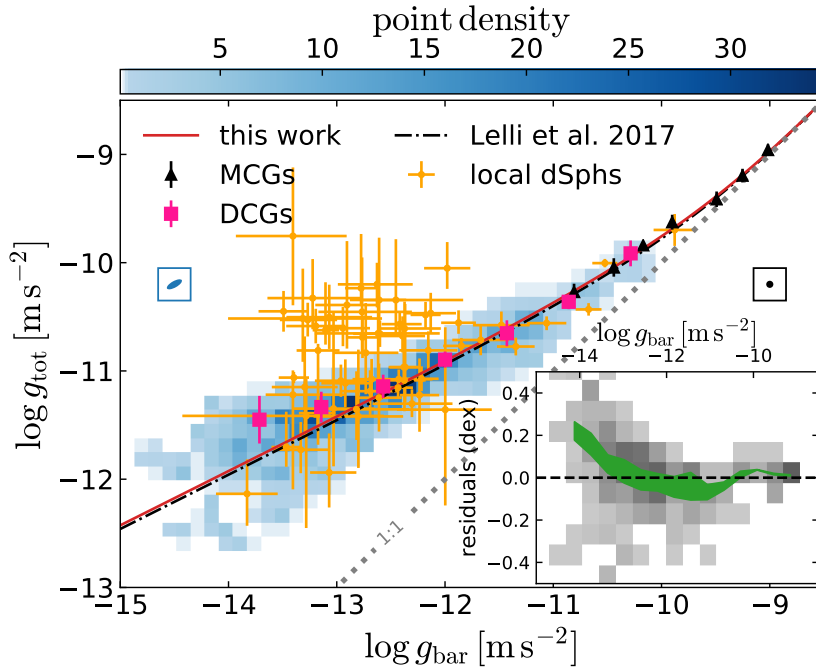


Figure 3.1: Distribution of observed and simulated galaxies in the $\log g_{\text{bar}} - \log g_{\text{tot}}$ plane. Triangles and squares indicate the median g_{tot} in bins of g_{bar} for the simulated MCGs and DCGs, respectively (errorbars enclose the central 68 per cent of the data). The solid and dot-dashed curves are the best-fit RARs inferred from the MCGs and the observations. The large crosses represent the measurements for local dSph satellites presented in [53]. The colored map displays the number density of the simulated MSGs. Each object corresponds to a bivariate Gaussian distribution reflecting the statistical errors. The framed ellipses show the typical 68 per cent bootstrap region for objects with $g_{\text{bar}} < 10^{-13} \text{ m s}^{-2}$ (left) and $g_{\text{bar}} > 10^{-10.5} \text{ m s}^{-2}$ (right). The inset shows the density of the residuals between the MSGs and the best-fit RAR for the MCGs. The solid band is centred on the mean residual at fixed g_{bar} and has width equal to the mean measurement error for g_{tot} .

the spherically averaged mass-density profile as in [193]) are labelled as ‘main satellite galaxies’ (MSGs). Finally, we consider the dwarf central galaxies (DCGs) associated with less massive DM clumps lying between one and three splashback radii from the main halos. The centripetal accelerations are evaluated as $g_x = G M_x(< r)/r^2$, where G is the gravitational constant and $M_x(< r)$ denotes the galaxy mass (total or baryonic) contained within the radius r . For MCGs, we compute the acceleration radial profiles and their correlated bootstrap errors (consistent with Poisson fluctuations) at 7 different positions extending from 1 per cent to 10 per cent of the halo radius equally spaced in log scale. We find that the resulting g_{tot} is consistent with measurements based on the gas rotational velocity, as done in observational studies. For MSGs and DCGs, accelerations are only computed at the stellar half-mass radius $R_{1/2}$ (i.e. the radius within which half of the stellar particles are located) to mimic the half-light radius used for observational data. We only consider galaxies containing more than 10 (gravitationally bound) stellar particles within $R_{1/2}$. The covariance matrix for g_{bar} and g_{tot} is estimated with the bootstrap method by resampling stellar particles within the individual objects. We find that errors on $\log g_{\text{bar}}$ and $\log g_{\text{tot}}$ approximately follow a bivariate Gaussian distribution. We fit Eq. (3.1) to our simulated data. Using Bayesian statistics, we jointly constrain g_{r} and σ_{int} , the intrinsic scatter around the RAR at fixed g_{bar} (i.e. the rms value of the residuals of $\log g_{\text{tot}}$). For each measured pair $(\log g_{\text{bar}}, \log g_{\text{tot}})$, we consider a Gaussian (partial) likelihood function and we marginalize it over the unknown true value of the baryonic acceleration (which

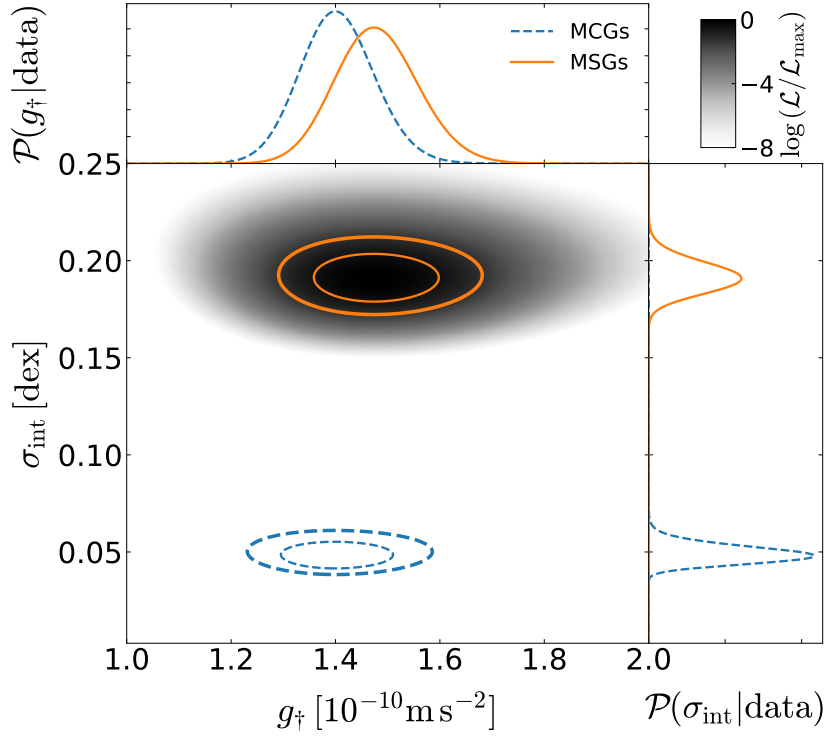


Figure 3.2: The central image shows the likelihood of the fitting parameters g_{\dagger} and σ_{int} given the simulated MSGs. The solid curves indicate the contour levels enclosing 68 per cent and 95 per cent of the posterior probability. Fitting the simulated MCGs, instead, produces the dashed contours. The top and right panels show the marginalized posterior distributions for g_{\dagger} and σ_{int} , respectively.

does not coincide with g_{bar} due to measurement errors). We write the variance of $\log g_{\text{tot}}$ at fixed g_{bar} as the sum in quadrature of the measurement error and σ_{int} . Eventually, we build posterior distributions for the model parameters by uniformly sampling the parameter space and assuming flat priors on g_{\dagger} and σ_{int} .

3.4 The RAR at redshift zero

Fig. 3.1 compares real and simulated galaxies in the $\log g_{\text{bar}} - \log g_{\text{tot}}$ plane at $z = 0$. Our MCGs and DCGs follow a tight RAR which is in excellent agreement with observations. For $g_{\text{bar}} < 10^{-12} \text{ m s}^{-2}$, DCGs depart from Eq. (3.1) and tend to have higher g_{tot} (see also [56, 57]). The dSph satellite galaxies analyzed in Ref. [53] sprinkle around $g_{\text{tot}} \simeq 10^{-11} \text{ m s}^{-2}$ independently of g_{bar} . Conversely, the simulated MSGs form a well defined sequence to a great extent aligned with the observed RAR (but with a larger scatter) and do not show any transition to a constant g_{tot} for the least massive satellites. For $g_{\text{bar}} < 10^{-13} \text{ m s}^{-2}$, their mean g_{tot} at fixed g_{bar} lies slightly above the observed RAR of the central galaxies (in fact $g_{\text{tot}} \propto g_{\text{bar}}^{0.4}$ in this regime) but slightly below that of DCGs. The observed dSph seem to be composed of two subsets: a sizeable fraction of them behave as the simulated satellites while the remainder align at $g_{\text{tot}} \simeq 3 \times 10^{-11} \text{ m s}^{-2}$. A quantitative analysis is presented in Fig. 3.2 where we compare the best-fit RARs for our MCGs and MSGs. The posterior probability densities of the model parameters show that centrals and satellites follow a RAR characterized by the same g_{\dagger} but with very different values for the intrinsic scatter. In fact, for the MCGs, we find $g_{\dagger} = (1.40 \pm 0.07) \times 10^{-10} \text{ m s}^{-2}$ and $\sigma_{\text{int}} = 0.048 \pm 0.005 \text{ dex}$

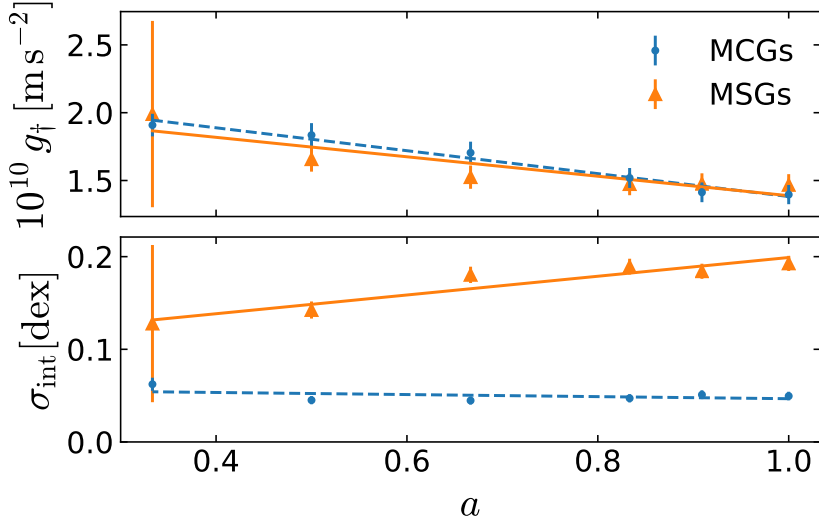


Figure 3.3: Evolution of g_+ (top) and σ_{int} (bottom) as a function of the expansion factor of the universe for MCGs (dots) and MSGs (triangles). The lines show the best-fit linear relations.

while, for the satellites, $g_+ = (1.48 \pm 0.08) \times 10^{-10} \text{ m s}^{-2}$ and $\sigma_{\text{int}} = 0.192 \pm 0.008 \text{ dex}$. The characteristic acceleration we measure is larger than, but compatible with, the observed value for MCGs which is plagued with a relatively large systematic error. We note that the model-fitting method influences the result. For instance, adopting the (frequentist) orthogonal-distance regression algorithm to fit only the characteristic acceleration (as in [53, 273]) yields $g_+ = (1.19 \pm 0.02) \times 10^{-10} \text{ m s}^{-2}$ for MCGs, in very good agreement with the observational results. Following [53], we define a ‘high-quality’ sample of satellites that contain a large number of stellar particles, have small ellipticities and are barely affected by the tidal field of the host galaxy. This does not significantly change the best-fit intervals for g_+ and σ_{int} .

3.5 Independency of the RAR on the satellite properties

Given the large scatter characterizing the RAR for MSGs, we investigate whether sub-classes of satellites with different physical properties follow distinct RARs at $z = 0$. We first sort the satellites based on some physical property. Then we separately fit Eq. (3.1) to the subsets containing the upper and lower 20 per cent of the sorted data. Specifically, we examine the following variables: (a) the tidal acceleration at $R_{1/2}$ due to the gravitational field of the host galaxy, $g_{\text{tides}} = 2 G M_{\text{host}} R_{1/2} / D_{\text{host}}^3$, as defined in [53]; (b) The distance of the satellite from the main galaxy; (c) The triaxiality parameter of the stellar distribution; (d) The minor-to-major and medium-to-major axis ratios; (e) The cosine of the angle between the satellite velocity and the radial direction with respect to the central host; (f) The stellar concentration defined as the ratio between the radius enclosing 80 per cent of the stellar mass and that enclosing 20 per cent of it; (g) The accretion time of the satellite on to its host; (h) The mass loss experienced between accretion time and redshift zero. The only significant discrepancy we find is between the credibility intervals of σ_{int} for the subsamples of case (h): the scatter is three times larger for satellites that experienced a large mass loss.

3.6 Time evolution of the RAR

Finally, we study the RAR at $z > 0$. At all epochs, we identify a well defined relation for both MCGs and MSGs which we fit using Eq. (3.1). Our findings, summarized in Fig. 3.3, show that both g_{\ddagger} and σ_{int} evolve little with time. To good approximation, the best-fit parameters for the RAR scale linearly with the scale factor a of the universe. In the range $0.33 \leq a \leq 1$, $g_{\ddagger} \simeq (-0.84 a + 2.23) \times 10^{-10} \text{ m s}^{-2}$ for MCGs and $g_{\ddagger} \simeq (-0.72 a + 2.11) \times 10^{-10} \text{ m s}^{-2}$ for MSGs (the uncertainty on the parameters is ~ 10 per cent). On the other hand, the intrinsic scatter around the RAR stays approximately constant for MCGs, $\sigma_{\text{int}} \simeq -0.01 a + 0.06 \text{ dex}$, and grows as $\sigma_{\text{int}} \simeq 0.1 a + 0.1 \text{ dex}$ for the satellites.

The evolution of the RAR for central galaxies is promoted by stellar feedback which drives important outflows at high redshift [56].

In order to characterize the time evolution of the satellites, in the top panel of Fig. 3.4, we partition them based on their g_{bar} at the present time and

plot the median trajectory of each subset in the $g_{\text{bar}}-g_{\text{tot}}$ plane as a function of redshift (indicated by the color). The trend is to move from the top right to the bottom left nearly parallel to the RAR. The other panels of Fig. 3.4 reveal the reason for this tendency. Essentially, while $R_{1/2}$ and the DM mass within it tend to grow with time, the stellar mass of the satellites decreases. This is the net result of tidal stripping that makes satellites more DM dominated with time. Since the DM and the stars in a satellite follow distinct spatial distributions at the accretion time, they react differently to tidal forces. The (physical) extension of the stellar distribution increases during the evolution [276, 277] while the DM density profile becomes more concentrated [278, 279]. Of course, individual objects follow complex trajectories in the $g_{\text{bar}}-g_{\text{tot}}$ plane which produce some scatter around the median trend (see also [280]).

3.7 Conclusions

The RAR is an empirical law describing a tight relation between the radial acceleration generated by the visible matter in galaxies and the actual acceleration derived from kinematic measurements. For bright central galaxies, the correlation is such that both g_{bar} and g_{tot} decrease in the outer regions. This result could hint towards a scenario in which there is no DM and the law of gravity needs to be modified along the lines of MOND. Galaxy-formation models within the Λ CDM scenario are able to reproduce the observed relation, although with too large a scatter. Ref. [53] provides evidence that nearby dSph satellite galaxies depart from the RAR and show a constant g_{tot} for $g_{\text{bar}} \lesssim 10^{-12} \text{ m s}^{-2}$. However, the authors caution that unresolved binary stars and out-of-equilibrium dynamics could bias the measurements of g_{tot} high in these low-mass structures. It is yet unclear what are the implications for the theory of gravity. The missing pieces of the puzzle are (a) more precise measurements and (b) accurate theoretical predictions for the behaviour of satellite galaxies in Λ CDM. This work supplies the latter by making use of a suite of zoom hydrodynamical simulations. Our main results are: (i) At $z = 0$, the simulated satellites scatter around a well defined sequence in the $g_{\text{bar}}-g_{\text{tot}}$ plane which is approximately aligned with the observed RAR for central galaxies and does not show any transition to a constant g_{tot} at low accelerations. (ii) For the least massive objects, the satellite sequence is shallower than the RAR for the central galaxies. In fact, g_{tot} scales as $g_{\text{bar}}^{0.4}$. This flattening is even more prominent for dwarf galaxies that are not satellites. (iii) The scatter around the satellite sequence is approximately four times larger than for the central galaxies. (iv) Although the deviations from the main sequence do not correlate with many physical properties of the satellites, the intrinsic scatter around the RAR is three times larger for objects that were stripped off more mass. (v) The RAR for central galaxies shows a mild evolution with redshift. The characteristic acceleration decreases with time, meaning that galaxies are relatively more baryon depleted at high

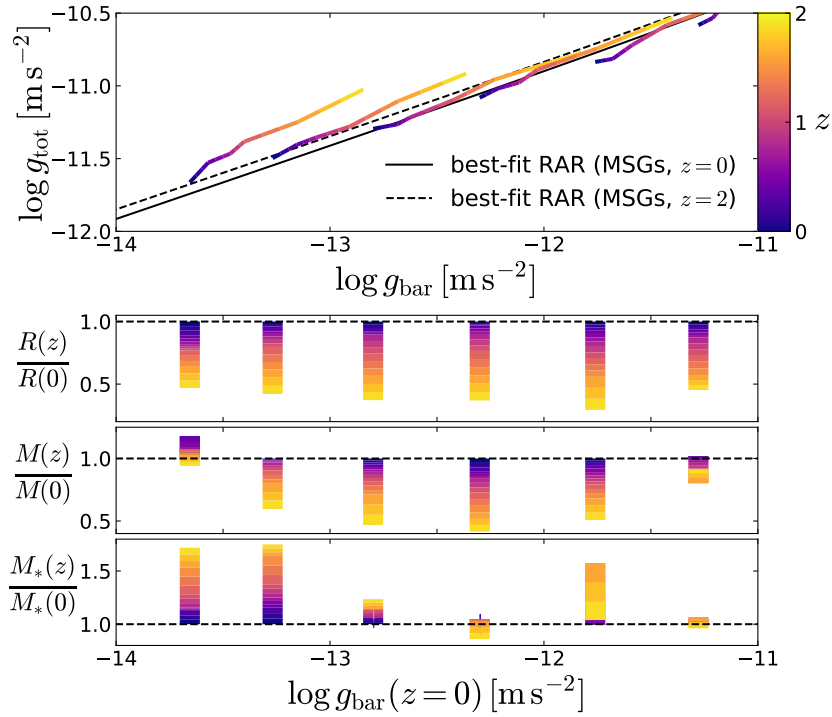


Figure 3.4: Top: Characteristic evolutionary tracks of MSGs obtained by partitioning the objects based on their value of g_{bar} at $z = 0$ and plotting the median values of g_{bar} and g_{tot} in each bin at some earlier epoch indicated by the color scale. Bottom: Evolution of $R_{1/2}$ and of the enclosed total and stellar masses for the same bins. Note that each satellite is tracked from the moment it accretes on to its host halo to $z = 0$. Therefore the number of objects in each bin decreases with increasing z .

redshifts with respect to the present epoch. The scatter around the relation z stays constant with time. (vi) Individual satellites tend to evolve along the $g_{\text{bar}}-g_{\text{tot}}$ sequence. This trend is driven by tidal stripping combined with an internal readjustment of the structures. Typically, the stellar profile broadens out and $R_{1/2}$ increases with time while the DM distribution gets more concentrated. (vii) Since satellites follow the RAR of the central galaxies before accreting on to their hosts and evolve along the main sequence afterwards, their g_{bar} shows the same time evolution as for the central galaxies. Given the wide variety of the evolutionary paths, the scatter around the relation between the accelerations for the satellites increases with time and with decreasing g_{bar} . (viii) In our simulations, residuals from the RAR for the satellites do not correlate with g_{tides} . Conversely, in the MOND framework, satellites in a strong external gravitational field show different internal accelerations than if they were isolated. Detecting the absence or presence of the correlations from observations would therefore provide a powerful test of the theory of gravity.

The effect of quasars on cosmic reionization¹

4.1 Introduction

Over the last decades, a standard picture has emerged for the epoch of cosmic reionization (EoR, see e.g. 282, 283 for a review). In this scenario, ultraviolet (UV) radiation produced by star formation in faint galaxies is responsible for the ionization of hydrogen and for the first ionization of helium in the intergalactic medium (IGM) at redshift $6 \lesssim z \lesssim 10$. Later on, at $2 \lesssim z \lesssim 4$, harder radiation from quasars (QSOs) causes the second ionization of the diffuse helium.

This standard picture is supported by observations and theoretical considerations. The rapid evolution in the transmission of the Lyman- α ($\text{Ly}\alpha$) forest at $z \lesssim 6$ [108, 127, 284], and the drop in the number density of $\text{Ly}\alpha$ emitters and $\text{Ly}\alpha$ -bright galaxies at $6 < z < 7$ (285, 286, 287, 288, 119; but see 289) set constraints on the timing of hydrogen reionization which are also supported by the latest data on the Thomson optical depth of the cosmic microwave background [CMB, 17, 290]. Similarly, the HeII $\text{Ly}\alpha$ forest encodes information about ‘helium reionization’, a conventional name used to indicate the transition from HeII to HeIII. Although only a handful of ‘clean’ sightlines (with little foreground absorption down to the HeII $\text{Ly}\alpha$ resonance wavelength) are available, they consistently show a rapid increase in the transmitted flux between $2.7 \lesssim z \lesssim 3$ [105, 107, 291–293]. Further constraints can be obtained from the evolution of the IGM temperature at mean density, inferred from the HI $\text{Ly}\alpha$ absorption features. Observational data are available only at $z \lesssim 5$ and show a large scatter, partially reflecting the different data analysis techniques used to retrieve this information. Nevertheless, the peak at $z \approx 3$ is usually interpreted as a signature of the completion of helium reionization.

Still, many details of the EoR are loosely constrained and there is space for substantial modifications to accommodate recent observations that challenge the standard description. The spectrum of the quasar ULAS J0148+0600 [108] contains a particularly long ($\sim 110 h^{-1}$ Mpc) Gunn-Peterson trough at redshift $z = 5.98$, which appears at odds with a completed hydrogen reionization [e.g. 294]. More recently, [295] observed a very extended dark gap covering the range $6.12 < z < 7.04$ and corresponding to a comoving length of $240 h^{-1}$ Mpc with a mean HI fraction $> 10^{-4}$. Additionally, current models of reionization have difficulties to explain the IGM inhomogeneity indicated by the broad probability distribution of the HI optical depth observed at $5 \lesssim z \lesssim 6$ (108, 109, 296, but see 297). Several studies have addressed this problem and indicated possible solutions. It has emerged that opacity fluctuations can be enhanced either

¹This chapter has been submitted for publication to *Monthly Notices of the Royal Astronomical Society*, while a preprint is available at [281]. The notation has been adapted to match the rest of this Thesis.

in the presence of local temperature variations [298] or by considering that the mean free path (λ_{mfp}) of ionizing photons depends on the local photoionization rate [299, 300]. Another possibility is to consider a scenario in which the QSO contribution to the reionization photon budget is boosted at high redshift [294]. This is the direction we explore in this paper.

The rationale for our investigation lies in an ongoing discussion in the literature regarding the abundance of faint active galactic nuclei at high redshift and their role during the EoR. By applying a novel selection criterion within a deep field with extensive multiwavelength coverage, [301] have detected an unexpectedly large number of faint (i.e. with an absolute magnitude $M_{\text{AB}} \sim -20$ at 1450 \AA) QSO candidates at $z > 4$ [but see 302, 303]. If confirmed, this result would suggest that QSOs provide an important contribution to the photon budget during the entire EoR and, possibly, even dominate it. Inspired by these findings, [304, MH2015 hereafter] have built an analytical model for the EoR in which all ionizing photons are generated by QSOs. Interestingly, the results of the model satisfy the observational constraints on the evolution of the HII fraction and on the Thomson optical depth of CMB photons. Following [301] and MH2015, a number of authors have revisited the question of the importance of non-stellar sources during hydrogen reionization [e.g. 294, 305–311]. However, these analytic or semi-numerical studies do not include a detailed treatment of radiation transfer which is necessary to make more accurate predictions (especially for the temperature of the IGM) and produce realistic synthetic observations to be compared with actual data. Moreover, the investigations based on semi-numerical methods only consider rather small computational volumes and thus suffer from sample variance. In this work, we improve upon existing results by performing detailed hydrodynamical simulations of a scenario in which cosmic reionization is driven only by quasars. We use a suite of large simulation boxes post-processed with a radiative-transfer (RT) code in order to track the detailed evolution of the IGM. We then produce realistic synthetic observations and use them to (i) test the plausibility of the QSO-only reionization model, (ii) uncover peculiarities of the QSO contribution to the EoR, and (iii) provide predictions for a number of observables that should be able to discriminate between the standard reionization scenario and a QSO-dominated one. Such information is extremely valuable in order to disentangle the role of different types of sources and shed light on the properties of the high-redshift IGM.

The paper is organized as follows. In Section 4.2, we describe our numerical techniques and the specifics of the runs. The simulation outputs are presented in Section 4.3 and analysed in Section 4.4 where we discuss several mock observations that we compare with actual data and previous theoretical work. Finally, we summarise our findings and draw conclusions in Section 4.5.

4.2 Numerical Methods

In this Section, we describe the setup of our numerical simulations, together with the modelling of the radiation sources and their calibration against recent observations. The techniques we use here are based on [312, hereafter CCP2013] and [106, CCP2014], to which we refer for further details.

4.2.1 Hydrodynamical simulations

We consider a flat Λ CDM cosmological model and use the results of the *Planck* satellite to fix the parameters that determine its background evolution and the power spectrum of the Gaussian linear perturbations [20]. For the present-day values of the matter density, the baryon density and the Hubble parameter we thus use $\Omega_{\text{m}} = 0.306$, $\Omega_{\text{b}} = 0.0483$ and $H_0 = 67.9 \text{ km s}^{-1} \text{ Mpc}^{-1}$, respectively. Moreover, the normalization of the linear power spectrum and the primordial spectral index are $\sigma_8 = 0.815$ and

$n = 0.958$.

We run four hydrodynamical simulations using the adaptive mesh refinement (AMR) code `RAMSES` [140] and employing a cubic box of comoving side $L_{\text{box}} = 100 h^{-1} \text{ Mpc}$ with periodic boundary conditions. The dark matter (DM) is sampled using 256^3 particles (corresponding to a particle mass $m_{\text{DM}} = 4.3 \times 10^9 h^{-1} M_{\odot}$) while the hydrodynamical equations are solved on a base grid of 256^3 elements with up to 7 levels of refinement. This way, the simulations reach a maximum nominal resolution of approximately $3 h^{-1} \text{ kpc}$ and resolve the Jeans length of the gas with several computational mesh cells. The refinement strategy is quasi-Lagrangian, namely a cell is split whenever the enclosed mass exceeds the critical threshold of $8 m_{\text{DM}}$. The initial conditions are produced using the `GRAFIC` package [313]. The gas is assumed to follow an ideal equation of state with adiabatic index $\gamma = 5/3$ and has a primordial composition (i.e. the helium mass fraction is $Y = 0.24$). We do not track star formation and neglect stellar feedback since the scales of interest for the analysis of the EoR are much larger than those affected by such phenomena (see also CCP2013, CCP2014). Note that our simulations do not include a background of UV radiation. The reason is twofold. First, we do not consider ionizing photons emitted by stars. Second, the ionizing radiation produced by QSOs is treated in post-processing as described in Section 4.2.2.

DM haloes are identified using the `HOP` finder [314] in its default configuration. We only consider haloes containing more than 70 DM particles (corresponding to halo masses $M_{\text{h}} > 3 \times 10^{11} h^{-1} M_{\odot}$) whose abundance agrees well with popular fitting functions [e.g. 315].

4.2.2 Radiative transfer

Modelling the timing and the properties of the EoR requires an accurate treatment of RT. This consists of two parts: describing the properties of the sources of UV radiation and propagating the ionizing photons through the IGM.

Ionizing sources

The spatial distribution of the ionizing sources within the cosmic web influences the development of cosmic reionization. Having the possibility to model this effect in a realistic way represents one of the main advantages of numerical simulations with respect to analytical models that describe radiation as a uniform background. In order to assign a position to each source of radiation, we assume that QSOs reside at the centre of DM haloes (neglecting multiple occupancies) and that their luminosity scales (statistically) with the mass of the host haloes [e.g. 106, 312, 316–318]. Several observations support this hypothesis [e.g. 319–323] although some exceptions have been found [324–326]. In practice, we consider each DM halo as a potential host of a QSO and sample the associated magnitude at 1450 \AA (M_{AB}) from a Gaussian distribution with mean

$$M_{\text{AB}} = -\frac{10}{3} \log \left(\frac{M_{\text{h}}}{h^{-1} M_{\odot}} \right) + \varepsilon \quad (4.1)$$

and standard deviation σ_{AB} . We determine the free parameters ε and σ_{AB} by fitting the shape of the quasar luminosity function (QLF) measured by [301] at redshift $4.0 < z < 4.5$. Using 1000 realisations of the QSO assignment, we obtain $\varepsilon = 19$ and $\sigma_{\text{AB}} = 1.25$ (with some freedom within a degeneracy region in parameter space). This implies that the resolved haloes in our simulations host QSOs in the range $-25.76 \leq M_{\text{AB}} \leq -18.67$. Our ionizing sources thus sample the faint end of the QLF which generates the majority of the ionising photons (only 11.6 per cent of the total should be emitted by the unresolved

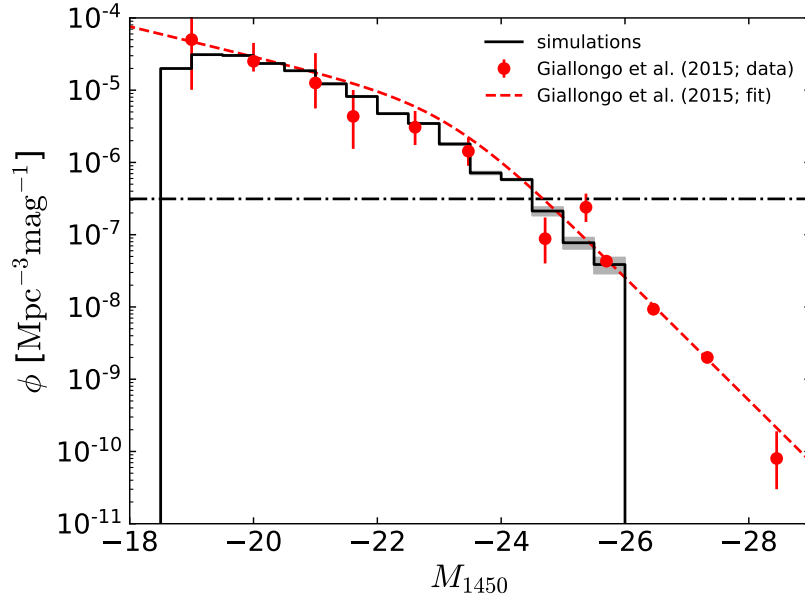


Figure 4.1: The QLF, ϕ , constructed from our simulations (solid histogram) is compared with the observational results by [301, points with errorbars] and the best-fit double power law reported in the same work (dashed line). The shaded regions show the rms scatter of the four simulations around the mean. The horizontal dot-dashed line highlights the value of ϕ corresponding to one object per simulation box.

faint sources).

We employ a lightbulb model to describe the QSO activity. Sources are randomly switched on with a probability that is independent of the properties of the host halo. Once activated, a QSO has a constant emissivity for a lifetime of 45 Myr and is switched off afterwards. Each source can become active multiple times during a simulation run. The resulting duty cycle is consistent with many observational studies which, however, set only weak constraints [320, 327–336].

The fraction of active sources at $z \sim 4$ is determined by matching the amplitude of the QLF measured by [301, see Fig. 4.1]. Its redshift dependence, instead, is determined by adopting a ‘pure density evolution’ model, as follows. First, we assume that the shape of the QLF does not evolve (which is consistent, to first approximation, with the results in 301). Second, we change the fraction of active sources so that to match the evolution of the emissivity at 912 \AA , $\epsilon_{912}(z)$, obtained by MH2015 after extrapolating down to $z = 12$ a collection of observational data at $z \lesssim 6$. In practice, this is done by changing the number of active sources, $N_{\text{src,active}}(L, z)$, according to the relation

$$N_{\text{src,active}}(L, z) = C(z) N_{\text{src,active}}(L, z = 4), \quad (4.2)$$

where

$$C(z) = \epsilon_{912}(z) / \epsilon_{912}(z = 4). \quad (4.3)$$

This procedure ensures that our integrated emissivity exactly matches the input used in the analytical model by MH2015. On average, we end up having between 120 and 400 active sources within a single simulation box, the number increasing with time.

We model the rest-frame QSO spectral energy distribution with a broken power law:

$$f(\nu) \propto \begin{cases} \nu^{\alpha_{\text{FUV}}}, & \lambda \geq \lambda_b \\ \nu^{\alpha_{\text{EUV}}}, & \lambda < \lambda_b \end{cases} \quad (4.4)$$

where $f(\nu)$ is the energy flux, α_{FUV} and α_{EUV} are the spectral indices in the far UV and extreme UV, respectively, and λ_b is the junction point of the two power-laws. Following [337], we assume $\lambda_b = 912 \text{ \AA}$ and assign to each source a pair of spectral indices sampled from two Gaussian distributions with means and standard deviations corresponding to $\alpha_{\text{FUV}} = -0.61 \pm 0.01$ and $\alpha_{\text{EUV}} = -1.7 \pm 0.61$, respectively. This matches the observed spectrum of low-redshift QSOs corrected for IGM absorption.

Propagation of radiation

In order to model the radiation transport, we employ an upgraded version of the three-dimensional RT code RADAMESH [141]. This software implements an efficient photon-conserving ray-tracing algorithm and is designed for AMR grids. RADAMESH uses a cell-by-cell Monte Carlo scheme to sample the radiation field at each location. The temperature and ionization state of each resolution element are computed using a non-equilibrium fully-implicit chemistry solver that includes six different species (HI, HII, HeI, HeII, HeIII and e^-).

In order to limit the computational time to an acceptable amount, we artificially decouple the RT from the hydrodynamic evolution of the gas. We thus post-process the $z = 4$ snapshot of the hydro simulations with the RT code. Ionizing photons emitted from the discrete sources described in Section 4.2.2 are propagated through the simulation box. The gas density, temperature and ionization states are updated keeping into account the local photoionization, photoheating, recombination and cooling rates as well as the expansion of the Universe. However, the spatial pattern of the density fluctuations is fully determined by the $z = 4$ output of the hydro simulation. We briefly comment on the robustness of this approximate method in the next Section.

To ensure a proper comparison with the analytical study by MH2015, we assume that the first QSOs light up at $z_{\text{start}} = 12$ which is compatible with the predictions of large cosmological simulations [e.g. 104]. The RT runs are then evolved until redshift $z_{\text{end}} = 3.5$, when both hydrogen and helium are completely ionized (i.e. their neutral volume fraction is less than 10^{-5}).

We sample the radiation spectrum between 1 and 40 Ry using 50 bins logarithmically spaced within three sub intervals starting at the ionizing thresholds of HI, HeI, and HeII. In details, we use 10 bins between 1 and 1.81 Ry, 10 bins between 1.81 and 4 Ry, and 30 bins in the range (4, 40] Ry. Further increasing the number of bins or modifying their frequency range produces only negligible changes in the gas temperature (see Appendix B in CCP2013 for a convergence test). Note that our simulations include soft X-rays that, thanks to their long mean free path, pre-heat the gas ahead of the ionization fronts. On the other hand, we neglect secondary ionizations that are expected to have only a minor impact [338–340].

Sources outside of the simulation box could, in principle, affect the computational volume. In order to estimate their contribution, we assume each QSO influences a Strömgen sphere of radius R_i (depending on the QSO magnitude, among other parameters) around itself following [341]. Hence, only sources within a cubical shell of thickness R_i surrounding the simulation box can influence our simulation. (Note that this is a very conservative approach, as the overlap between the Strömgen sphere of most sources in such shell and the simulation box is small.) Nevertheless, we compute the expected number of sources in such a shell integrating the QLF multiplied by the volume associated to each magnitude. This number never exceeds one for any realistic combination of QSO lifetime and ionization state at $z \gtrsim 6$.

At late times, when the gas in the simulations is almost completely ionized, the mean free path of the most energetic photons can exceed the box size. In order to reduce the computational time, we discard the photon packets that freely traverse the box two times (at variance with CCP2014 where they were replaced by a uniform background). This approximation might slightly shift our results towards higher optical depths at the very end of the EoR.

Post-process RT: motivations and accuracy

RT is a very computationally intensive problem. The intensity of radiation depends on seven variables (three spatial and two angular coordinates as well as time and photon energy) and the RT equation is non local. In consequence, for the current technology, coupled RT and hydrodynamic equations turn out to be too challenging to solve within large spatial domains without making simplifying assumptions. Different approaches have been followed in the literature to study the EoR. Some authors prefer to study the coupled evolution at the price of introducing crude approximations in the RT modelling (e.g. monochromatic radiation) and/or considering limited volumes [e.g. 342–345]. Others employ more detailed RT algorithms at the cost of decoupling them from the hydrodynamics [e.g. 312, 339, 346–349].

In this work, we follow the second approach in order to simulate a representative cosmological volume and suppress random fluctuations in the number of rare sources like QSOs. This strategy also offers us the possibility of comparing our results with the analysis of the standard EoR scenario presented in CCP2013 and CCP2014 using the same numerical setup.

It has been shown that decoupling the RT from the hydrodynamical response of the gas has a small impact on the models for the EoR. For instance, [350] found that gas velocities are typically altered by $\sim 1 \text{ km s}^{-1}$ while gas densities change by less than 10 per cent. Similar conclusions have been reached by employing the same codes and setup used in this work (see Appendix A in CCP2013): the gas density is altered by less than ~ 5 per cent down to $z = 3.2$ with the largest deviations seen in filamentary regions around mean density. We are thus confident that our results are sufficiently robust and accurate.

4.3 Results

In order to give a visual impression of the development of the EoR, Fig. 4.2 shows a series of snapshots extracted from one of our simulations and displaying the redshift evolution of different physical quantities. From left to right, columns refer to $z = 10$, 8, and 6, respectively. The top panels display the baryonic overdensity $\Delta_b(\mathbf{x}) \equiv \rho_b(\mathbf{x})/\bar{\rho}_b$, where $\rho_b(\mathbf{x})$ is the baryon density and $\bar{\rho}_b$ denotes its mean value within the box. Over plot are the projected positions of the nearby active sources, color-coded in such a way that redder colors correspond to brighter QSOs. The second row of panels illustrates changes in the gas temperature, while the last two exhibit the evolution of the HII and HeIII fractions, respectively. Note that, contrary to what happens in the standard scenario, hydrogen and helium get fully ionized simultaneously at a given location. When dominated by QSOs, cosmic reionization proceeds in a very inhomogeneous fashion. First, individual ionized bubbles are formed that then percolate.

This aspect is further elucidated in Fig. 4.3 where we show a time sequence of volume renderings of the HI ionization fronts (here defined as the regions where the local HII fraction is 50 per cent). A topological change due to the percolation transition is clearly noticeable at $z \sim 6$.

4.3.1 Ionized fractions

In Fig. 4.4, we provide a first quantitative evaluation of the impact of early QSOs on the EoR by studying the redshift evolution of the ionized volume fraction (often referred to also as the ‘volume filling factor’)

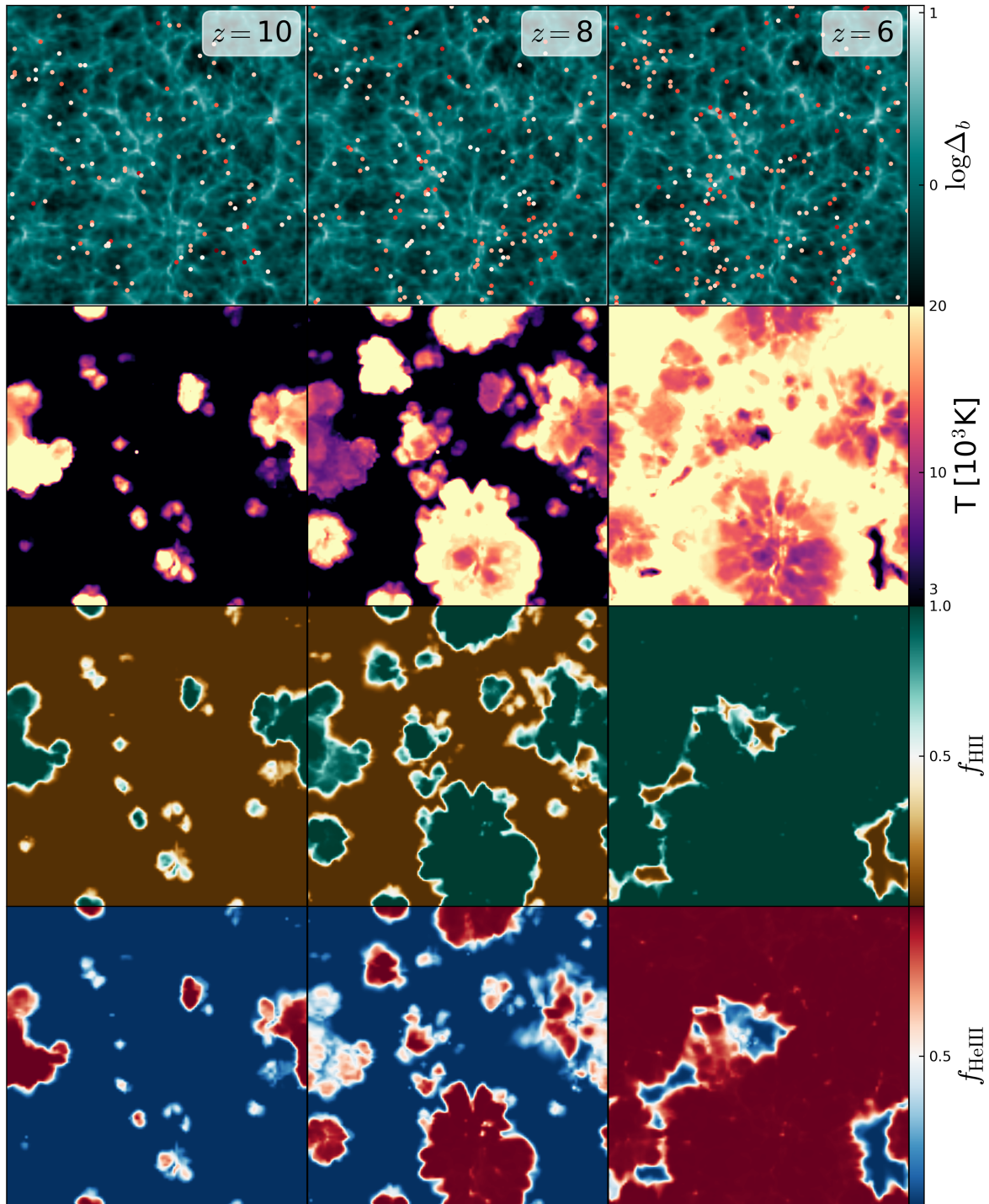


Figure 4.2: Simulation snapshots referring to a thin slice passing through the centre of one of our boxes. The time evolution proceeds from left to right across the frames that correspond to $z = 10, 8$ and 6 . In the top row, the baryon overdensity is shown together with the projected position of the active sources located within $\sim 4 h^{-1} \text{ Mpc}$ from the slice (redder colors denote brighter sources). The second, third and fourth rows display the gas temperature as well as the HIII and HeIII volume fractions, respectively.

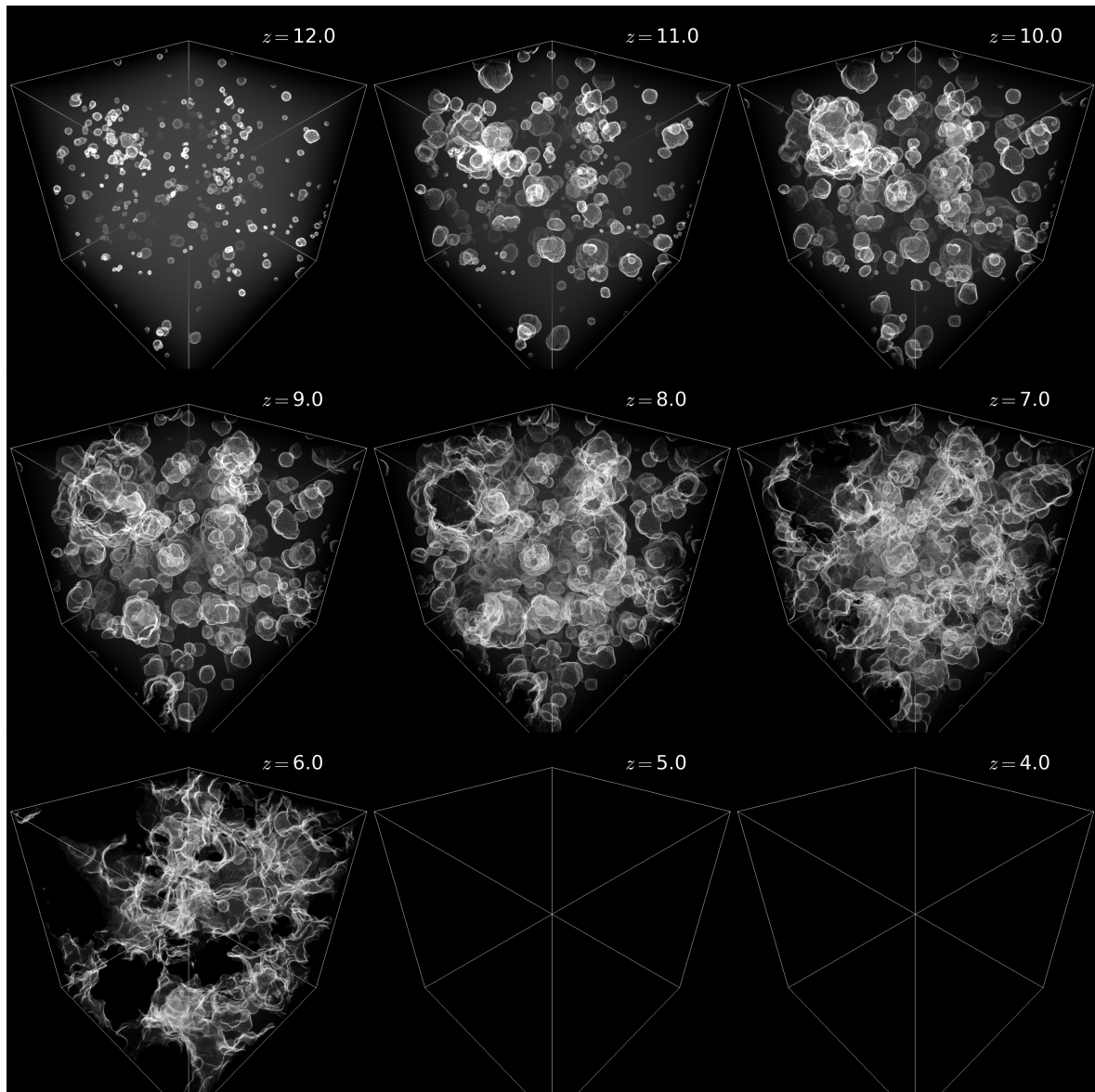


Figure 4.3: Volume rendering of the HI ionization front in one of our simulations at different redshifts. Neutral gas is shown in semi-transparent white, while the ionization fronts (defined as the regions where the local HII fraction is 50 per cent) are shown using opaque white.

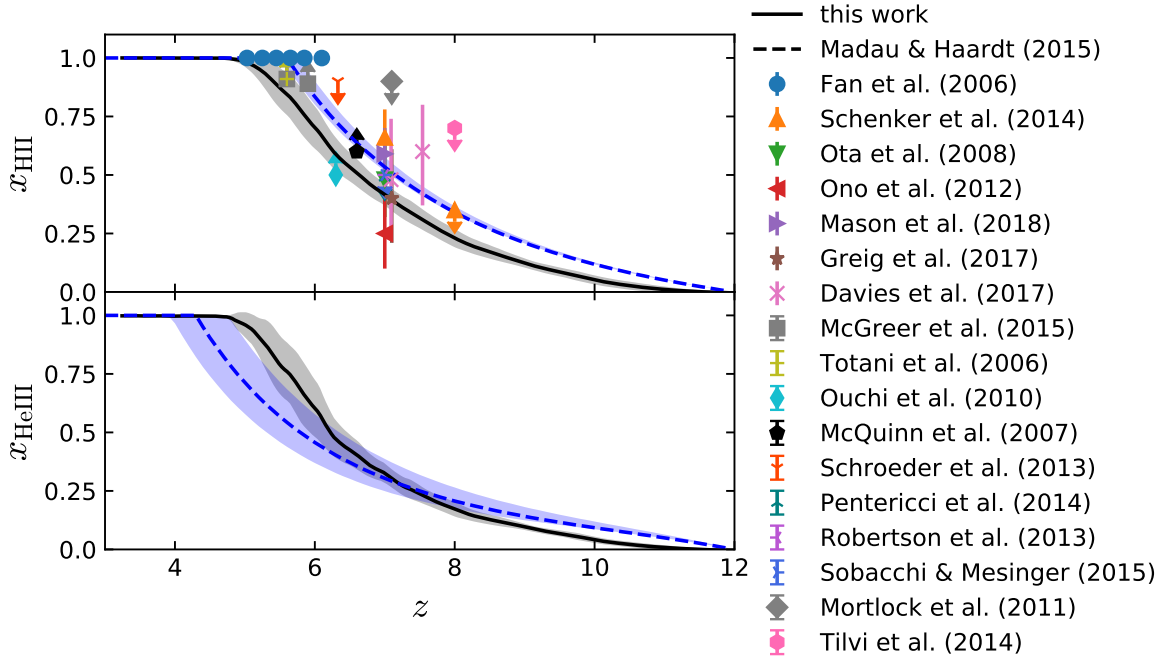


Figure 4.4: Volume fraction of HII (top) and HeIII (bottom) computed from our simulation suite. The solid lines and the surrounding shaded regions show the mean and the rms scatter among the four realizations. The dashed lines indicate the predictions by MH2015 and the shaded areas around them describe the effect of varying the parameters of their analytical model. The symbols correspond to a collection of constraints on the hydrogen ionized fraction as indicated by the labels.

for HII (x_{HII} , top panel) and HeIII (x_{HeIII} , bottom panel). We do not show the HeII fraction here (nor we discuss it elsewhere in the paper) as it matches almost perfectly x_{HII} as a consequence of the hard radiation spectrum emitted by QSOs and the close first-ionization energies of hydrogen and helium. The solid line indicates the average over our simulations and the surrounding light shaded region denotes the corresponding rms value. The four runs are in very good agreement and the scatter among them is small. Different symbols indicate a number of observational constraints on the HII fraction [117–119, 127, 129, 132, 137, 351–360]. This confirms that the QSO-dominated model produces enough photons to generate an EoR and keep the IGM ionized afterwards as suggested by previous analytical work. An obvious benchmark for our simulations is the MH2015 model (dashed line) which predicts similar volume fractions. Some important differences can nevertheless be appreciated: in our simulations, reionization proceeds slower at $z \gtrsim 9$ and becomes faster at $z \lesssim 7.5$. The reason is that MH2015 describe the ionizing photons as an uniform UV background and do not consider the precise location of the sources as well as RT effects. However, our simulated QSOs reside in highly overdense regions of the Universe that are characterized by a faster recombination rate than average. The net effect is to slow down the progression of the reionization process around the active sources. Later on, when the overdense patches are completely ionized, the ionization fronts reach underdense regions, in which reionization takes place faster than in the analytical model.

As we have briefly mentioned above, a striking feature characterizing the QSO-dominated scenario (compared with the standard model of the EoR) is the nearly simultaneous ionization of HI and HeII. This is a direct consequence of the assumption that only one population of sources provides all the

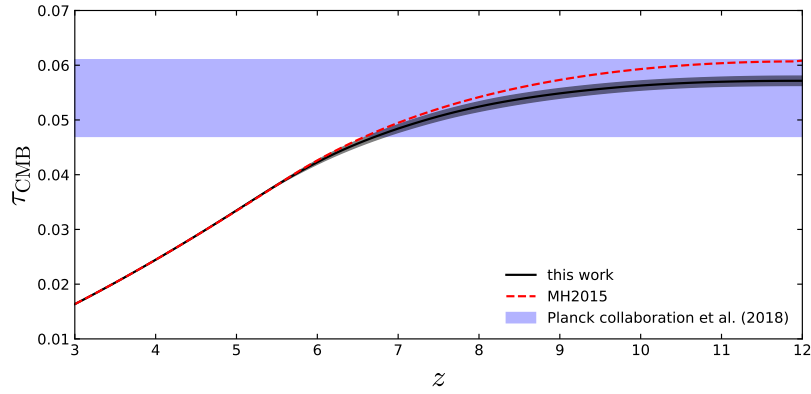


Figure 4.5: Optical depth to Thomson scattering integrated from the present time to redshift z . The solid line and the surrounding shaded region correspond to the results from our simulations shown in Fig. 4.4. The dashed curve shows the prediction by MH2015. The large shaded area highlights the current observational constraints for the CMB at $z \sim 1100$ [17].

ionizing photons for both species. By directly comparing the evolution of x_{HII} and x_{HeIII} in Fig. 4.4, it emerges that the volume fraction of ionized hydrogen is a bit higher at all times. This small delay in the reionization of helium reflects the shape of the QSO spectrum that gives less ionizing photons per helium atom than for hydrogen (see, however, the discussion in Section 4.5 on the impact of the escape fraction).

The peculiar reionization histories in the QSO-only scenario modify the number density of free electrons in the IGM with respect to the standard model of the EoR. In Fig. 4.5, we show that the resulting optical depth of CMB radiation to Thomson scattering, τ_{CMB} , still lies within the observational constraints [17] as also derived by MH2015 (dashed lines).

4.3.2 IGM temperature

Although analytic models of reionization can compute the ionized volume fractions rather accurately, they cannot make robust predictions for the IGM temperature which is heavily influenced by RT effects. For instance, MH2015 assume that the IGM has a uniform temperature of $T_{\text{IGM}} = 2 \times 10^4$ K, neglecting any dependence on redshift or density. In Fig. 4.6, we show the redshift evolution of the gas temperature at mean density (T_0) in our simulations. The solid line and the shaded area around it denote the mean and the associated scatter among all the mean-density cells in the four realizations. For completeness, we extrapolate T_0 at $z < 3.5$ (dashed line) as in [361] by taking into account that, when the gas is fully ionized, the temperature at mean density is determined by the adiabatic expansion of the Universe (plus smaller contributions due to Compton and free-free cooling). Overall, the IGM is photo-heated until $z \simeq 5.5$ and cools down afterwards. Note that, excluding its maximum value, $T_0 \ll 2 \times 10^4$ K at all times.

Several observational constraints published by various authors using substantially different methods are overplotted in Fig. 4.6. Namely, we show the results obtained by [362, using the distribution of line widths in the Ly α forest], [363, from the Doppler parameter in the quasar proximity zone], [364, from the curvature statistic], [365, via a wavelet filtering analysis], [366, from the distribution of line widths], [367, employing the curvature statistic], [368, using the Morlet wavelet filter analysis], [369, from the joint distribution of HI column densities and Doppler parameters], [370, using the flux power spectrum], [371, employing the cutoff in the Doppler parameter distribution] and [372, using the Ly α forest power spectrum]. Although statistical errorbars tend to be large and different methods do not

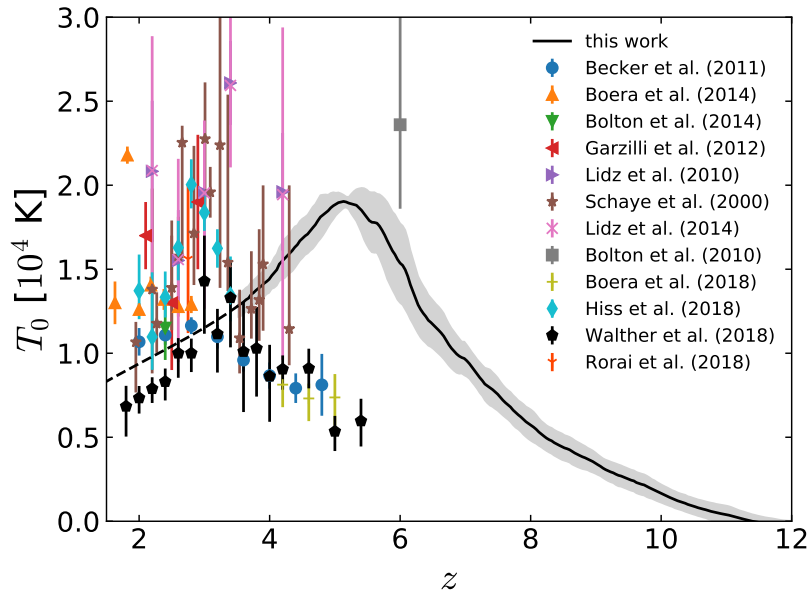


Figure 4.6: Volume-weighted average temperature of the IGM at mean density, T_0 , as a function of redshift. The average (solid line) and the rms scatter (shaded area) are evaluated over the entire simulation suite. For $z < 3.5$, we use an analytical approximation to extrapolate the evolution of T_0 beyond the range covered by the simulations (dashed line). The symbols show a collection of observational data (see the main text for details).

always match, the available data show a peak around $z \approx 3.5$, which is usually interpreted as a signature of late helium reionization [e.g. 283, and references therein]. This clearly poses a severe challenge to the QSO-dominated model which cannot accommodate such a late local maximum in $T_0(z)$. In general, it is impossible to fit the existing temperature constraints if HeII reionization takes place at $z > 4.5$ [305, 306].

4.4 Synthetic observations

The hydrogen and helium Ly α forests are powerful probes of the IGM properties. In this Section, we use our simulations of the QSO-dominated reionization model to produce synthetic absorption-line spectra for HI and HeII that we then compare with observational data and previous numerical studies. Finally, we suggest new ways to analyse the experimental data and better constrain the QSO contribution to reionization.

The mock spectra are generated as in CCP2013. In brief, we compute the IGM absorption profile as a function of wavelength by keeping into account the effects of density, temperature and velocity. For each simulation snapshot, we consider 100 random lines of sight, each one extending for $100 h^{-1}$ Mpc. In total, we produce ~ 12000 spectra with an initial resolution of 1 km s^{-1} that we subsequently degrade by using a Gaussian filter with a full width at half maximum of 88 km s^{-1} in order to mimic the instrumental response of an actual spectrograph. The smoothing length matches the nominal resolution of our simulations in low-density regions at $z \approx 3.5$. Although our mock spectra do not resolve individual absorption features in the Ly α forest, they do encode information about the IGM opacity.

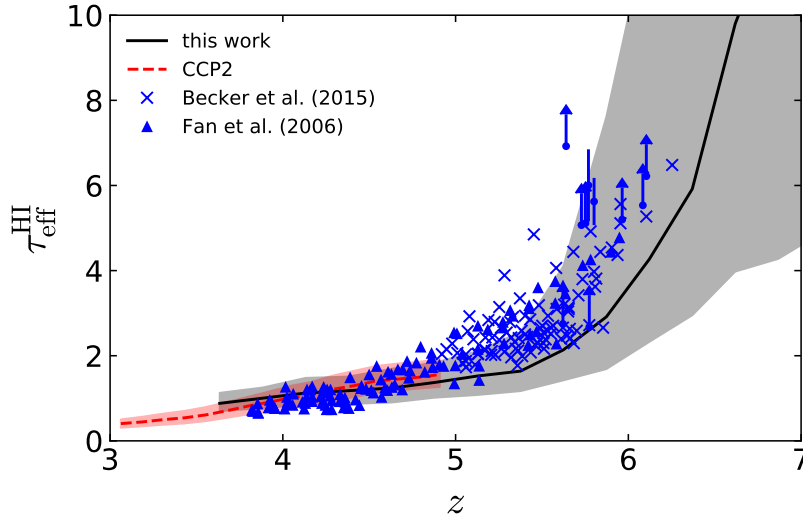


Figure 4.7: The redshift evolution of the HI effective optical depth computed from synthetic spectra in different numerical simulations is compared with recent observational estimates. The solid line shows the median value obtained from our simulation suite of the QSO-dominated scenario for the EoR. The corresponding evolution in the standard model of reionization (see CCP2014) is displayed with a dashed line. In both cases, the shading indicates the central 68 per cent of data. The observational results by [108] and [127] are shown with triangles and crosses (or vertical arrows for lower limits), respectively.

4.4.1 Effective optical depths

The evolution of the effective optical depth, τ_{eff} , has emerged as one of the most widely used characterizations of the Ly α forest. In order to evaluate this statistic for our simulations, we first divide each synthetic spectrum in chunks of size $\Delta z = 0.1$ [as in e.g. 284] and compute the (continuum-normalized) mean transmitted flux in it, $0 \leq \langle F \rangle \leq 1$. The effective optical depth is then obtained using $\tau_{\text{eff}} = -\ln(\langle F \rangle)$.

The resulting values for the HI forest are plotted in Fig. 4.7. The solid line shows the median value in each redshift bin and the surrounding shaded region encloses the central 68 per cent of the data. For comparison, we also display the results obtained by CCP2014 within the standard scenario for reionization (dashed line and shaded region). The large scatter seen in our simulations at $z \gtrsim 5.5$ is a clear indication of patchy reionization caused by the low number density of QSOs (see also Section 4.4.2). Overplotted are observational data for 42 quasar spectra [108, 127]. At $z \lesssim 4.5$, the simulations are in excellent agreement with the observations, especially taking into account that they should be slightly biased towards higher effective optical depths at low redshifts (see Section 4.2.2). On the other hand, at higher redshifts, the IGM in the simulations tends to be too transparent, with most of the observational data falling in the upper half of the synthetic distribution of $\tau_{\text{eff}}^{\text{HI}}$.

We repeat the same analysis for the HeII Ly α forest but using chunks with $\Delta z = 0.04$ as in [107]. The late evolution² of $\tau_{\text{eff}}^{\text{HeII}}$ is plotted in Fig. 4.8, together with recent measurements from [107] and [293, containing an extensive re-analysis of data from Worseck et al. 2016]. Despite the small number

² In the QSO-dominated model, $\tau_{\text{eff}}^{\text{HeII}}$ changes in a peculiar way with redshift. After the first QSOs become active, HeII is present only in between the hydrogen and helium ionization fronts which are generally close in space. Therefore, the effective optical depth assumes rather low values at early times ($\tau_{\text{eff}}^{\text{HeII}} \lesssim 6$) that steadily grow as the separation between the hydrogen and helium fronts increases due to the steep spectral index of the ionizing radiation. The effective optical depth reaches its maximum value around the epoch of hydrogen reionization and decreases afterwards. In fact, once the HII bubbles percolate,

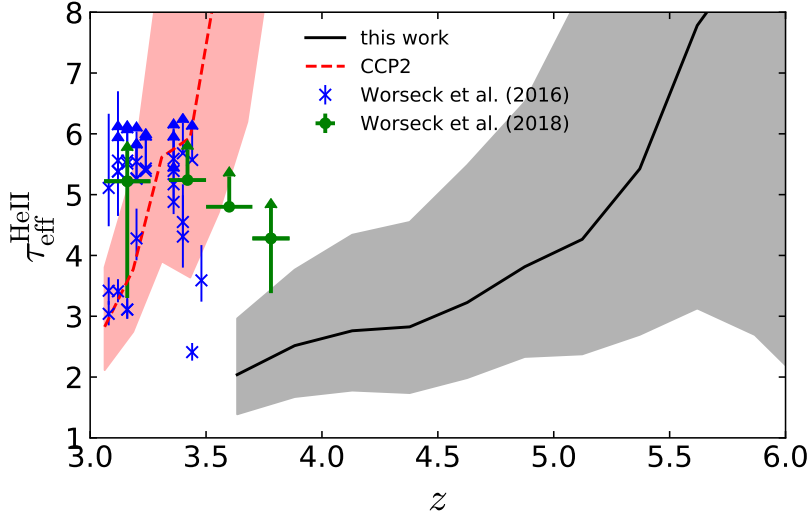


Figure 4.8: As in Fig. 4.7 but for the HeII effective optical depth. The data points indicate the measurements by [107, crosses] and [293, dots], including an extensive re-analysis of data from Worseck et al. 2016. For visual clarity only the median and 68 per cent central data within each redshift bin are shown].

of experimental data in the redshift range covered by our simulations, the model and the observations are in strong tension. In fact, the optical depths predicted by the QSO-dominated scenario at $z \approx 3.7$ are substantially lower than the observed ones at $z = 3.4$. On the contrary, the standard reionization scenario is in good agreement with the available data.

In summary, the QSO-dominated scenario we have simulated does not match the observed evolution of the IGM opacity. For what concerns HI, however, a moderate delay in the appearance of the first active sources and/or a steeper evolution of the ionizing emissivity could reduce (and likely completely remove) the small tension we have found with the data at intermediate redshifts. Conversely, it does not seem possible to reconcile the model and the data for HeII by making small adjustments. Simply, helium reionization is completed too early in the QSO-dominated scenario.

4.4.2 The probability distribution function of optical depths

The spread in $\tau_{\text{eff}}^{\text{HI}}$ recorded at fixed redshift indicates that the opacity of the intergalactic hydrogen varies between different sightlines. The cumulative distribution function (CDF) of $\tau_{\text{eff}}^{\text{HI}}$ thus provides a simple and convenient characterization of these local changes. In Fig. 4.9, we plot the CDF measured by [108] using spectral chunks with a comoving length of $50 h^{-1}$ Mpc. It is well known that these results, that have been recently confirmed with increased statistical significance [109, 296], are inconsistent with the distribution inferred from numerical simulations of the standard reionization model that employ a uniform UV background³ calibrated to match the observed low-optical-depth data (see the dashed lines in Fig. 4.9). In fact, the CDF extracted from the simulations is too steep and can not reproduce the extended tail of large optical depths observed at redshift $z \gtrsim 5$ [108]. It is thus interesting to verify whether the QSO-dominated scenario (with its rarer ionizing sources) may help reconciling the discordance

HeII regions find themselves illuminated by multiple sources and are rapidly turned into HeIII.

³ Although using a smooth radiation field represents a rather crude approximation during the early phases of the EoR, it should be a sufficiently good working hypothesis after bubble percolation (i.e. at $z \lesssim 6$).

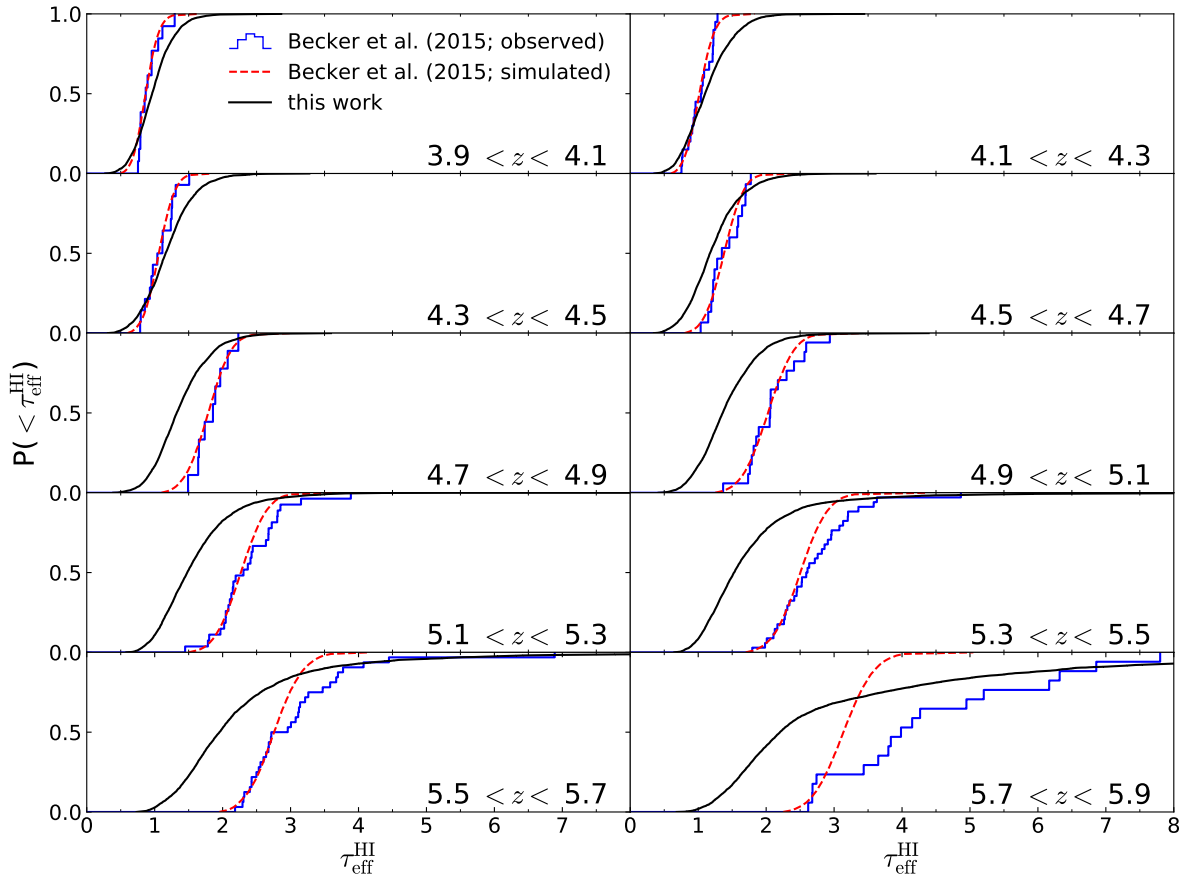


Figure 4.9: Cumulative distribution function of the HI effective optical depth. The solid curve shows the median over our simulations. The histogram displays the observational results by [108], while the dashed curve indicates the CDF predicted using numerical simulations of a standard reionization history calibrated to match the low-optical-depth end of the observed distribution (also from 108). Each panel corresponds to a different redshift bin as indicated by the labels.

with the observations. The solid lines in Fig. 4.9 represent the CDF obtained from our mock spectra. Before proceeding with the comparison, it is important to stress that our optical depths have not been calibrated to match any part of the observed CDF. In general, the modified scenario for the EoR does not reproduce the observations at any redshift. At $z \lesssim 4.5$, the observed CDF is steeper than the simulated one, meaning that the IGM is more homogeneous than predicted by the QSO-dominated model. Including fainter QSOs in the simulations may relieve this tension, as a larger number density of sources can produce a more homogeneous IGM. At $4.5 \lesssim z \lesssim 5.5$, the simulated CDF has the correct shape but is systematically shifted towards lower optical depths (as already seen in Fig. 4.7). At even higher redshift, the disagreement increases at small optical depths but the synthetic CDF nicely reproduces the high- $\tau_{\text{eff}}^{\text{HI}}$ tails of the distribution. This is the opposite trend to that expected in the standard reionization model [108]. It is therefore tempting to interpret our results as implying that an increased QSO contribution at high redshift (with respect to the standard reionization history, see also 294) might bring the theoretical predictions in agreement with observations. Dedicated numerical studies are necessary in order to settle this issue which is beyond the scope of this paper.

In this Section and the next one, we use our synthetic spectra to explore possible ways of gauging the QSO contribution to cosmic reionization with observational data. We proceed by comparing the predictions of the QSO-dominated scenario with those of the standard model. For the latter, we use the results presented in CCP2014. Our analysis does not involve any fine tuning of the model parameters and, as such, is qualitative in nature. Our intention is to provide a guideline for future studies that will employ hybrid populations of ionizing sources in order to make more quantitative statements.

We first isolate specific features generated by HI and HeII Ly α absorption in QSO spectra and characterize them in terms of four numbers. Following CCP2013, we consider the width of flux-transmission windows (FTW) defined as the (simply connected) regions where the transmitted flux is everywhere greater than 20 per cent of the continuum level. We also examine the length of dark gaps (DG) that are intended as the extended regions where the flux is everywhere below 10 per cent of the continuum level. Finally, we look at transmission peaks [297, 373] that we define as the continuous regions where the flux always lies above a threshold value of 0.5 times the maximum transmitted flux within the segment. In particular, we record the width and the maximum height of the peaks (hereafter PKw and PKh, respectively). For this analysis, in order to avoid classifying small local fluctuations as peaks, we add Gaussian noise with an rms value of $F_{\text{noise}} = 0.05$ to the synthetic spectra and only consider peaks with a signal-to-noise ratio greater than 3.

Our results are shown in Fig. 4.10 for the HI Ly α forest and in Fig. 4.11 for the HeII spectra. In both cases, we compare the quasar-only scenario (solid lines) with the standard one as computed in CCP2014 (dashed lines) and focus on $z \lesssim 4.5$. Shown are the density distributions of the different features per comoving pathlength in h^{-1} Mpc. For HI, the two models give very similar results as hydrogen is highly ionized in the post-overlap phase and the transmissivity in the spectra is mostly dictated by the underlying density field. Small deviations are noticeable at late times because the models generate different intensities of the UV background. Overall, the distribution of DG widths (w_{DG}) shifts towards shorter values as the redshift decreases (see the rightmost column in Fig. 4.10) as a consequence of the increasing ionization level of the IGM. Complementarily, the widths of FTWs (w_{FTW} , leftmost column) and PKs (w_{PK} , third column from the left) tend to increase. On the other hand, the distribution of peak heights (h_{PK} , second column) hardly changes with time.

The two scenarios for the EoR, however, make very different predictions for the HeII spectra. Because of the late reionization of HeII, the standard model of reionization generates many less features than the QSO-dominated scenario. Moreover, their distributions rapidly evolve with time thus showing the opposite trend as in the QSO-dominated scenario where HeII reionization takes place much earlier. It is worth noticing that, in the standard case, the widths of FTWs and PKs are usually smaller than for HI as

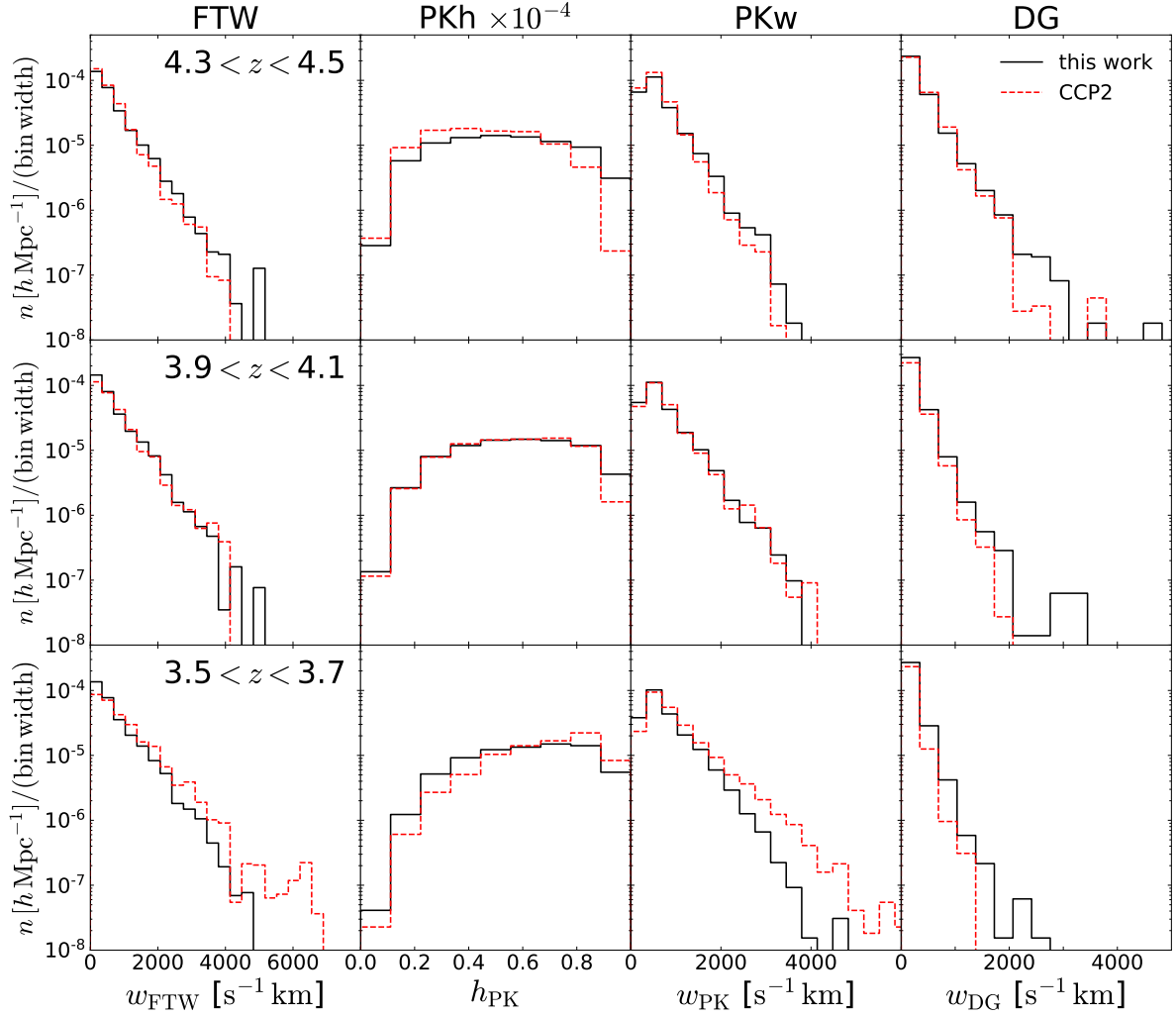


Figure 4.10: Distribution of shape properties of transmission peaks and dark gaps in synthetic spectra of the HI Ly α forest. Each row refers to a different redshift reported in the leftmost panel. Each column shows the density distribution along synthetic sightlines of (from left to right) the width of flux transmission windows, the height (rescaled by a factor 10^{-4} for visual clarity) and width of transmission peaks and the size of dark gaps. A precise definition of these quantities is given in the text. Solid lines show the result for our simulations while dashed lines refer to the standard reionization history and employ the simulations of CCP2014.

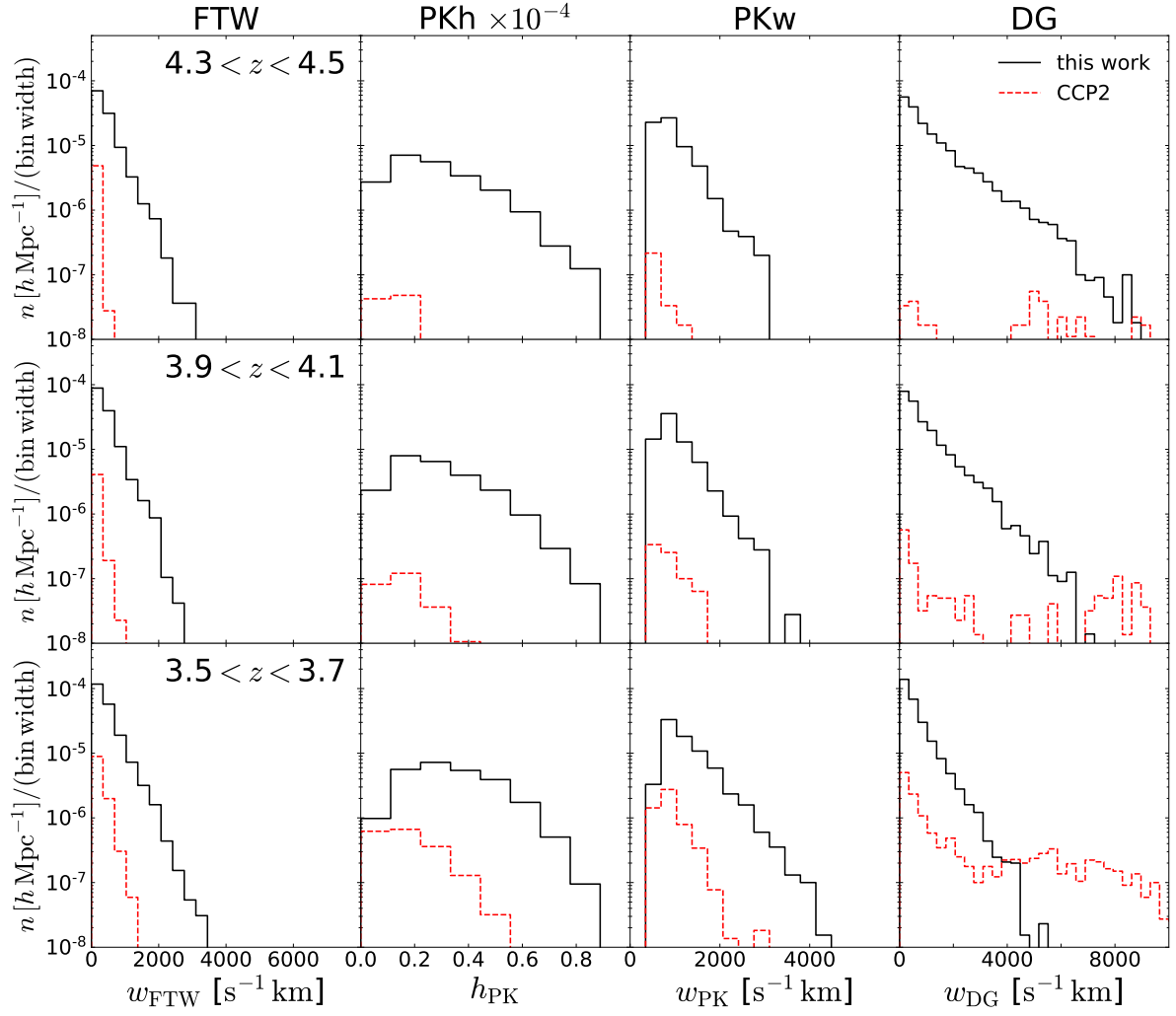


Figure 4.11: As in Fig. 4.10 but for the HeII Ly α forest. Notice the different horizontal scale in the rightmost column.

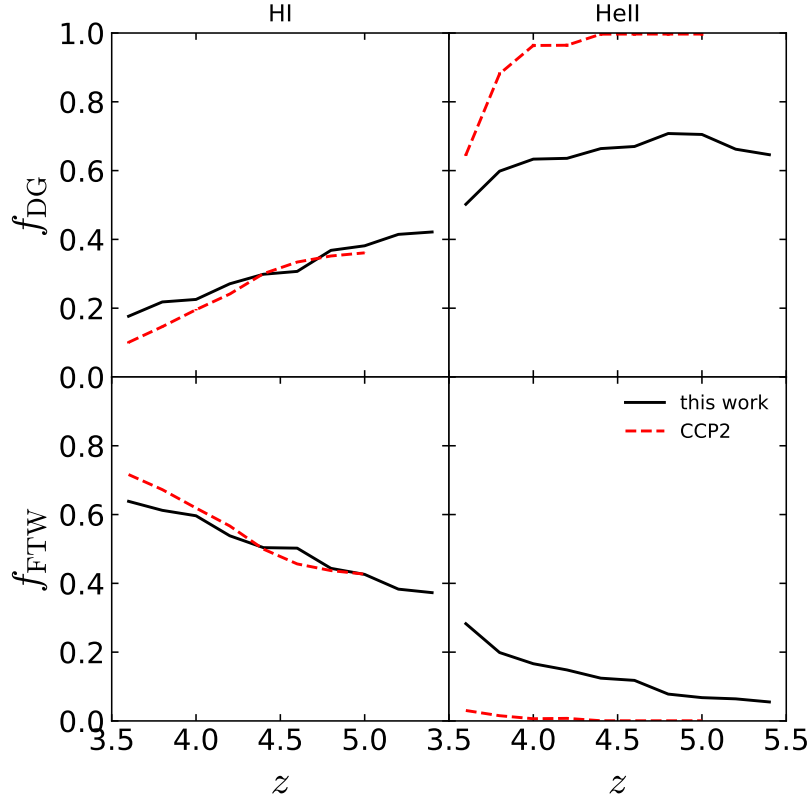


Figure 4.12: Average fraction of a spectrum classified as DGs (top) or FTWs (bottom) as a function of redshift. The panels on the left-hand side refer to the HI Ly α forest and those on the right-hand side to HeII. The solid lines show the evolution in our set of simulations of the QSO-dominated scenario, while the dashed ones show the results of CCP2014 for the standard model of the EoR. Statistical errors are always smaller than the line thickness.

a consequence of the reduced number of ionizing photons available. Complementarily, the width of DGs is larger. In particular, at $z \approx 3.6$, the standard scenario generates a prominent tail of very long DGs with $w_{\text{DG}} \gtrsim 4500 \text{ km s}^{-1}$ that is not present in the QSO-dominated case because of the higher number density of hard photons.

At first sight, it might be surprising that the number densities of both FTWs and DGs are small at high redshift. The reason is that our analysis equally weights long and short features, i.e. a completely absorbed spectrum will account for only one (long) DG, whilst a typical line of sight showing the Ly α forest will produce hundreds of DGs. In order to provide the missing information, in Fig. 4.12, we plot the evolution of the mean fraction of the spectra which is assigned to DGs (f_{DG} , top) or FTWs (f_{FTW} , bottom). As expected, the portion of the spectra which is identified as FTWs increases with time while f_{DG} decreases. Once again, results for HI are very similar in the two scenarios while they strongly differ for HeII, reflecting the different timing of helium reionization. In particular, in the standard model, there is basically no transmitted flux for $z \gtrsim 4.5$ while 30 to 40 per cent of the pixels at these redshifts are not dark in the QSO-dominated scenario.

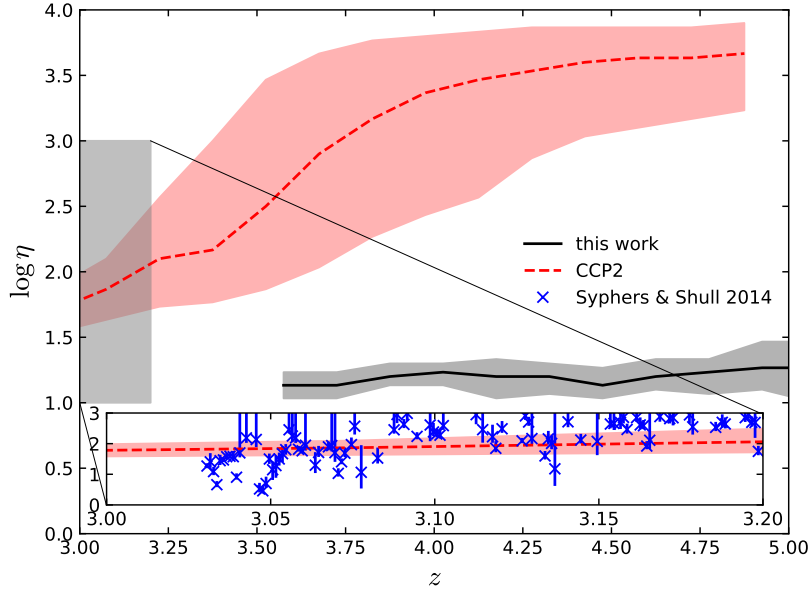


Figure 4.13: Percentiles of the distribution of the column density ratio, η , as a function of redshift. The lines show the median value extracted from our simulations (solid) and from those in CCP2014 (dashed) while the shaded regions enclose the central 68 per cent of the data. The rectangular box on the left-hand side indicates the area containing the observational results by [374] and is magnified in the inset for visual clarity.

4.4.3 The column-density ratio

An useful tool to constrain the QSO contribution is the HeII-to-HI column-density ratio, η . This quantity can be measured from QSO sightlines that are transparent in the Lyman continuum because no intervening Lyman limit systems block the UV part of the spectrum (hereafter HeII QSOs). For optically thin gas, the ratio encodes information on the spectral hardness of the ionizing radiation and thus on the relative contributions from hard (QSOs) and soft (stellar) sources.

In Fig. 4.13, we show how the probability density of η evolves as a function of redshift in our simulations and in those by CCP2014. The solid lines show the median column-density ratio and the dashed lines enclose the central 68 per cent of the data. Results are very different in the standard and in the QSO-dominated scenarios due to the different timing of He reionization. In the standard model, right after hydrogen reionization is completed, η assumes values of several thousands (meaning that little or no flux is transmitted at the frequency of the HeII Ly α transition) that tend to decrease with time and show a large scatter. In this case, η fluctuations mainly trace the HeII density and the patchiness of HeII-ionizing radiation. Later on, when also HeII is fully ionized, the η distribution presents a broad peak at $\eta \sim 200$ [see also 350]. On the other hand, in the QSO-dominated model, HI and HeII are ionized in parallel and their column-density ratio assumes significantly lower values, typically ranging between a few and a hundred at $z > 6$. As soon as the reionization of both species is completed, the PDF of η rapidly relaxes to its final form which sharply peaks at $\eta \sim 14$ and presents very little scatter.

Observations should be able to distinguish between these very different evolutionary paths and final states. Current statistical samples at $z \lesssim 2.7$ [291] provide a better match to the η -distribution generated during the standard reionization history. Consistently, rare data at higher redshifts present signs of incomplete HeII reionization at $z \gtrsim 3$ [e.g. 374]. It is thus plausible that collecting more HeII-

absorption spectra at $z \sim 3$ and contrasting them with custom-made numerical simulations might help us to precisely gauge the importance of the quasar contribution to the EoR.

4.5 Discussion and Conclusions

Determining the nature of the astrophysical sources of radiation that shaped the EoR continues to be an elusive goal. The tentative detection of a population of faint QSO candidates at high redshifts [301] led MH2015 to investigate a scenario in which the emission from active galactic nuclei dominates over the contribution of star-forming galaxies at all times. Their analytical calculations indicate that such a model is compatible with observations of the HI volume fraction and with the optical depth to Thomson scattering of the cosmic microwave background. In this paper, we have further scrutinized the QSO-dominated scenario by using more sophisticated tools. We have run full hydrodynamical simulations and post-processed their output with a radiative-transfer code in order to compute the evolution of the temperature and ionization state of the IGM. Subsequently, we assess the viability of the QSO-dominated scenario by producing synthetic absorption-line HI and HeII spectra from our simulations and comparing their properties with observations and with previous studies of the standard model for the EoR.

Our main results can be summarized as follows.

1. The HII and HeIII volume fractions extracted from our simulations of the QSO-dominated scenario are consistent with most observational constraints and with the analytical model by MH2015. Similarly, the Thomson optical depth of the IGM is in very good agreement with the latest measurements [17].
2. The striking feature that characterises the QSO-only scenario is that HI, HeI, and HeII reionization take place nearly at the same time. In consequence, the IGM temperature at mean density shows a single peak at redshift $z \approx 5.7$ (where $T_{0,\text{peak}} \approx 2 \times 10^4$ K). Compared with the bulk of the observed values, the model over predicts the IGM temperature at $4 < z < 5$ and under predicts it at $2 < z < 3$. In particular, due to the early completion of HeII reionization, the QSO-dominated model is inconsistent with the measurements that show a temperature peak at $z \approx 3$.
3. Correspondingly, the effective optical depth derived from our HeII Ly α synthetic spectra is significantly too low at $3 < z < 4$ to reproduce the observational constraints.
4. The redshift evolution of several features in the HeII Ly α absorption spectra easily differentiates the QSO-dominated model for the EoR from the standard one and could be used to set tight constraints on the onset of HeII reionization. Conversely, the properties of the HI Ly α forest are very similar in the two scenarios. Therefore, major progress in the field could be achieved by increasing the size of current samples of HeII quasars and extending them to higher redshifts.
5. Although the QSO-dominated model is not able to fully reproduce the observed PDF of the HI effective optical depth at $z \gtrsim 4.5$, it nicely generates very extended tails at high values that are not present in the standard scenario where the reionization of HI is much more spatially homogeneous and less patchy. This provides a hint that complementing the standard scenario with a sub-dominant population of high- z QSOs might be key to reconcile the observed distribution of optical depths with the predictions from numerical simulations.

In brief, our principal conclusion is that existing constraints on the IGM temperature and HeII opacity rule out the QSO-dominated scenario we have investigated. There is a possible caveat, however.

Throughout the paper, we have assumed that all UV photons escape their sources independently of wavelength. This is a common expectation motivated by the large luminosity of active galactic nuclei, although it has not been tested for the faint sources that generate most of the ionising photons at high redshift. By relaxing the hypothesis that $f_{\text{esc,QSO}} = 1$ across all (relevant) wavelengths and assuming that $f_{\text{esc,QSO}}(\sim 912 \text{ \AA}) > f_{\text{esc,QSO}}(\sim 228 \text{ \AA})$, it should be possible to delay the onset of HeII reionization and vastly improve the agreement with current observational constraints on the temperature of the IGM and the HeII opacity. This, however, will not modify much the PDF of the HI optical depth which is mainly influenced by radiation close to the hydrogen ionization threshold. Nevertheless, this distribution is also sensitive to sub-dominant contributions to the ionizing flux and dedicated simulations including also variable levels of stellar UV radiation need to be performed to address this issue in a more quantitative way.

Our results suggest that a rather extreme fine tuning of the escape fraction might be necessary to bring the QSO-dominated model for the EoR in agreement with existing observational data. Our analysis also reveals that developing a fully quantitative understanding of populations of sources that are active in the different phases of the EoR requires that future observational campaigns will collect many more HeII QSO spectra so that to enable statistical studies of their characteristic features.

Final remarks

This Thesis gathers together a series of studies investigating the interplay between different astrophysical scales. The influence that large scales have on smaller ones is addressed in Chapter 2, where we show how the cosmic web influence the properties of satellite galaxies. Similarly, in Chapter 3 we analyze what information about gravity, the force shaping the largest scales in the Universe, are encoded in the properties of small satellite galaxies. We then move to the analysis of the opposite clout, i.e. how small scales affect larger regions, by studying the effects of parsec-scale accretion in AGN on the reionization of the largest scales in the Universe (Chapter 4). In this Chapter we highlight the main results of these studies and describe future research directions.

5.1 A deeper understanding of assembly bias

Dark matter haloes of unequal age show different clustering properties. Many numerical investigations carried out in the past years have shown that the strength of this assembly bias correlates with the tidal field acting on the objects [e.g. 176, 177]. The ZOMG project (of which Chapter 2 is part) is a numerical endeavour aiming at clarifying the origin and effects of assembly bias, not only on DM (as historically done) but also on baryons. It has been shown that the different growth of ‘old’ and ‘young’ haloes is determined by their position within the cosmic web, that modulates the inflow of new material [98], but the central galaxies are only marginally affected by this [156]. In Chapter 2 we use state-of-the-art simulations to carry out a thorough investigation of the satellite populations of haloes with similar mass but different age. The majority of satellite properties are insensitive to the collapse time of the parent halo and their mass spectrum is comparable in ‘young’ and ‘old’ objects, both at accretion time and today. More than 80 per cent of these structures do not contain stars and almost all of them have been completely stripped of their gas content, half of which is subsequently ejected outside the host, while a small portion (correlated with the satellite mass, since massive objects are more resilient to gas stripping) of it manage to reach the central galactic disk. As a consequence, all these satellites have vanishing SFR.

The halo assembly history has a stronger impact on the dynamical properties of satellite galaxies, as a consequence of the different structure of the gravitational field around ‘young’ and ‘old’ haloes. Satellites are luminous tracers of the DM dynamics, and indeed we show their distribution of radial velocities strongly correlates with the cosmic web environment. In ‘young’ objects this quantity shows a prominent peak corresponding to radial infall, while no preferred direction can be identified in ‘old’ objects. To boost the applicability of our results, we condense this information into a single anisotropy parameter, easier to measure, that characterizes the motion of satellites within the halo and can be used to segregate hosts of different age. Finally, we apply this knowledge to the Milky Way, showing that the measured

motion of satellites indicates it is embedded in a ‘old’ DM halo.

The very-high resolution of the simulations employed in Chapter 2 is necessary to properly capture the physical mechanisms at the origin of the assembly bias and to properly resolve satellite properties. However, it also entails that such simulations are computationally expensive and, therefore, in this Thesis we focus on a narrow mass range (where the assembly bias signal is the strongest) and on the tails of the halo age distribution. A natural follow-up of this study is thus the inclusion of haloes with intermediate age, in order to properly understand the transition from the properties of ‘old’ haloes to the ones of ‘young’ objects, as well as the exploration of a broader mass spectrum. This will enable us to confirm the physical picture we draw in Chapter 2 and, possibly, to extend it to a broader range of environments.

5.2 The first prediction of the radial acceleration relation for small satellite galaxies

In recent years, an intense debate has sparked over the ability of the standard Λ CDM cosmology to explain the connection between dark and luminous components of galaxies known as radial acceleration relation (RAR). While many studies have addressed this issue in the context of central galaxies, the low-acceleration regime, dominated by satellites, was an uncharted territory. We explore this part of the parameter space in Chapter 3, where we exploit the superb resolution of the ZOMG simulation suite to provide the first-ever predictions of the location of satellite galaxies in the RAR plane. In the Λ CDM model, they follow the same relation as their host, although with a four times larger scatter. We show this by performing a Bayesian analysis that simultaneously constrain the best-fitting relation (in excellent agreement with the observed value) and its intrinsic scatter. Furthermore, we investigate the secondary dependence of the RAR on additional properties, showing that only the accretion time of the satellite correlates with the scatter. In particular, objects accreted earlier show a larger dispersion, demonstrating that the satellite-host interaction is the origin of their larger scatter. Exploiting our findings and the external field effect of the MOND, we devise a test that can discriminate between the Λ CDM and MOND cosmological models. Finally, we study the time evolution of the RAR and demonstrate that, in the Λ CDM model, the relation evolves mildly with redshift. In particular, the critical acceleration decreases with redshift, while the intrinsic scatter remains approximately constant. We isolated the physical mechanism responsible, namely the tidal stripping that affects preferentially the stellar component, followed by an internal re-adjustment of the DM.

Our results provide the scientific community with a powerful tool to test the mysterious DM on small scales. Once observational data will become sufficiently precise, this test can be applied to satellites of Local Group galaxies in order to disprove either the Λ CDM or MOND theory. Data taken by the GAIA¹ spacecraft include some of the Milky Way satellite galaxies and will improve over time, hopefully enabling in the future such a test.

5.3 The role of quasars in cosmic reionization

Quasars have been recently proposed as important, even dominant, source of ionizing photons during the epoch of reionization. This idea roots in recent observations showing orders-of-magnitude more candidate quasars than expected at $z \sim 6$ [301]. A number of studies have investigated their role either using approximate methods for the radiative transfer or small volumes [294, 305–311]. The former approach hinders the possibility to produce realistic synthetic spectra, while the latter is sensitive to

¹ <http://sci.esa.int/gaia/>

sample variance. In Chapter 4 we amend this by running large-scale, radiative-transfer simulations of a reionization history dominated by QSOs at all cosmic epochs. We show that the volume fractions of ionized hydrogen and helium are consistent with analytical predictions, while the Thomson optical depth of CMB photons is well within the PLANCK limits [20]. In this model hydrogen and helium reionization occur in a short time span. Consequently, the IGM temperature at mean density has a single peak at $z \approx 5.7$, in tension with measurements showing a maximum at $z \approx 3.5$. For the same reason, the HeII optical depth is lower than available data. A different measure of the IGM inhomogeneity is provided by the distribution of optical depths in chunks of quasar sightlines. Our simulations are able to reproduce the long, high-optical-depth tails found in observations, but they fail in matching the low- τ part of the distribution.

We characterize the absorption and transmission regions in synthetic spectra of the Ly α forest with a set of shape parameters and show that, in the case of HeII, these are very sensitive to the sources dominant during the EoR. However, using such properties to put observational constraints is impractical as a consequence of the large amount of sightlines required. Hence, we distill the information contained in the distribution into more accessible quantities. Among them, the most promising is the fraction of pixels in a spectrum that have transmission below a given threshold. This is not only sensitive to the sources at play, but its values in a standard reionization history and a quasar-dominated scenario diverge at low redshift, rendering it a promising tool to observationally test these models. Finally, we show that the hydrogen-to-helium column density ratio is also sensitive to the sources. In fact, the asymptotic value it reaches at low redshift is different for the standard and quasar-only reionization histories.

Applying the proposed test to observational data requires a careful investigation of possible degeneracies with other physical parameters and, chiefly, an exploration of the predictions from intermediate models. In particular, accurate numerical simulations of reionization histories with a boosted, but not dominant, quasar contribution are needed to properly interpret the data. A different research path is related to a key assumption typically made in reionization studies, namely the uniformity of the QSO escape fraction. While this assumption is well-substantiated for bright objects, its physical motivations are less clear for quasars of less extreme luminosity. Finally, a recent study [375] homogenized and re-analyzed available observations of the QSO luminosity function at $0.1 \leq z < 6.5$, providing a consistent view of its evolution through cosmic time. One of its main features is an enhancement of the quasar ionizing emissivity with respect to the standard scenario, in line with the findings of described in Chapter 4. It would therefore be desirable to perform full hydrodynamical and radiative-transfer simulations including this updated quasar luminosity function in order to test its viability and strengthen the results presented here.

Bibliography

- [1] C. Kidd and B. Y. Hayden, *The psychology and neuroscience of curiosity*, *Neuron* **88** (2015) 449 (cit. on p. 1).
- [2] P. Ntelis et al., *Exploring cosmic homogeneity with the BOSS DR12 galaxy sample*, *JCAP* **6**, 019 (2017) 019, arXiv: 1702.02159 (cit. on p. 2).
- [3] P. Sarkar et al., *The scale of homogeneity of the galaxy distribution in SDSS DR6*, *Mon Not R Astron Soc* **399** (2009) L128, arXiv: 0906.3431 (cit. on p. 2).
- [4] J. Yadav et al., *Testing homogeneity on large scales in the Sloan Digital Sky Survey Data Release One*, *Mon Not R Astron Soc* **364** (2005) 601, eprint: astro-ph/0504315 (cit. on p. 2).
- [5] Planck Collaboration et al., *Planck 2015 results. I. Overview of products and scientific results*, *Astron Astrophys* **594**, A1 (2016) A1, arXiv: 1502.01582 (cit. on p. 2).
- [6] T. Clifton, C. Clarkson and P. Bull, *Isotropic Blackbody Cosmic Microwave Background Radiation as Evidence for a Homogeneous Universe*, *Physical Review Letters* **109**, 051303 (2012) 051303, arXiv: 1111.3794 [gr-qc] (cit. on p. 2).
- [7] A. Einstein, “The foundation of the general theory of relativity”, *The Principle of Relativity. Dover Books on Physics. June 1, 1952. 240 pages.* <ISBN>0486600815</ISBN>, p. 109-164, 1952 109 (cit. on p. 3).
- [8] A. Friedmann, *Über die Krümmung des Raumes*, *Zeitschrift für Physik* **10** (1922) 377, ISSN: 0044-3328, URL: <https://doi.org/10.1007/BF01332580> (cit. on pp. 3, 4).
- [9] A. Friedmann, *Über die Möglichkeit einer Welt mit konstanter negativer Krümmung des Raumes*, *Zeitschrift für Physik* **21** (1924) 326, ISSN: 0044-3328, URL: <https://doi.org/10.1007/BF01328280> (cit. on pp. 3, 4).
- [10] G. Lemaître, *Expansion of the universe, A homogeneous universe of constant mass and increasing radius accounting for the radial velocity of extra-galactic nebulae*, *Mon Not R Astron Soc* **91** (1931) 483 (cit. on p. 3).
- [11] H. P. Robertson, *Kinematics and World-Structure*, *Astrophys J* **82** (1935) 284 (cit. on p. 3).
- [12] H. P. Robertson, *Kinematics and World-Structure II.*, *Astrophys J* **83** (1936) 187 (cit. on p. 3).
- [13] H. P. Robertson, *Kinematics and World-Structure III.*, *Astrophys J* **83** (1936) 257 (cit. on p. 3).
- [14] A. G. Walker, *On Milne’s Theory of World-Structure**, *Proceedings of the London Mathematical Society* **s2-42** (1937) 90, eprint: <https://londmathsoc.onlinelibrary.wiley.com/doi/pdf/10.1112/plms/s2-42.1.90>, URL: <https://londmathsoc.onlinelibrary.wiley.com/doi/abs/10.1112/plms/s2-42.1.90> (cit. on p. 3).

- [15] E. Gaztañaga, R. Miquel and E. Sánchez, *First Cosmological Constraints on Dark Energy from the Radial Baryon Acoustic Scale*, Physical Review Letters **103**, 091302 (2009) 091302, arXiv: 0808.1921 (cit. on p. 3).
- [16] M. Vardanyan, R. Trotta and J. Silk, *How flat can you get? A model comparison perspective on the curvature of the Universe*, Mon Not R Astron Soc **397** (2009) 431, arXiv: 0901.3354 [astro-ph.CO] (cit. on p. 3).
- [17] Planck Collaboration et al., *Planck 2018 results. VI. Cosmological parameters*, ArXiv e-prints (2018), arXiv: 1807.06209 (cit. on pp. 3, 6, 7, 63, 72, 82).
- [18] H. Minkowski, *Die Grundgleichungen für die elektromagnetischen Vorgänge in bewegten Körpern*, Nachrichten von der Gesellschaft der Wissenschaften zu Göttingen, Mathematisch-Physikalische Klasse **1908** (1908) 53, URL: <http://eudml.org/doc/58707> (cit. on p. 4).
- [19] S. Weinberg, *Gravitation and Cosmology: Principles and Applications of the General Theory of Relativity*, 1972 688 (cit. on pp. 4, 9).
- [20] Planck Collaboration et al., *Planck 2015 results. XIII. Cosmological parameters*, Astron Astrophys **594**, A13 (2016) A13, arXiv: 1502.01589 (cit. on pp. 5, 6, 12, 18, 64, 87).
- [21] F. Zwicky, *On the Masses of Nebulae and of Clusters of Nebulae*, Astrophys J **86** (1937) 217 (cit. on p. 5).
- [22] V. C. Rubin, W. K. Ford Jr. and N. Thonnard, *Rotational properties of 21 SC galaxies with a large range of luminosities and radii, from NGC 4605 /R = 4kpc/ to UGC 2885 /R = 122 kpc/*, Astrophys J **238** (1980) 471 (cit. on p. 6).
- [23] S. D. M. White et al., *The baryon content of galaxy clusters: a challenge to cosmological orthodoxy*, Nature **366** (1993) 429 (cit. on p. 6).
- [24] G. Bertone, D. Hooper and J. Silk, *Particle dark matter: evidence, candidates and constraints*, Physics Reports **405** (2005) 279, ISSN: 0370-1573, URL: <http://www.sciencedirect.com/science/article/pii/S0370157304003515> (cit. on p. 6).
- [25] G. Squires et al., *The Dark Matter, Gas, and Galaxy Distributions in Abell 2218: A Weak Gravitational Lensing and X-Ray Analysis*, Astrophys J **461** (1996) 572, eprint: astro-ph/9507008 (cit. on p. 6).
- [26] G. Squires et al., *A Weak Gravitational Lensing Analysis of Abell 2390*, Astrophys J **469** (1996) 73, eprint: astro-ph/9602105 (cit. on p. 6).
- [27] G. Squires et al., *Weak Gravitational Lensing and X-Ray Analysis of Abell 2163*, Astrophys J **482** (1997) 648, eprint: astro-ph/9603050 (cit. on p. 6).
- [28] R. Massey, T. Kitching and J. Richard, *The dark matter of gravitational lensing*, Reports on Progress in Physics **73** (2010) 086901, URL: <http://stacks.iop.org/0034-4885/73/i=8/a=086901> (cit. on p. 6).
- [29] S. D. M. White, C. S. Frenk and M. Davis, *Clustering in a neutrino-dominated universe*, Astrophys J Lett **274** (1983) L1 (cit. on p. 6).

-
- [30] A. G. Riess et al., *Observational Evidence from Supernovae for an Accelerating Universe and a Cosmological Constant*, *Astron J* **116** (1998) 1009, eprint: astro-ph/9805201 (cit. on p. 6).
- [31] S. Perlmutter et al., *Measurements of Ω and Λ from 42 High-Redshift Supernovae*, *Astrophys J* **517** (1999) 565, eprint: astro-ph/9812133 (cit. on p. 6).
- [32] S. M. Carroll, *The Cosmological Constant*, *Living Reviews in Relativity* **4** (2001) 1, ISSN: 1433-8351, URL: <https://doi.org/10.12942/lrr-2001-1> (cit. on p. 6).
- [33] J. Solà, *Cosmological constant and vacuum energy: old and new ideas*, *Journal of Physics: Conference Series* **453** (2013) 012015, URL: <http://stacks.iop.org/1742-6596/453/i=1/a=012015> (cit. on p. 6).
- [34] *What is the Big Bang all about?*, http://scienceblogs.com/startswithabang/files/2013/06/AT_7e_Figure_27_01.jpeg, Credits: 2011 Pearson education, Pearson Addison Wesley. Accessed: 2018-08-01 (cit. on p. 7).
- [35] L. Bergström, *Non-baryonic dark matter: observational evidence and detection methods*, *Reports on Progress in Physics* **63** (2000) 793, eprint: hep-ph/0002126 (cit. on p. 6).
- [36] J. Dubinski and R. G. Carlberg, *The structure of cold dark matter halos*, *Astrophys J* **378** (1991) 496 (cit. on p. 6).
- [37] R. A. Flores and J. R. Primack, *Observational and theoretical constraints on singular dark matter halos*, *Astrophys J Lett* **427** (1994) L1, eprint: astro-ph/9402004 (cit. on p. 6).
- [38] R. A. Swaters, B. F. Madore and M. Trewhella, *High-Resolution Rotation Curves of Low Surface Brightness Galaxies*, *Astrophys J Lett* **531** (2000) L107, eprint: astro-ph/0001277 (cit. on p. 6).
- [39] A. Klypin et al., *Resolving the Structure of Cold Dark Matter Halos*, *Astrophys J* **554** (2001) 903, eprint: astro-ph/0006343 (cit. on p. 6).
- [40] J. E. Taylor and J. F. Navarro, *The Phase-Space Density Profiles of Cold Dark Matter Halos*, *Astrophys J* **563** (2001) 483, eprint: astro-ph/0104002 (cit. on p. 6).
- [41] R. Kuzio de Naray, S. S. McGaugh and W. J. G. de Blok, *Mass Models for Low Surface Brightness Galaxies with High-Resolution Optical Velocity Fields*, *Astrophys J* **676** (2008) 920, arXiv: 0712.0860 (cit. on p. 6).
- [42] A. Pontzen and F. Governato, *How supernova feedback turns dark matter cusps into cores*, *Mon Not R Astron Soc* **421** (2012) 3464, arXiv: 1106.0499 (cit. on p. 7).
- [43] E. Garaldi, M. Baldi and L. Moscardini, *Zoomed high-resolution simulations of Multi-coupled Dark Energy: cored galaxy density profiles at high redshift*, *JCAP* **1**, 050 (2016) 050, arXiv: 1511.02239 (cit. on p. 7).
- [44] M. Boylan-Kolchin, J. S. Bullock and M. Kaplinghat, *Too big to fail? The puzzling darkness of massive Milky Way subhaloes*, *Monthly Notices of the Royal Astronomical Society: Letters* **415** (2011) L40, eprint: /oup/backfile/content_public/journal/mnrasl/415/1/10.1111/j.1745-3933.2011.01074.x/2/415-1-140.pdf, URL: <http://dx.doi.org/10.1111/j.1745-3933.2011.01074.x> (cit. on p. 7).

- [45] S. Garrison-Kimmel et al., *Can feedback solve the too-big-to-fail problem?*, Monthly Notices of the Royal Astronomical Society **433** (2013) 3539, eprint: /oup/backfile/content_public/journal/mnras/433/4/10.1093/mnras/stt984/2/stt984.pdf, URL: <http://dx.doi.org/10.1093/mnras/stt984> (cit. on p. 7).
- [46] S. Garrison-Kimmel et al., *Too big to fail in the Local Group*, Monthly Notices of the Royal Astronomical Society **444** (2014) 222, eprint: /oup/backfile/content_public/journal/mnras/444/1/10.1093_mnras_stu1477/1/stu1477.pdf, URL: <http://dx.doi.org/10.1093/mnras/stu1477> (cit. on p. 7).
- [47] A. A. Dutton et al., *NIHAO V: too big does not fail – reconciling the conflict between Λ CDM predictions and the circular velocities of nearby field galaxies*, Monthly Notices of the Royal Astronomical Society: Letters **457** (2016) L74, eprint: /oup/backfile/content_public/journal/mnrasl/457/1/10.1093_mnrasl_slv193/2/slv193.pdf, URL: <http://dx.doi.org/10.1093/mnrasl/slv193> (cit. on p. 7).
- [48] T. Sawala et al., *The APOSTLE simulations: solutions to the Local Group’s cosmic puzzles*, Monthly Notices of the Royal Astronomical Society **457** (2016) 1931, eprint: /oup/backfile/content_public/journal/mnras/457/2/10.1093/mnras/stw145/2/stw145.pdf, URL: <http://dx.doi.org/10.1093/mnras/stw145> (cit. on p. 7).
- [49] H. Hildebrandt et al., *KiDS-450: cosmological parameter constraints from tomographic weak gravitational lensing*, Monthly Notices of the Royal Astronomical Society **465** (2017) 1454, eprint: /oup/backfile/content_public/journal/mnras/465/2/10.1093_mnras_stw2805/4/stw2805.pdf, URL: <http://dx.doi.org/10.1093/mnras/stw2805> (cit. on p. 7).
- [50] M. A. Troxel et al., *Dark Energy Survey Year 1 Results: Cosmological Constraints from Cosmic Shear*, ArXiv e-prints (2017), arXiv: 1708.01538 (cit. on p. 7).
- [51] A. G. Riess et al., *Milky Way Cepheid Standards for Measuring Cosmic Distances and Application to Gaia DR2: Implications for the Hubble Constant*, Astrophys J **861**, 126 (2018) 126, arXiv: 1804.10655 (cit. on p. 7).
- [52] S. S. McGaugh, *The Mass Discrepancy-Acceleration Relation: Disk Mass and the Dark Matter Distribution*, The Astrophysical Journal **609** (2004) 652, URL: <http://stacks.iop.org/0004-637X/609/i=2/a=652> (cit. on pp. 7, 55).
- [53] F. Lelli et al., *One Law to Rule Them All: The Radial Acceleration Relation of Galaxies*, Astrophys J **836**, 152 (2017) 152, arXiv: 1610.08981 (cit. on pp. 7, 28, 55–60).
- [54] A. Di Cintio and F. Lelli, *The mass discrepancy acceleration relation in a Λ CDM context*, Mon Not R Astron Soc **456** (2016) L127 (cit. on pp. 7, 56).
- [55] I. M. Santos-Santos et al., *The distribution of mass components in simulated disc galaxies*, Mon Not R Astron Soc **455** (2016) 476 (cit. on pp. 7, 56).
- [56] B. W. Keller and J. W. Wadsley, *Λ CDM is Consistent with SPARC Radial Acceleration Relation*, Astrophys J Lett **835**, L17 (2017) L17 (cit. on pp. 7, 56, 58, 60).

-
- [57] A. D. Ludlow et al., *Mass-Discrepancy Acceleration Relation: A Natural Outcome of Galaxy Formation in Cold Dark Matter Halos*, Physical Review Letters **118**, 161103 (2017) 161103 (cit. on pp. 7, 56, 58).
- [58] J. F. Navarro et al., *The origin of the mass discrepancy-acceleration relation in Λ CDM*, Mon Not R Astron Soc **471** (2017) 1841 (cit. on pp. 7, 56).
- [59] H. Desmond,
The scatter, residual correlations and curvature of the SPARC baryonic Tully-Fisher relation, Mon Not R Astron Soc **472** (2017) L35, arXiv: 1706.01017 (cit. on pp. 7, 56).
- [60] A. Tenneti et al.,
The radial acceleration relation in disc galaxies in the MassiveBlack-II simulation, Mon Not R Astron Soc **474** (2018) 3125, arXiv: 1703.05287 (cit. on pp. 7, 56).
- [61] P. Bull et al., *Beyond Λ CDM: Problems, solutions, and the road ahead*, Physics of the Dark Universe **12** (2016) 56, arXiv: 1512.05356 (cit. on p. 7).
- [62] A. Joyce et al., *Beyond the cosmological standard model*, Phys Rep **568** (2015) 1, arXiv: 1407.0059 (cit. on p. 7).
- [63] M. Milgrom, *A modification of the Newtonian dynamics as a possible alternative to the hidden mass hypothesis*, Astrophys J **270** (1983) 365 (cit. on pp. 8, 55).
- [64] J. Bekenstein and M. Milgrom,
Does the missing mass problem signal the breakdown of Newtonian gravity?, Astrophys J **286** (1984) 7 (cit. on pp. 8, 9).
- [65] M. Milgrom, *Dynamics with a Nonstandard Inertia-Acceleration Relation: An Alternative to Dark Matter in Galactic Systems*, Annals of Physics **229** (1994) 384, eprint: astro-ph/9303012 (cit. on pp. 8, 55).
- [66] M. Milgrom, *A modification of the Newtonian dynamics - Implications for galaxies*, Astrophys J **270** (1983) 371 (cit. on p. 8).
- [67] R. B. Tully and J. R. Fisher, *A new method of determining distances to galaxies*, Astron Astrophys **54** (1977) 661 (cit. on pp. 8, 40).
- [68] M. A. Walker, *Collisional baryonic dark matter haloes*, Mon Not R Astron Soc **308** (1999) 551, eprint: astro-ph/9807236 (cit. on pp. 8, 40).
- [69] S. S. McGaugh et al., *The Baryonic Tully-Fisher Relation*, Astrophys J Lett **533** (2000) L99, eprint: astro-ph/0003001 (cit. on pp. 8, 40).
- [70] J. Bekenstein, *The modified Newtonian dynamics - MOND and its implications for new physics*, Contemporary Physics **47** (2006) 387, eprint: astro-ph/0701848 (cit. on p. 8).
- [71] N. Hashim et al., *Rotation Curve with MOND and Dark Matter Halo profile for ESO138-G014*, ArXiv e-prints (2014), arXiv: 1407.0379 (cit. on p. 8).
- [72] R. H. Sanders, *Clusters of galaxies with modified Newtonian dynamics*, Mon Not R Astron Soc **342** (2003) 901, eprint: astro-ph/0212293 (cit. on p. 8).

- [73] G. W. Angus, B. Famaey and D. A. Buote, *X-ray group and cluster mass profiles in MOND: unexplained mass on the group scale*, Monthly Notices of the Royal Astronomical Society **387** (2008) 1470, eprint: [/oup/backfile/content_public/journal/mnras/387/4/10.1111/j.1365-2966.2008.13353.x/2/mnras0387-1470.pdf](http://oup/backfile/content_public/journal/mnras/387/4/10.1111/j.1365-2966.2008.13353.x/2/mnras0387-1470.pdf), URL: <http://dx.doi.org/10.1111/j.1365-2966.2008.13353.x> (cit. on p. 8).
- [74] G. W. Angus, B. Famaey and H. S. Zhao, *Can MOND take a bullet? Analytical comparisons of three versions of MOND beyond spherical symmetry*, Mon Not R Astron Soc **371** (2006) 138, eprint: [astro-ph/0606216](http://arxiv.org/abs/astro-ph/0606216) (cit. on p. 9).
- [75] G. W. Angus et al., *On the Proof of Dark Matter, the Law of Gravity, and the Mass of Neutrinos*, Astrophys J Lett **654** (2007) L13, eprint: [astro-ph/0609125](http://arxiv.org/abs/astro-ph/0609125) (cit. on p. 9).
- [76] D. Clowe, S. W. Randall and M. Markevitch, *Catching a bullet: direct evidence for the existence of dark matter*, Nuclear Physics B Proceedings Supplements **173** (2007) 28, eprint: [astro-ph/0611496](http://arxiv.org/abs/astro-ph/0611496) (cit. on p. 9).
- [77] J. D. Bekenstein, *Relativistic gravitation theory for the modified Newtonian dynamics paradigm*, Phys Rev D **70**, 083509 (2004) 083509, eprint: [astro-ph/0403694](http://arxiv.org/abs/astro-ph/0403694) (cit. on p. 9).
- [78] J. D. Bekenstein, *An alternative to the dark matter paradigm: relativistic MOND gravitation*, ArXiv Astrophysics e-prints (2004), eprint: [astro-ph/0412652](http://arxiv.org/abs/astro-ph/0412652) (cit. on p. 9).
- [79] B. P. Abbott et al., *GW170817: Observation of Gravitational Waves from a Binary Neutron Star Inspiral*, Phys. Rev. Lett. **119** (16 2017) 161101, URL: <https://link.aps.org/doi/10.1103/PhysRevLett.119.161101> (cit. on p. 9).
- [80] B. P. Abbott et al., *Gravitational Waves and Gamma-Rays from a Binary Neutron Star Merger: GW170817 and GRB 170817A*, The Astrophysical Journal Letters **848** (2017) L13, URL: <http://stacks.iop.org/2041-8205/848/i=2/a=L13> (cit. on p. 9).
- [81] E. Sagi, *Propagation of gravitational waves in the generalized tensor-vector-scalar theory*, Phys Rev D **81**, 064031 (2010) 064031, arXiv: [1001.1555](https://arxiv.org/abs/1001.1555) [gr-qc] (cit. on p. 9).
- [82] S. Boran et al., *GW170817 falsifies dark matter emulators*, Phys Rev D **97**, 041501 (2018) 041501, arXiv: [1710.06168](https://arxiv.org/abs/1710.06168) [astro-ph.HE] (cit. on p. 9).
- [83] Y. B. Zel'dovich, *Gravitational instability: An approximate theory for large density perturbations.*, Astron Astrophys **5** (1970) 84 (cit. on p. 9).
- [84] J. H. Jeans, *The Stability of a Spherical Nebula*, Philosophical Transactions of the Royal Society of London. Series A, Containing Papers of a Mathematical or Physical Character **199** (1902) 1, ISSN: 02643952, URL: <http://www.jstor.org/stable/90845> (cit. on p. 10).
- [85] R. E. Angulo et al., *Scaling relations for galaxy clusters in the Millennium-XXL simulation*, Mon Not R Astron Soc **426** (2012) 2046, arXiv: [1203.3216](https://arxiv.org/abs/1203.3216) (cit. on p. 11).
- [86] V. Springel, C. S. Frenk and S. D. M. White, *The large-scale structure of the Universe*, Nature **440** (2006) 1137, eprint: [astro-ph/0604561](http://arxiv.org/abs/astro-ph/0604561) (cit. on p. 11).
- [87] C. S. Frenk and S. D. M. White, *Dark matter and cosmic structure*, Annalen der Physik **524** (2012) 507, arXiv: [1210.0544](https://arxiv.org/abs/1210.0544) [astro-ph.CO] (cit. on p. 11).

-
- [88] Planck Collaboration et al.,
Planck 2015 results. XVII. Constraints on primordial non-Gaussianity,
Astron Astrophys **594**, A17 (2016) A17, arXiv: 1502.01592 (cit. on p. 12).
- [89] M. Borzyszkowski,
The large-scale structure of the Universe; environmental effects and relativistic corrections,
PhD thesis: Universität Bonn, 2018 (cit. on p. 12).
- [90] L. Gao, V. Springel and S. D. M. White, *The age dependence of halo clustering*,
Mon Not R Astron Soc **363** (2005) L66, eprint: astro-ph/0506510 (cit. on pp. 12, 29).
- [91] G. Zhu et al., *The Dependence of the Occupation of Galaxies on the Halo Formation Time*,
Astrophys J Lett **639** (2006) L5, eprint: astro-ph/0601120 (cit. on pp. 12, 29).
- [92] R. H. Wechsler et al.,
The Dependence of Halo Clustering on Halo Formation History, Concentration, and Occupation,
Astrophys J **652** (2006) 71, eprint: astro-ph/0512416 (cit. on p. 12).
- [93] P. Bett et al., *The spin and shape of dark matter haloes in the Millennium simulation of a Λ cold dark matter universe*,
Mon Not R Astron Soc **376** (2007) 215, eprint: astro-ph/0608607 (cit. on p. 12).
- [94] Y. P. Jing, Y. Suto and H. J. Mo,
The Dependence of Dark Halo Clustering on Formation Epoch and Concentration Parameter,
Astrophys J **657** (2007) 664, eprint: astro-ph/0610099 (cit. on p. 12).
- [95] R. E. Angulo, C. M. Baugh and C. G. Lacey,
The assembly bias of dark matter haloes to higher orders,
Mon Not R Astron Soc **387** (2008) 921, arXiv: 0712.2280 (cit. on p. 12).
- [96] A. Faltenbacher and S. D. M. White,
Assembly Bias and the Dynamical Structure of Dark Matter Halos, *Astrophys J* **708** (2010) 469,
arXiv: 0909.4302 (cit. on p. 12).
- [97] R. Li et al., *Assembly bias of dwarf-sized dark matter haloes*,
Mon Not R Astron Soc **435** (2013) 3592, arXiv: 1308.4204 (cit. on p. 12).
- [98] M. Borzyszkowski et al.,
ZOMG – I. How the cosmic web inhibits halo growth and generates assembly bias,
Mon Not R Astron Soc **469** (2017) 594, arXiv: 1610.04231 (cit. on pp. 12, 29, 56, 85).
- [99] A. C. Fabian, *Observational Evidence of Active Galactic Nuclei Feedback*,
Ann Rev of Astron and Astrophys **50** (2012) 455, arXiv: 1204.4114 (cit. on p. 13).
- [100] P. A. Oesch et al., *A Remarkably Luminous Galaxy at $z=11.1$ Measured with Hubble Space Telescope Grism Spectroscopy*,
Astrophys J **819**, 129 (2016) 129, arXiv: 1603.00461 (cit. on p. 14).
- [101] N. Y. Gnedin, *Are There Enough Ionizing Photons to Reionize the Universe by $z \approx 6$?*,
Astrophys J Lett **673** (2008) L1, arXiv: 0709.3308 (cit. on p. 14).
- [102] H. Xu et al., *Galaxy Properties and UV Escape Fractions during the Epoch of Reionization: Results from the Renaissance Simulations*,
The Astrophysical Journal **833** (2016) 84,
URL: <http://stacks.iop.org/0004-637X/833/i=1/a=84> (cit. on p. 14).
- [103] E. Bañados et al.,
An 800-million-solar-mass black hole in a significantly neutral Universe at a redshift of 7.5,
Nature **553** (2018) 473, arXiv: 1712.01860 (cit. on p. 14).

- [104] T. Di Matteo et al., *The origin of the most massive black holes at high- z : BlueTides and the next quasar frontier*, *Mon Not R Astron Soc* **467** (2017) 4243, arXiv: 1606.08871 (cit. on pp. 14, 67).
- [105] G. Worseck et al., *The End of Helium Reionization at $z \sim 2.7$ Inferred from Cosmic Variance in HST/COS He II Ly α Absorption Spectra*, *Astrophys J Lett* **733**, L24 (2011) L24, arXiv: 1103.5752 [astro-ph.CO] (cit. on pp. 14, 63).
- [106] M. Compostella, S. Cantalupo and C. Porciani, *AGN-driven helium reionization and the incidence of extended He III regions at redshift $z > 3$* , *Mon Not R Astron Soc* **445** (2014) 4186, arXiv: 1407.1316 (cit. on pp. 14, 64, 65).
- [107] G. Worseck et al., *Early and Extended Helium Reionization over More Than 600 Million Years of Cosmic Time*, *Astrophys J* **825**, 144 (2016) 144, arXiv: 1405.7405 (cit. on pp. 14, 17, 63, 74, 75).
- [108] G. D. Becker et al., *Evidence of patchy hydrogen reionization from an extreme Ly α trough below redshift six*, *Mon Not R Astron Soc* **447** (2015) 3402, arXiv: 1407.4850 (cit. on pp. 14, 63, 74–77).
- [109] S. E. I. Bosman et al., *New constraints on Lyman- α opacity with a sample of 62 quasars at $z > 5.7$* , ArXiv e-prints (2018), arXiv: 1802.08177 (cit. on pp. 14, 63, 75).
- [110] X. Fan, C. L. Carilli and B. Keating, *Observational Constraints on Cosmic Reionization*, *Ann Rev of Astron and Astrophys* **44** (2006) 415, eprint: astro-ph/0602375 (cit. on pp. 15–17).
- [111] J. E. Gunn and B. A. Peterson, *On the Density of Neutral Hydrogen in Intergalactic Space.*, *Astrophys J* **142** (1965) 1633 (cit. on p. 16).
- [112] A. Songaila, *The Evolution of the Intergalactic Medium Transmission to Redshift 6*, *Astron J* **127** (2004) 2598, eprint: astro-ph/0402347 (cit. on p. 17).
- [113] J. Miralda-Escudé, *Reionization of the Intergalactic Medium and the Damping Wing of the Gunn-Peterson Trough*, *Astrophys J* **501** (1998) 15, eprint: astro-ph/9708253 (cit. on p. 16).
- [114] A. Fontana et al., *The Lack of Intense Ly α in Ultradeep Spectra of $z = 7$ Candidates in GOODS-S: Imprint of Reionization?*, *Astrophys J Lett* **725** (2010) L205, arXiv: 1010.2754 (cit. on p. 17).
- [115] D. P. Stark et al., *Keck spectroscopy of faint $3 < z < 7$ Lyman break galaxies - I. New constraints on cosmic reionization from the luminosity and redshift-dependent fraction of Lyman α emission*, *Mon Not R Astron Soc* **408** (2010) 1628, arXiv: 1003.5244 (cit. on p. 17).
- [116] T. Treu et al., *The Changing Ly α Optical Depth in the Range $6 < z < 9$ from the MOSFIRE Spectroscopy of Y-dropouts*, *Astrophys J Lett* **775**, L29 (2013) L29, arXiv: 1308.5985 (cit. on p. 17).
- [117] M. A. Schenker et al., *Line-emitting Galaxies beyond a Redshift of 7: An Improved Method for Estimating the Evolving Neutrality of the Intergalactic Medium*, *Astrophys J* **795**, 20 (2014) 20, arXiv: 1404.4632 (cit. on pp. 17, 71).
- [118] L. Pentericci et al., *New Observations of $z \sim 7$ Galaxies: Evidence for a Patchy Reionization*, *Astrophys J* **793**, 113 (2014) 113, arXiv: 1403.5466 (cit. on pp. 17, 71).

-
- [119] C. A. Mason et al., *The Universe Is Reionizing at $z \sim 7$: Bayesian Inference of the IGM Neutral Fraction Using Ly α Emission from Galaxies*, *Astrophys J* **856**, 2 (2018) 2, arXiv: 1709.05356 (cit. on pp. 17, 63, 71).
- [120] H. J. A. Rottgering et al., *LOFAR - Opening up a new window on the Universe*, *ArXiv Astrophysics e-prints* (2006), eprint: astro-ph/0610596 (cit. on p. 18).
- [121] A. R. Parsons et al., *The Precision Array for Probing the Epoch of Re-ionization: Eight Station Results*, *Astron J* **139** (2010) 1468, arXiv: 0904.2334 (cit. on p. 18).
- [122] S. Tingay et al., “Realisation of a low frequency SKA Precursor: The Murchison Widefield Array”, *Resolving The Sky - Radio Interferometry: Past, Present and Future*, 2012 36, arXiv: 1212.1327 [astro-ph.IM] (cit. on p. 18).
- [123] S. Singh et al., *SARAS 2: a spectral radiometer for probing cosmic dawn and the epoch of reionization through detection of the global 21-cm signal*, *Experimental Astronomy* **45** (2018) 269, arXiv: 1710.01101 [astro-ph.IM] (cit. on p. 18).
- [124] J. D. Bowman et al., *An absorption profile centred at 78 megahertz in the sky-averaged spectrum*, *Nature* **555** (2018) 67 (cit. on p. 18).
- [125] K. Kakiichi et al., *Ly α -emitting galaxies as a probe of reionization: large-scale bubble morphology and small-scale absorbers*, *Mon Not R Astron Soc* **463** (2016) 4019, arXiv: 1510.05647 (cit. on p. 18).
- [126] Planck Collaboration et al., *Planck 2013 results. XVI. Cosmological parameters*, *Astron Astrophys* **571**, A16 (2014) A16, arXiv: 1303.5076 (cit. on pp. 18, 30, 56).
- [127] X. Fan et al., *Constraining the Evolution of the Ionizing Background and the Epoch of Reionization with $z \sim 6$ Quasars. II. A Sample of 19 Quasars*, *Astron J* **132** (2006) 117, eprint: astro-ph/0512082 (cit. on pp. 18, 63, 71, 74).
- [128] I. D. McGreer, A. Mesinger and X. Fan, *The first (nearly) model-independent constraint on the neutral hydrogen fraction at $z \sim 6$* , *Mon Not R Astron Soc* **415** (2011) 3237, arXiv: 1101.3314 (cit. on p. 18).
- [129] T. Totani et al., *Implications for Cosmic Reionization from the Optical Afterglow Spectrum of the Gamma-Ray Burst 050904 at $z = 6.3$* , *Pub Astron Soc Japan* **58** (2006) 485, eprint: astro-ph/0512154 (cit. on pp. 18, 71).
- [130] M. McQuinn et al., *Probing the neutral fraction of the IGM with GRBs during the epoch of reionization*, *Mon Not R Astron Soc* **388** (2008) 1101, arXiv: 0710.1018 (cit. on p. 18).
- [131] J. S. Bolton et al., *How neutral is the intergalactic medium surrounding the redshift $z = 7.085$ quasar ULAS J1120+0641?*, *Mon Not R Astron Soc* **416** (2011) L70, arXiv: 1106.6089 (cit. on p. 18).
- [132] J. Schroeder, A. Mesinger and Z. Haiman, *Evidence of Gunn-Peterson damping wings in high- z quasar spectra: strengthening the case for incomplete reionization at $z \sim 6 - 7$* , *Mon Not R Astron Soc* **428** (2013) 3058, arXiv: 1204.2838 (cit. on pp. 18, 71).
- [133] H. Jensen et al., *On the use of Ly α emitters as probes of reionization*, *Mon Not R Astron Soc* **428** (2013) 1366, arXiv: 1206.4028 (cit. on p. 18).

- [134] M. Dijkstra, A. Mesinger and J. S. B. Wyithe,
The detectability of Ly α emission from galaxies during the epoch of reionization,
Mon Not R Astron Soc **414** (2011) 2139, arXiv: 1101.5160 (cit. on p. 18).
- [135] T. R. Choudhury et al., *Lyman α emitters gone missing: evidence for late reionization?*,
Mon Not R Astron Soc **452** (2015) 261, arXiv: 1412.4790 (cit. on p. 18).
- [136] A. Mesinger et al., *Can the intergalactic medium cause a rapid drop in Ly α emission at $z > 6$?*,
Mon Not R Astron Soc **446** (2015) 566, arXiv: 1406.6373 (cit. on p. 18).
- [137] M. Ouchi et al., *Statistics of 207 Ly α Emitters at a Redshift Near 7: Constraints on Reionization and Galaxy Formation Models*, Astrophys J **723** (2010) 869, arXiv: 1007.2961 (cit. on pp. 18, 71).
- [138] V. Springel, N. Yoshida and S. D. White,
GADGET: A Code for collisionless and gasdynamical cosmological simulations,
New Astron. **6** (2001) 79, arXiv: astro-ph/0003162 [astro-ph] (cit. on p. 19).
- [139] V. Springel, *The cosmological simulation code GADGET-2*,
Mon Not R Astron Soc **364** (2005) 1105, eprint: astro-ph/0505010 (cit. on pp. 19, 21, 32).
- [140] R. Teyssier, *Cosmological hydrodynamics with adaptive mesh refinement. A new high resolution code called RAMSES*, Astron Astrophys **385** (2002) 337, eprint: astro-ph/0111367 (cit. on pp. 19, 65).
- [141] S. Cantalupo and C. Porciani,
RADAMESH: cosmological radiative transfer for Adaptive Mesh Refinement simulations,
Mon Not R Astron Soc **411** (2011) 1678, arXiv: 1009.1625 (cit. on pp. 19, 67).
- [142] R. W. Hockney and J. W. Eastwood, *Computer simulation using particles*, 1988 (cit. on p. 19).
- [143] A. Y. Toukmaji and J. A. Board, *Ewald summation techniques in perspective: a survey*,
Computer Physics Communications **95** (1996) 73, ISSN: 0010-4655,
URL: <http://www.sciencedirect.com/science/article/pii/S0010465596000161>
(cit. on p. 19).
- [144] M. Berger and P. Colella, *Local adaptive mesh refinement for shock hydrodynamics*,
Journal of Computational Physics **82** (1989) 64, ISSN: 0021-9991,
URL: <http://www.sciencedirect.com/science/article/pii/S0021999189900351>
(cit. on p. 20).
- [145] D. E. Knuth, *The Art of Computer Programming, Volume 1 (3rd Ed.): Fundamental Algorithms*,
Addison Wesley Longman Publishing Co., Inc., 1997, ISBN: 0-201-89683-4 (cit. on p. 20).
- [146] G. Benettin and F. Fassò,
From Hamiltonian perturbation theory to symplectic integrators and back,
Applied Numerical Mathematics **29** (1999) 73, Proceedings of the NSF/CBMS Regional
Conference on Numerical Analysis of Hamiltonian Differential Equations, ISSN: 0168-9274,
URL: <http://www.sciencedirect.com/science/article/pii/S0168927498000749>
(cit. on p. 21).
- [147] R. A. Gingold and J. J. Monaghan,
Smoothed particle hydrodynamics - Theory and application to non-spherical stars,
Mon Not R Astron Soc **181** (1977) 375 (cit. on p. 22).
- [148] L. B. Lucy, *A numerical approach to the testing of the fission hypothesis*,
Astron J **82** (1977) 1013 (cit. on p. 22).

-
- [149] J. Amanatides, A. Woo et al., “A fast voxel traversal algorithm for ray tracing”, *Eurographics*, vol. 87, 3, 1987 3 (cit. on p. 23).
- [150] M. Berger and I. Rigoutsos, *An algorithm for point clustering and grid generation*, *IEEE Transactions on Systems, Man, and Cybernetics* **21** (1991) 1278 (cit. on p. 23).
- [151] M. Schmidt, *The Rate of Star Formation.*, *Astrophys J* **129** (1959) 243 (cit. on p. 24).
- [152] J. Robert C. Kennicutt, *The Global Schmidt Law in Star-forming Galaxies*, *The Astrophysical Journal* **498** (1998) 541, URL: <http://stacks.iop.org/0004-637X/498/i=2/a=541> (cit. on p. 24).
- [153] C. Scannapieco et al., *Feedback and metal enrichment in cosmological smoothed particle hydrodynamics simulations - I. A model for chemical enrichment*, *Mon Not R Astron Soc* **364** (2005) 552, eprint: [astro-ph/0505440](https://arxiv.org/abs/astro-ph/0505440) (cit. on p. 24).
- [154] M. Aumer et al., *Towards a more realistic population of bright spiral galaxies in cosmological simulations*, *Mon Not R Astron Soc* **434** (2013) 3142, arXiv: [1304.1559](https://arxiv.org/abs/1304.1559) [[astro-ph.GA](https://arxiv.org/abs/1304.1559)] (cit. on p. 25).
- [155] O. Hahn and T. Abel, *Multi-scale initial conditions for cosmological simulations*, *Mon Not R Astron Soc* **415** (2011) 2101, arXiv: [1103.6031](https://arxiv.org/abs/1103.6031) (cit. on pp. 26, 30).
- [156] E. Romano-Díaz et al., *ZOMG - II. Does the halo assembly history influence central galaxies and gas accretion?*, *Mon Not R Astron Soc* **469** (2017) 1809, arXiv: [1701.02743](https://arxiv.org/abs/1701.02743) (cit. on pp. 27, 30, 56, 85).
- [157] E. Garaldi et al., *ZOMG - III. The effect of halo assembly on the satellite population*, *Mon Not R Astron Soc* **473** (2018) 2234, arXiv: [1707.01108](https://arxiv.org/abs/1707.01108) (cit. on pp. 29, 56).
- [158] B. Moore, N. Katz and G. Lake, *On the Destruction and Overmerging of Dark Halos in Dissipationless N-Body Simulations*, *Astrophys J* **457** (1996) 455, eprint: [astro-ph/9503088](https://arxiv.org/abs/astro-ph/9503088) (cit. on p. 29).
- [159] G. Tormen, A. Diaferio and D. Syer, *Survival of substructure within dark matter haloes*, *Mon Not R Astron Soc* **299** (1998) 728, eprint: [astro-ph/9712222](https://arxiv.org/abs/astro-ph/9712222) (cit. on p. 29).
- [160] A. Klypin et al., *Galaxies in N-Body Simulations: Overcoming the Overmerging Problem*, *Astrophys J* **516** (1999) 530, eprint: [astro-ph/9708191](https://arxiv.org/abs/astro-ph/9708191) (cit. on pp. 29, 38).
- [161] A. Kravtsov, *The Dark Matter Annihilation Signal from Dwarf Galaxies and Subhalos*, *Advances in Astronomy* **2010**, 281913 (2010) 281913, arXiv: [0906.3295](https://arxiv.org/abs/0906.3295) (cit. on p. 29).
- [162] J. S. Bullock, *Notes on the Missing Satellites Problem*, *ArXiv e-prints* (2010), arXiv: [1009.4505](https://arxiv.org/abs/1009.4505) [[astro-ph.CO](https://arxiv.org/abs/1009.4505)] (cit. on p. 29).
- [163] D. H. Weinberg et al., *Cold dark matter: Controversies on small scales*, *Proceedings of the National Academy of Science* **112** (2015) 12249, arXiv: [1306.0913](https://arxiv.org/abs/1306.0913) (cit. on p. 29).
- [164] L. Gao et al., *The statistics of the subhalo abundance of dark matter haloes*, *Mon Not R Astron Soc* **410** (2011) 2309, arXiv: [1006.2882](https://arxiv.org/abs/1006.2882) [[astro-ph.CO](https://arxiv.org/abs/1006.2882)] (cit. on p. 29).
- [165] T. Ishiyama et al., *The Cosmogrid Simulation: Statistical Properties of Small Dark Matter Halos*, *Astrophys J* **767**, 146 (2013) 146, arXiv: [1101.2020](https://arxiv.org/abs/1101.2020) [[astro-ph.CO](https://arxiv.org/abs/1101.2020)] (cit. on p. 29).
- [166] H.-Y. Wu et al., *Rhapsody. II. Subhalo Properties and the Impact of Tidal Stripping From a Statistical Sample of Cluster-size Halos*, *Astrophys J* **767**, 23 (2013) 23, arXiv: [1210.6358](https://arxiv.org/abs/1210.6358) [[astro-ph.CO](https://arxiv.org/abs/1210.6358)] (cit. on p. 29).

- [167] K. Dolag et al., *Substructures in hydrodynamical cluster simulations*, Mon Not R Astron Soc **399** (2009) 497, arXiv: 0808.3401 (cit. on pp. 29, 41).
- [168] T. Okamoto et al., *The properties of satellite galaxies in simulations of galaxy formation*, Mon Not R Astron Soc **406** (2010) 208, arXiv: 0909.0265 (cit. on p. 29).
- [169] E. Romano-Díaz et al., *Dissecting Galaxy Formation. II. Comparing Substructure in Pure Dark Matter and Baryonic Models*, Astrophys J **716** (2010) 1095, arXiv: 1002.4200 (cit. on pp. 29, 38).
- [170] J. A. Schewtschenko and A. V. Macciò, *Comparing galactic satellite properties in hydrodynamical and N-body simulations*, Mon Not R Astron Soc **413** (2011) 878, arXiv: 1012.0311 (cit. on pp. 29, 40).
- [171] A. Di Cintio et al., *Size matters: the non-universal density profile of subhaloes in SPH simulations and implications for the Milky Way's dSphs*, Mon Not R Astron Soc **431** (2013) 1220, arXiv: 1204.0515 (cit. on p. 29).
- [172] L. Wang et al., *NIHAO VII: Predictions for the galactic baryon budget in dwarf to Milky Way mass haloes*, ArXiv e-prints (2016), arXiv: 1601.00967 (cit. on p. 29).
- [173] K. T. E. Chua et al., *Subhalo Demographics in the Illustris Simulation: Effects of Baryons and Halo-to-Halo Variation*, ArXiv e-prints (2016), arXiv: 1611.07991 (cit. on p. 29).
- [174] G. Harker et al., *A marked correlation function analysis of halo formation times in the Millennium Simulation*, Mon Not R Astron Soc **367** (2006) 1039, eprint: astro-ph/0510488 (cit. on p. 29).
- [175] L. Gao and S. D. M. White, *Assembly bias in the clustering of dark matter haloes*, Mon Not R Astron Soc **377** (2007) L5, eprint: astro-ph/0611921 (cit. on p. 29).
- [176] N. Dalal et al., *Halo Assembly Bias in Hierarchical Structure Formation*, Astrophys J **687**, 12-21 (2008) 12, arXiv: 0803.3453 (cit. on pp. 29, 85).
- [177] O. Hahn et al., *Tidal effects and the environment dependence of halo assembly*, Mon Not R Astron Soc **398** (2009) 1742, arXiv: 0803.4211 (cit. on pp. 29, 85).
- [178] M. R. Lovell et al., *The link between galactic satellite orbits and subhalo accretion*, Mon Not R Astron Soc **413** (2011) 3013, arXiv: 1008.0484 (cit. on pp. 30, 49).
- [179] R. E. González and N. D. Padilla, *Subhalo Accretion through Filaments*, Astrophys J **829**, 58 (2016) 58, arXiv: 1601.06434 (cit. on p. 30).
- [180] N. I. Libeskind et al., *The distribution of satellite galaxies: the great pancake*, Mon Not R Astron Soc **363** (2005) 146, eprint: astro-ph/0503400 (cit. on pp. 30, 51).
- [181] N. I. Libeskind et al., *Planes of satellite galaxies and the cosmic web*, Mon Not R Astron Soc **452** (2015) 1052, arXiv: 1503.05915 (cit. on p. 30).
- [182] S. H. Ahmed, A. M. Brooks and C. R. Christensen, *The role of baryons in creating statistically significant planes of satellites around Milky Way-mass galaxies*, Mon Not R Astron Soc **466** (2017) 3119, arXiv: 1610.03077 (cit. on p. 30).
- [183] T. Buck, A. V. Macciò and A. A. Dutton, *Evidence for Early Filamentary Accretion from the Andromeda Galaxy's Thin Plane of Satellites*, Astrophys J **809**, 49 (2015) 49, arXiv: 1504.05193 (cit. on p. 30).

-
- [184] S. Shao et al., *Alignments between galaxies, satellite systems and haloes*, Mon Not R Astron Soc **460** (2016) 3772, arXiv: 1605.01728 (cit. on p. 30).
- [185] N. I. Libeskind et al., *The universal nature of subhalo accretion*, Mon Not R Astron Soc **443** (2014) 1274, arXiv: 1407.0394 (cit. on p. 30).
- [186] J. F. Navarro, C. S. Frenk and S. D. M. White, *A Universal Density Profile from Hierarchical Clustering*, Astrophys J **490** (1997) 493, eprint: astro-ph/9611107 (cit. on p. 32).
- [187] M. Borzyszkowski, A. D. Ludlow and C. Porciani, *The formation of cold dark matter haloes - II. Collapse time and tides*, Mon Not R Astron Soc **445** (2014) 4124, arXiv: 1405.7367 (cit. on p. 30).
- [188] V. Springel and L. Hernquist, *Cosmological smoothed particle hydrodynamics simulations: a hybrid multiphase model for star formation*, Mon Not R Astron Soc **339** (2003) 289, eprint: astro-ph/0206393 (cit. on p. 32).
- [189] F. Haardt and P. Madau, “Modelling the UV/X-ray cosmic background with CUBA”, *Clusters of Galaxies and the High Redshift Universe Observed in X-rays*, ed. by D. M. Neumann and J. T. V. Tran, 2001, eprint: astro-ph/0106018 (cit. on p. 32).
- [190] S. P. D. Gill, A. Knebe and B. K. Gibson, *The evolution of substructure - I. A new identification method*, Mon Not R Astron Soc **351** (2004) 399, eprint: astro-ph/0404258 (cit. on pp. 32, 56).
- [191] S. R. Knollmann and A. Knebe, *AHF: Amiga’s Halo Finder*, Astrophys J Suppl Ser **182** (2009) 608, arXiv: 0904.3662 (cit. on pp. 32, 56).
- [192] C. Scannapieco et al., *The Aquila comparison project: the effects of feedback and numerical methods on simulations of galaxy formation*, Mon Not R Astron Soc **423** (2012) 1726, arXiv: 1112.0315 (cit. on p. 32).
- [193] B. Diemer and A. V. Kravtsov, *Dependence of the Outer Density Profiles of Halos on Their Mass Accretion Rate*, Astrophys J **789**, 1 (2014) 1, arXiv: 1401.1216 (cit. on pp. 32, 57).
- [194] S. Adhikari, N. Dalal and R. T. Chamberlain, *Splashback in accreting dark matter halos*, JCAP **11**, 019 (2014) 019, arXiv: 1409.4482 (cit. on pp. 33, 37).
- [195] S. More, B. Diemer and A. V. Kravtsov, *The Splashback Radius as a Physical Halo Boundary and the Growth of Halo Mass*, Astrophys J **810**, 36 (2015) 36, arXiv: 1504.05591 (cit. on pp. 33, 34, 37).
- [196] J. Binney and S. Tremaine, *Galactic Dynamics: Second Edition*, Princeton University Press, 2008 (cit. on p. 33).
- [197] H. Mo, F. C. van den Bosch and S. White, *Galaxy Formation and Evolution*, 2010 (cit. on p. 33).
- [198] L. Mayer, *Cosmological simulations of the Milky Way*, Highlights of Astronomy **15** (2010) 193 (cit. on p. 33).
- [199] A. G. Doroshkevich, Y. B. Zel’dovich and I. D. Novikov, *The Origin of Galaxies in an Expanding Universe.*, Soviet Astron **11** (1967) 233 (cit. on p. 36).
- [200] M. J. Rees, *Lyman absorption lines in quasar spectra - Evidence for gravitationally-confined gas in dark minihaloes*, Mon Not R Astron Soc **218** (1986) 25P (cit. on p. 36).

- [201] N. Y. Gnedin, *Effect of Reionization on Structure Formation in the Universe*, *Astrophys J* **542** (2000) 535, eprint: astro-ph/0002151 (cit. on p. 36).
- [202] T. Okamoto, L. Gao and T. Theuns, *Mass loss of galaxies due to an ultraviolet background*, *Mon Not R Astron Soc* **390** (2008) 920, arXiv: 0806.0378 (cit. on p. 36).
- [203] A. Benítez-Llambay et al., *Mergers and the outside-in formation of dwarf spheroidals*, *Mon Not R Astron Soc* **456** (2016) 1185, arXiv: 1511.06188 (cit. on p. 36).
- [204] A. Helmi and S. D. M. White, *Building up the stellar halo of the Galaxy*, *Mon Not R Astron Soc* **307** (1999) 495, eprint: astro-ph/9901102 (cit. on p. 36).
- [205] R. Mohayaee and S. F. Shandarin, *Gravitational cooling and density profile near caustics in collisionless dark matter haloes*, *Mon Not R Astron Soc* **366** (2006) 1217, eprint: astro-ph/0503163 (cit. on p. 36).
- [206] A. D. Ludlow et al., *The Unorthodox Orbits of Substructure Halos*, *Astrophys J* **692** (2009) 931, arXiv: 0801.1127 (cit. on p. 37).
- [207] P. Mansfield, A. V. Kravtsov and B. Diemer, *Splashback Shells of Cold Dark Matter Halos*, ArXiv e-prints (2016), arXiv: 1612.01531 (cit. on p. 37).
- [208] B. Diemer, *The Splashback Radius of Halos from Particle Dynamics. I. The SPARTA Algorithm*, *Astrophys J Suppl Ser* **231**, 5 (2017) 5, arXiv: 1703.09712 (cit. on p. 37).
- [209] S. More et al., *Detection of the Splashback Radius and Halo Assembly Bias of Massive Galaxy Clusters*, *Astrophys J* **825**, 39 (2016) 39, arXiv: 1601.06063 (cit. on p. 37).
- [210] E. Baxter et al., *The Halo Boundary of Galaxy Clusters in the SDSS*, *Astrophys J* **841**, 18 (2017) 18, arXiv: 1702.01722 (cit. on p. 37).
- [211] M. Hirschmann et al., *Galaxy formation in semi-analytic models and cosmological hydrodynamic zoom simulations*, *Mon Not R Astron Soc* **419** (2012) 3200, arXiv: 1104.1626 (cit. on p. 38).
- [212] S. Garrison-Kimmel et al., *Not so lumpy after all: modeling the depletion of dark matter subhalos by Milky Way-like galaxies*, ArXiv e-prints (2017), arXiv: 1701.03792 (cit. on pp. 38, 54).
- [213] B. Moore et al., *Dark Matter Substructure within Galactic Halos*, *Astrophys J Lett* **524** (1999) L19, eprint: astro-ph/9907411 (cit. on p. 38).
- [214] S. Ghigna et al., *Density Profiles and Substructure of Dark Matter Halos: Converging Results at Ultra-High Numerical Resolution*, *Astrophys J* **544** (2000) 616, eprint: astro-ph/9910166 (cit. on p. 38).
- [215] V. Springel et al., *The Aquarius Project: the subhaloes of galactic haloes*, *Mon Not R Astron Soc* **391** (2008) 1685, arXiv: 0809.0898 (cit. on pp. 38, 39).
- [216] L. Gao et al., *The Phoenix Project: the dark side of rich Galaxy clusters*, *Mon Not R Astron Soc* **425** (2012) 2169, arXiv: 1201.1940 [astro-ph.CO] (cit. on pp. 38, 40).
- [217] M. Cautun et al., *Subhalo statistics of galactic haloes: beyond the resolution limit*, *Mon Not R Astron Soc* **445** (2014) 1820, arXiv: 1405.7700 (cit. on p. 38).

-
- [218] W. A. Hellwing et al.,
The Copernicus Complexio: a high-resolution view of the small-scale Universe,
Mon Not R Astron Soc **457** (2016) 3492, arXiv: 1505.06436 (cit. on p. 38).
- [219] T. Sawala et al., *The abundance of (not just) dark matter haloes*,
Mon Not R Astron Soc **431** (2013) 1366, arXiv: 1206.6495 [astro-ph.CO] (cit. on p. 38).
- [220] T. Sawala et al., *Shaken and stirred: the Milky Way's dark substructures*,
Mon Not R Astron Soc **467** (2017) 4383, arXiv: 1609.01718 (cit. on p. 38).
- [221] S. Vegetti et al., *Inference of the cold dark matter substructure mass function at $z = 0.2$ using strong gravitational lenses*, Mon Not R Astron Soc **442** (2014) 2017, arXiv: 1405.3666 (cit. on p. 38).
- [222] N. Okabe et al., *Subaru Weak-lensing Survey of Dark Matter Subhalos in the Coma Cluster: Subhalo Mass Function and Statistical Properties*, Astrophys J **784**, 90 (2014) 90, arXiv: 1304.2399 (cit. on p. 38).
- [223] C. Giocoli, G. Tormen and F. C. van den Bosch,
The population of dark matter subhaloes: mass functions and average mass-loss rates,
Mon Not R Astron Soc **386** (2008) 2135, arXiv: 0712.1563 (cit. on p. 39).
- [224] J. Han et al., *A unified model for the spatial and mass distribution of subhaloes*,
Mon Not R Astron Soc **457** (2016) 1208, arXiv: 1509.02175 (cit. on pp. 39, 40).
- [225] D. Nagai and A. V. Kravtsov,
The Radial Distribution of Galaxies in Λ Cold Dark Matter Clusters,
Astrophys J **618** (2005) 557, eprint: astro-ph/0408273 (cit. on p. 40).
- [226] N. I. Libeskind et al., *Satellite systems around galaxies in hydrodynamic simulations*,
Mon Not R Astron Soc **374** (2007) 16, eprint: astro-ph/0607237 (cit. on p. 40).
- [227] Q. Zhu et al.,
Baryonic impact on the dark matter distribution in Milky Way-sized galaxies and their satellites,
Mon Not R Astron Soc **458** (2016) 1559, arXiv: 1506.05537 (cit. on p. 40).
- [228] S. S. McGaugh,
The Baryonic Tully-Fisher Relation of Gas-rich Galaxies as a Test of Λ CDM and MOND,
Astron J **143**, 40 (2012) 40, arXiv: 1107.2934 (cit. on pp. 40, 41).
- [229] J. Wolf et al., *Accurate masses for dispersion-supported galaxies*,
Mon Not R Astron Soc **406** (2010) 1220, arXiv: 0908.2995 (cit. on pp. 40, 42, 56).
- [230] O. H. Parry et al., *The baryons in the Milky Way satellites*,
Mon Not R Astron Soc **419** (2012) 3304, arXiv: 1105.3474 (cit. on pp. 40, 42).
- [231] A. A. Dutton, *The baryonic Tully-Fisher relation and galactic outflows*,
Mon Not R Astron Soc **424** (2012) 3123, arXiv: 1206.1855 (cit. on p. 40).
- [232] F. Lelli, S. S. McGaugh and J. M. Schombert,
The Small Scatter of the Baryonic Tully-Fisher Relation, Astrophys J Lett **816**, L14 (2016) L14, arXiv: 1512.04543 (cit. on p. 40).
- [233] L. V. Sales et al., *The low-mass end of the baryonic Tully-Fisher relation*,
Mon Not R Astron Soc **464** (2017) 2419, arXiv: 1602.02155 (cit. on p. 40).
- [234] J. G. Sorce and Q. Guo, *The baryonic Tully-Fisher relation cares about the galaxy sample*,
Mon Not R Astron Soc **458** (2016) 2667 (cit. on p. 40).

- [235] G. Tormen, L. Moscardini and N. Yoshida,
Properties of cluster satellites in hydrodynamical simulations,
Mon Not R Astron Soc **350** (2004) 1397, eprint: astro-ph/0304375 (cit. on p. 41).
- [236] L. Liu et al., *How Common are the Magellanic Clouds?*, Astrophys J **733**, 62 (2011) 62,
arXiv: 1011.2255 (cit. on p. 41).
- [237] J. Grcevich and M. E. Putman,
HI in Local Group Dwarf Galaxies and Stripping by the Galactic Halo,
Astrophys J **696**, 385-395 (2009) 385, arXiv: 0901.4975 (cit. on p. 41).
- [238] A. W. McConnachie,
The Observed Properties of Dwarf Galaxies in and around the Local Group,
Astron J **144**, 4 (2012) 4, arXiv: 1204.1562 (cit. on p. 41).
- [239] K. Spekkens et al., *The Dearth of Neutral Hydrogen in Galactic Dwarf Spheroidal Galaxies*,
Astrophys J Lett **795**, L5 (2014) L5, arXiv: 1410.0028 (cit. on p. 41).
- [240] T. Westmeier et al.,
On the neutral gas content of nine new Milky Way satellite galaxy candidates,
Mon Not R Astron Soc **453** (2015) 338, arXiv: 1507.03661 (cit. on p. 41).
- [241] S. M. Weinmann et al., *Properties of galaxy groups in the Sloan Digital Sky Survey - II. Active galactic nucleus feedback and star formation truncation*,
Mon Not R Astron Soc **372** (2006) 1161, eprint: astro-ph/0606458 (cit. on pp. 41, 42, 54).
- [242] G. Kauffmann et al., *A re-examination of galactic conformity and a comparison with semi-analytic models of galaxy formation*, Mon Not R Astron Soc **430** (2013) 1447,
arXiv: 1209.3306 (cit. on p. 41).
- [243] C. Knobel et al., *Quenching of Star Formation in Sloan Digital Sky Survey Groups: Centrals, Satellites, and Galactic Conformity*, Astrophys J **800**, 24 (2015) 24, arXiv: 1408.2553
(cit. on p. 41).
- [244] A. Paranjape et al.,
Correlating galaxy colour and halo concentration: a tunable halo model of galactic conformity,
Mon Not R Astron Soc **454** (2015) 3030, arXiv: 1503.08212 (cit. on p. 41).
- [245] M. Cautun and C. S. Frenk, *The tangential velocity excess of the Milky Way satellites*,
ArXiv e-prints (2016), arXiv: 1612.01529 (cit. on pp. 46–48, 54).
- [246] M. I. Wilkinson and N. W. Evans, *The present and future mass of the Milky Way halo*,
Mon Not R Astron Soc **310** (1999) 645, eprint: astro-ph/9906197 (cit. on p. 46).
- [247] N. Kallivayalil et al., *A Hubble Astrometry Initiative: Laying the Foundation for the Next-Generation Proper-Motion Survey of the Local Group*, ArXiv e-prints (2015),
arXiv: 1503.01785 (cit. on p. 46).
- [248] G. Gilmore and N. Reid, *New light on faint stars. III - Galactic structure towards the South Pole and the Galactic thick disc*, Mon Not R Astron Soc **202** (1983) 1025 (cit. on p. 48).
- [249] J. J. Dalcanton and R. A. Bernstein, *A Structural and Dynamical Study of Late-Type, Edge-on Galaxies. II. Vertical Color Gradients and the Detection of Ubiquitous Thick Disks*,
Astron J **124** (2002) 1328, eprint: astro-ph/0207221 (cit. on p. 48).
- [250] R. Wojtak and G. A. Mamon,
Physical properties underlying observed kinematics of satellite galaxies,
Mon Not R Astron Soc **428** (2013) 2407, arXiv: 1207.1647 [astro-ph.CO] (cit. on p. 48).

-
- [251] W. E. Kunkel and S. Demers, “The Magellanic Plane”, *The Galaxy and the Local Group*, ed. by R. J. Dickens et al., vol. 182, Royal Greenwich Observatory Bulletins, 1976 241 (cit. on p. 48).
- [252] D. Lynden-Bell, *Dwarf galaxies and globular clusters in high velocity hydrogen streams*, *Mon Not R Astron Soc* **174** (1976) 695 (cit. on p. 48).
- [253] P. Kroupa, C. Theis and C. M. Boily, *The great disk of Milky-Way satellites and cosmological sub-structures*, *Astron Astrophys* **431** (2005) 517, eprint: astro-ph/0410421 (cit. on p. 49).
- [254] R. A. Ibata et al., *A vast, thin plane of corotating dwarf galaxies orbiting the Andromeda galaxy*, *Nature* **493** (2013) 62, arXiv: 1301.0446 [astro-ph.CO] (cit. on p. 49).
- [255] K. Chiboucas et al., *Confirmation of Faint Dwarf Galaxies in the M81 Group*, *Astron J* **146**, 126 (2013) 126, arXiv: 1309.4130 (cit. on p. 49).
- [256] R. B. Tully et al., *Two Planes of Satellites in the Centaurus A Group*, *Astrophys J Lett* **802**, L25 (2015) L25, arXiv: 1503.05599 (cit. on p. 49).
- [257] M. Bellazzini et al., *Dwarfs walking in a row. The filamentary nature of the NGC 3109 association*, *Astron Astrophys* **559**, L11 (2013) L11, arXiv: 1310.6365 (cit. on p. 49).
- [258] Y.-S. Li and A. Helmi, *Infall of substructures on to a Milky Way-like dark halo*, *Mon Not R Astron Soc* **385** (2008) 1365, arXiv: 0711.2429 (cit. on p. 49).
- [259] E. D’Onghia and G. Lake, *Small Dwarf Galaxies within Larger Dwarfs: Why Some Are Luminous while Most Go Dark*, *Astrophys J Lett* **686**, L61 (2008) L61, arXiv: 0802.0001 (cit. on p. 49).
- [260] N. I. Libeskind et al., *The preferred direction of infalling satellite galaxies in the Local Group*, *Mon Not R Astron Soc* **411** (2011) 1525, arXiv: 1010.1531 (cit. on p. 49).
- [261] M. S. Pawlowski et al., *Filamentary accretion cannot explain the orbital poles of the Milky Way satellites*, *Mon Not R Astron Soc* **424** (2012) 80, arXiv: 1204.6039 (cit. on p. 49).
- [262] F. Hammer et al., *The vast thin plane of M31 corotating dwarfs: an additional fossil signature of the M31 merger and of its considerable impact in the whole Local Group*, *Mon Not R Astron Soc* **431** (2013) 3543, arXiv: 1303.1817 (cit. on p. 49).
- [263] M. Maji et al., *Is there a disk of satellites around the Milky Way?*, ArXiv e-prints (2017), arXiv: 1702.00485 (cit. on p. 51).
- [264] M. Maji et al., *The nature of disk of satellites around Milky Way-like galaxies*, ArXiv e-prints (2017), arXiv: 1702.00497 (cit. on p. 51).
- [265] M. S. Pawlowski et al., *A comment on “Is There a Disk of Satellites Around the Milky Way?” and “The Nature of Disks of Satellites Around Milky Way-Like Galaxies”*, ArXiv e-prints (2017), arXiv: 1702.06143 (cit. on p. 51).
- [266] M. Metz, P. Kroupa and N. I. Libeskind, *The Orbital Poles of Milky Way Satellite Galaxies: A Rotationally Supported Disk of Satellites*, *Astrophys J* **680**, 287-294 (2008) 287, arXiv: 0802.3899 (cit. on p. 51).

- [267] M. Ester et al.,
“A density-based algorithm for discovering clusters in large spatial databases with noise.”, *Kdd*,
vol. 96, 34, 1996 226 (cit. on p. 52).
- [268] E. Garaldi et al., *Radial Acceleration Relation of Λ CDM Satellite Galaxies*,
Physical Review Letters **120**, 261301 (2018) 261301, arXiv: 1712.04448 (cit. on p. 55).
- [269] S. M. Faber and R. E. Jackson,
Velocity dispersions and mass-to-light ratios for elliptical galaxies, *Astrophys J* **204** (1976) 668
(cit. on p. 55).
- [270] R. B. Tully and J. R. Fisher, *A new method of determining distances to galaxies*,
Astron Astrophys **54** (1977) 661 (cit. on p. 55).
- [271] R. Sancisi, “The visible matter – dark matter coupling”, *Dark Matter in Galaxies*,
ed. by S. Ryder et al., vol. 220, IAU Symposium, 2004 233 (cit. on p. 55).
- [272] J. Bekenstein and M. Milgrom,
Does the missing mass problem signal the breakdown of Newtonian gravity?,
Astrophys J **286** (1984) 7 (cit. on p. 55).
- [273] S. S. McGaugh, F. Lelli and J. M. Schombert,
Radial Acceleration Relation in Rotationally Supported Galaxies,
Physical Review Letters **117**, 201101 (2016) 201101 (cit. on pp. 55, 59).
- [274] A. W. McConnachie and P. Côté, *Revisiting the Influence of Unidentified Binaries on Velocity
Dispersion Measurements in Ultra-faint Stellar Systems*, *Astrophys J Lett* **722** (2010) L209
(cit. on p. 56).
- [275] S. S. McGaugh and J. Wolf,
Local Group Dwarf Spheroidals: Correlated Deviations from the Baryonic Tully-Fisher Relation,
Astrophys J **722** (2010) 248 (cit. on p. 56).
- [276] J. Peñarrubia, J. F. Navarro and A. W. McConnachie,
The Tidal Evolution of Local Group Dwarf Spheroidals, *Astrophys J* **673**, 226-240 (2008) 226
(cit. on p. 60).
- [277] J. Peñarrubia et al., *The Signature of Galactic Tides in Local Group Dwarf Spheroidals*,
Astrophys J **698** (2009) 222 (cit. on p. 60).
- [278] N. I. Libeskind et al.,
Constrained simulations of the Local Group: on the radial distribution of substructures,
Mon Not R Astron Soc **401** (2010) 1889 (cit. on p. 60).
- [279] E. Romano-Díaz et al., *Dissecting Galaxy Formation. II. Comparing Substructure in Pure Dark
Matter and Baryonic Models*, *Astrophys J* **716** (2010) 1095 (cit. on p. 60).
- [280] A. Fattahi et al., *Tidal stripping and the structure of dwarf galaxies in the Local Group*,
ArXiv e-prints (2017), arXiv: 1707.03898 (cit. on p. 60).
- [281] E. Garaldi, M. Compostella and C. Porciani,
The Goldilocks problem of the quasar contribution to reionization, ArXiv e-prints (2018),
arXiv: 1809.10144 (cit. on p. 63).
- [282] S. Zaroubi, “The Epoch of Reionization”, *The First Galaxies*,
ed. by T. Wiklind, B. Mobasher and V. Bromm, vol. 396,
Astrophysics and Space Science Library, 2013 45, arXiv: 1206.0267 (cit. on p. 63).

-
- [283] M. McQuinn, *The Evolution of the Intergalactic Medium*, *Ann Rev of Astron and Astrophys* **54** (2016) 313, arXiv: 1512.00086 (cit. on pp. 63, 73).
- [284] G. D. Becker et al., *A refined measurement of the mean transmitted flux in the Ly α forest over $2 < z < 5$ using composite quasar spectra*, *Mon Not R Astron Soc* **430** (2013) 2067, arXiv: 1208.2584 (cit. on pp. 63, 74).
- [285] K. Ota et al., *Ly α Emitters at $z = 7$ in the Subaru/XMM-Newton Deep Survey Field: Photometric Candidates and Luminosity Functions*, *Astrophys J* **722** (2010) 803, arXiv: 1008.4842 (cit. on p. 63).
- [286] L. Pentericci et al., *Spectroscopic Confirmation of $z \sim 7$ Lyman Break Galaxies: Probing the Earliest Galaxies and the Epoch of Reionization*, *Astrophys J* **743**, 132 (2011) 132, arXiv: 1107.1376 (cit. on p. 63).
- [287] T. Shibuya et al., *The First Systematic Survey for Ly α Emitters at $z = 7.3$ with Red-sensitive Subaru/Suprime-Cam*, *Astrophys J* **752**, 114 (2012) 114, arXiv: 1112.3997 (cit. on p. 63).
- [288] H. Furusawa et al., *A New Constraint on the Ly α Fraction of UV Very Bright Galaxies at Redshift 7*, *Astrophys J* **822**, 46 (2016) 46, arXiv: 1604.02214 (cit. on p. 63).
- [289] R. Sadoun, Z. Zheng and J. Miralda-Escudé, *On the Decreasing Fraction of Strong Ly α Emitters around $z \sim 6 - 7$* , *Astrophys J* **839**, 44 (2017) 44, arXiv: 1607.08247 (cit. on p. 63).
- [290] Planck Collaboration et al., *Planck intermediate results. XLVI. Reduction of large-scale systematic effects in HFI polarization maps and estimation of the reionization optical depth*, *Astron Astrophys* **596**, A107 (2016) A107, arXiv: 1605.02985 (cit. on p. 63).
- [291] J. M. Shull et al., *HST/COS Observations of the Quasar HE 2347-4342: Probing the Epoch of He II Patchy Reionization at Redshifts $z = 2.4-2.9$* , *Astrophys J* **722** (2010) 1312 (cit. on pp. 63, 81).
- [292] S. R. Furlanetto and K. L. Dixon, *Large-Scale Fluctuations in the He II Ly α Forest and He II Reionization*, *Astrophys J* **714** (2010) 355, arXiv: 0910.5246 (cit. on p. 63).
- [293] G. Worseck et al., *The Evolution of the HeII-Ionizing Background at Redshifts $2.3 < z < 3.8$ Inferred from a Statistical Sample of 24 HST/COS HeII Ly α Absorption Spectra*, *ArXiv e-prints* (2018), arXiv: 1808.05247 (cit. on pp. 63, 74, 75).
- [294] J. Chardin, E. Puchwein and M. G. Haehnelt, *Large-scale opacity fluctuations in the Ly α forest: evidence for QSOs dominating the ionizing UV background at $z \sim 5.5 - 6?$* , *Mon Not R Astron Soc* **465** (2017) 3429, arXiv: 1606.08231 (cit. on pp. 63, 64, 77, 86).
- [295] R. Barnett et al., *Observations of the Lyman series forest towards the redshift 7.1 quasar ULAS J1120+0641*, *Astron Astrophys* **601**, A16 (2017) A16, arXiv: 1702.03687 (cit. on p. 63).
- [296] A.-C. Eilers, F. B. Davies and J. F. Hennawi, *The Opacity of the Intergalactic Medium Measured Along Quasar Sightlines at $z \sim 6$* , *ArXiv e-prints* (2018), arXiv: 1807.04229 (cit. on pp. 63, 75).

- [297] N. Y. Gnedin, G. D. Becker and X. Fan, *Cosmic Reionization on Computers: Properties of the Post-reionization IGM*, *Astrophys J* **841**, 26 (2017) 26, arXiv: 1605.03183 (cit. on pp. 63, 77).
- [298] A. D’Aloisio, M. McQuinn and H. Trac, *Large Opacity Variations in the High-redshift Ly α Forest: The Signature of Relic Temperature Fluctuations from Patchy Reionization*, *Astrophys J Lett* **813**, L38 (2015) L38, arXiv: 1509.02523 (cit. on p. 64).
- [299] F. B. Davies and S. R. Furlanetto, *Large fluctuations in the hydrogen-ionizing background and mean free path following the epoch of reionization*, *Mon Not R Astron Soc* **460** (2016) 1328, arXiv: 1509.07131 (cit. on p. 64).
- [300] G. D. Becker et al., *Evidence for Large-Scale Fluctuations in the Metagalactic Ionizing Background Near Redshift Six*, ArXiv e-prints (2018), arXiv: 1803.08932 (cit. on p. 64).
- [301] E. Giallongo et al., *Faint AGNs at $z > 4$ in the CANDELS GOODS-S field: looking for contributors to the reionization of the Universe*, *Astron Astrophys* **578**, A83 (2015) A83, arXiv: 1502.02562 (cit. on pp. 64–66, 82, 86).
- [302] F. Ricci et al., *Constraining the UV emissivity of AGN throughout cosmic time via X-ray surveys*, *Mon Not R Astron Soc* **465** (2017) 1915, arXiv: 1610.01638 (cit. on p. 64).
- [303] S. Parsa, J. S. Dunlop and R. J. McLure, *No evidence for a significant AGN contribution to cosmic hydrogen reionization*, *Mon Not R Astron Soc* **474** (2018) 2904, arXiv: 1704.07750 (cit. on p. 64).
- [304] P. Madau and F. Haardt, *Cosmic Reionization after Planck: Could Quasars Do It All?*, *Astrophys J Lett* **813**, L8 (2015) L8, arXiv: 1507.07678 (cit. on p. 64).
- [305] A. D’Aloisio et al., *On the contribution of active galactic nuclei to the high-redshift metagalactic ionizing background*, *Mon Not R Astron Soc* **468** (2017) 4691, arXiv: 1607.06467 (cit. on pp. 64, 73, 86).
- [306] P. R. Upton Sanderbeck, A. D’Aloisio and M. J. McQuinn, *Models of the thermal evolution of the intergalactic medium after reionization*, *Mon Not R Astron Soc* **460** (2016) 1885, arXiv: 1511.05992 (cit. on pp. 64, 73, 86).
- [307] M. Onoue et al., *Minor Contribution of Quasars to Ionizing Photon Budget at $z \sim 6$: Update on Quasar Luminosity Function at the Faint End with Subaru/Suprime-Cam*, *Astrophys J Lett* **847**, L15 (2017) L15, arXiv: 1709.04413 (cit. on pp. 64, 86).
- [308] G. Kulkarni et al., *Large 21-cm signals from AGN-dominated reionization*, *Mon Not R Astron Soc* **469** (2017) 4283, arXiv: 1701.04408 (cit. on pp. 64, 86).
- [309] Y. Qin et al., *Dark-ages reionization and galaxy formation simulation - X. The small contribution of quasars to reionization*, *Mon Not R Astron Soc* **472** (2017) 2009, arXiv: 1703.04895 (cit. on pp. 64, 86).
- [310] S. Mitra, T. R. Choudhury and A. Ferrara, *Cosmic reionization after Planck II: contribution from quasars*, *Mon Not R Astron Soc* **473** (2018) 1416, arXiv: 1606.02719 (cit. on pp. 64, 86).
- [311] S. Hassan et al., *Constraining the contribution of active galactic nuclei to reionization*, *Mon Not R Astron Soc* **473** (2018) 227, arXiv: 1705.05398 (cit. on pp. 64, 86).
- [312] M. Compostella, S. Cantalupo and C. Porciani, *The imprint of inhomogeneous He II reionization on the H I and He II Ly α forest*, *Mon Not R Astron Soc* **435** (2013) 3169, arXiv: 1306.5745 (cit. on pp. 64, 65, 68).

-
- [313] E. Bertschinger, *Multiscale Gaussian Random Fields and Their Application to Cosmological Simulations*, *Astrophys J Suppl Ser* **137** (2001) 1, eprint: astro-ph/0103301 (cit. on p. 65).
- [314] D. J. Eisenstein and P. Hut, *HOP: A New Group-Finding Algorithm for N-Body Simulations*, *Astrophys J* **498** (1998) 137, eprint: astro-ph/9712200 (cit. on p. 65).
- [315] A. Jenkins et al., *The mass function of dark matter haloes*, *Mon Not R Astron Soc* **321** (2001) 372, eprint: astro-ph/0005260 (cit. on p. 65).
- [316] J. Silk and M. J. Rees, *Quasars and galaxy formation*, *Astron Astrophys* **331** (1998) L1, eprint: astro-ph/9801013 (cit. on p. 65).
- [317] J. S. B. Wyithe and A. Loeb, *A Physical Model for the Luminosity Function of High-Redshift Quasars*, *Astrophys J* **581** (2002) 886, eprint: astro-ph/0206154 (cit. on p. 65).
- [318] M. Volonteri and M. J. Rees, *Quasars at $z=6$: The Survival of the Fittest*, *Astrophys J* **650** (2006) 669, eprint: astro-ph/0607093 (cit. on p. 65).
- [319] S. Kim et al., *The Environments of High-Redshift Quasi-Stellar Objects*, *Astrophys J* **695** (2009) 809, arXiv: 0805.1412 (cit. on p. 65).
- [320] S. Cantalupo, S. J. Lilly and M. G. Haehnelt, *Detection of dark galaxies and circum-galactic filaments fluorescently illuminated by a quasar at $z = 2.4$* , *Mon Not R Astron Soc* **425** (2012) 1992, arXiv: 1204.5753 (cit. on pp. 65, 66).
- [321] L. Morselli et al., *Primordial environment of super massive black holes: large-scale galaxy overdensities around $z \sim 6$ quasars with LBT*, *Astron Astrophys* **568**, A1 (2014) A1, arXiv: 1406.3961 (cit. on p. 65).
- [322] K. Ota et al., *Large-scale Environment of a $z = 6.61$ Luminous Quasar Probed by Ly α Emitters and Lyman Break Galaxies*, *Astrophys J* **856**, 109 (2018) 109, arXiv: 1802.08912 (cit. on p. 65).
- [323] M. Onoue et al., *Enhancement of galaxy overdensity around quasar pairs at $z < 3.6$ based on the Hyper Suprime-Cam Subaru Strategic Program Survey*, *Pub Astron Soc Japan* **70**, S31 (2018) S31, arXiv: 1704.06051 (cit. on p. 65).
- [324] E. Bañados et al., *The Galaxy Environment of a QSO at $z \sim 5.7$* , *Astrophys J* **773**, 178 (2013) 178, arXiv: 1306.6642 [astro-ph.CO] (cit. on p. 65).
- [325] N. Fanidakis et al., *The most luminous quasars do not live in the most massive dark matter haloes at any redshift*, *Mon Not R Astron Soc* **436** (2013) 315, arXiv: 1305.2199 (cit. on p. 65).
- [326] C. Mazzucchelli et al., *No Overdensity of Lyman-Alpha Emitting Galaxies around a Quasar at $z \sim 5.7$* , *Astrophys J* **834**, 83 (2017) 83, arXiv: 1611.02870 (cit. on p. 65).
- [327] P. Jakobsen et al., *Caught in the act: A helium-reionizing quasar near the line of sight to Q0302-003*, *Astron Astrophys* **397** (2003) 891, eprint: astro-ph/0211035 (cit. on p. 66).
- [328] P. Martini, *QSO Lifetimes, Coevolution of Black Holes and Galaxies* (2004) 169, eprint: astro-ph/0304009 (cit. on p. 66).

- [329] C. Porciani, M. Magliocchetti and P. Norberg,
Cosmic evolution of quasar clustering: implications for the host haloes,
Mon Not R Astron Soc **355** (2004) 1010, eprint: astro-ph/0406036 (cit. on p. 66).
- [330] S. Cantalupo, S. J. Lilly and C. Porciani,
Plausible Fluorescent Ly α Emitters around the $z = 3.1$ QSO 0420-388,
Astrophys J **657** (2007) 135, eprint: astro-ph/0611449 (cit. on p. 66).
- [331] G. Worseck et al.,
The transverse proximity effect in spectral hardness on the line of sight towards HE 2347-4342,
Astron Astrophys **473** (2007) 805, arXiv: 0704.0187 (cit. on p. 66).
- [332] B. C. Kelly et al., *Constraints on Black Hole Growth, Quasar Lifetimes, and Eddington Ratio Distributions from the SDSS Broad-line Quasar Black Hole Mass Function*,
Astrophys J **719** (2010) 1315, arXiv: 1006.3561 (cit. on p. 66).
- [333] J. S. Bolton et al., *Improved measurements of the intergalactic medium temperature around quasars: possible evidence for the initial stages of He II reionization at $z \simeq 6$* ,
Mon Not R Astron Soc **419** (2012) 2880, arXiv: 1110.0539 (cit. on p. 66).
- [334] R. Trainor and C. C. Steidel,
Constraints on Hyperluminous QSO Lifetimes via Fluorescent Ly α Emitters at $z = 2.7$,
Astrophys J Lett **775**, L3 (2013) L3, arXiv: 1308.1678 (cit. on p. 66).
- [335] E. Borisova et al., *Constraining the Lifetime and Opening Angle of Quasars using Fluorescent Lyman α Emission: The Case of Q0420-388*,
Astrophys J **830**, 120 (2016) 120, arXiv: 1510.00029 (cit. on p. 66).
- [336] T. M. Schmidt et al., *Statistical Detection of the He II Transverse Proximity Effect: Evidence for Sustained Quasar Activity for > 25 Million Years*,
Astrophys J **847**, 81 (2017) 81, arXiv: 1701.08769 (cit. on p. 66).
- [337] E. Lusso et al., *The first ultraviolet quasar-stacked spectrum at $z \simeq 2.4$ from WFC3*,
Mon Not R Astron Soc **449** (2015) 4204, arXiv: 1503.02075 (cit. on p. 67).
- [338] J. M. Shull and M. E. van Steenberg,
X-ray secondary heating and ionization in quasar emission-line clouds,
Astrophys J **298** (1985) 268 (cit. on p. 67).
- [339] M. McQuinn et al., *He II Reionization and its Effect on the Intergalactic Medium*,
Astrophys J **694** (2009) 842, arXiv: 0807.2799 (cit. on pp. 67, 68).
- [340] K. Kakiichi et al., *The concerted impact of galaxies and QSOs on the ionization and thermal state of the intergalactic medium*,
Mon Not R Astron Soc **468** (2017) 3718, arXiv: 1607.07744 (cit. on p. 67).
- [341] Z. Haiman and R. Cen, “Probing the End of the Dark Age: Quasar Strömgren Spheres Before Cosmological Reionization”, *The Physics of Galaxy Formation*,
ed. by M. Umemura and H. Susa, vol. 222,
Astronomical Society of the Pacific Conference Series, 2001 101 (cit. on p. 67).
- [342] N. Y. Gnedin, *Cosmic Reionization on Computers. I. Design and Calibration of Simulations*,
Astrophys J **793**, 29 (2014) 29, arXiv: 1403.4245 (cit. on p. 68).
- [343] P. Ocvirk et al., *Cosmic Dawn (CoDa): the First Radiation-Hydrodynamics Simulation of Reionization and Galaxy Formation in the Local Universe*,
Mon Not R Astron Soc **463** (2016) 1462, arXiv: 1511.00011 (cit. on p. 68).

-
- [344] D. Aubert, N. Deparis and P. Ocvirk,
EMMA: an adaptive mesh refinement cosmological simulation code with radiative transfer,
Mon Not R Astron Soc **454** (2015) 1012, arXiv: 1508.07888 [astro-ph.IM] (cit. on p. 68).
- [345] A. H. Pawlik et al.,
The Aurora radiation-hydrodynamical simulations of reionization: calibration and first results,
Mon Not R Astron Soc **466** (2017) 960, arXiv: 1603.00034 (cit. on p. 68).
- [346] P. Paschos et al., *Late Reheating of the IGM by Quasars: A Radiation Hydrodynamical Simulation of Helium II Reionization*, ArXiv e-prints (2007), arXiv: 0711.1904 (cit. on p. 68).
- [347] A. Rahmati et al.,
On the evolution of the H I column density distribution in cosmological simulations,
Mon Not R Astron Soc **430** (2013) 2427, arXiv: 1210.7808 [astro-ph.CO] (cit. on p. 68).
- [348] A. Bauer et al., *Hydrogen reionization in the Illustris universe*,
Mon Not R Astron Soc **453** (2015) 3593, arXiv: 1503.00734 (cit. on p. 68).
- [349] K. Kakiichi et al., *Ly α -emitting galaxies as a probe of reionization: large-scale bubble morphology and small-scale absorbers*, Mon Not R Astron Soc **463** (2016) 4019,
arXiv: 1510.05647 (cit. on p. 68).
- [350] A. Meiksin and E. R. Tittley,
The impact of helium reionization on the structure of the intergalactic medium,
Mon Not R Astron Soc **423** (2012) 7, arXiv: 1109.5037 (cit. on pp. 68, 81).
- [351] M. McQuinn et al., *Studying reionization with Ly α emitters*,
Mon Not R Astron Soc **381** (2007) 75, arXiv: 0704.2239 (cit. on p. 71).
- [352] K. Ota et al., *Reionization and Galaxy Evolution Probed by $z = 7$ Ly α Emitters*,
Astrophys J **677**, 12-26 (2008) 12, arXiv: 0707.1561 (cit. on p. 71).
- [353] D. J. Mortlock et al., *A luminous quasar at a redshift of $z = 7.085$* , Nature **474** (2011) 616,
arXiv: 1106.6088 [astro-ph.CO] (cit. on p. 71).
- [354] Y. Ono et al., *Spectroscopic Confirmation of Three z -dropout Galaxies at $z = 6.844$ - 7.213 : Demographics of Ly α Emission in $z \sim 7$ Galaxies*, Astrophys J **744**, 83 (2012) 83,
arXiv: 1107.3159 (cit. on p. 71).
- [355] B. E. Robertson et al.,
New Constraints on Cosmic Reionization from the 2012 Hubble Ultra Deep Field Campaign,
Astrophys J **768**, 71 (2013) 71, arXiv: 1301.1228 (cit. on p. 71).
- [356] V. Tilvi et al., *Rapid Decline of Ly α Emission toward the Reionization Era*,
Astrophys J **794**, 5 (2014) 5, arXiv: 1405.4869 (cit. on p. 71).
- [357] I. D. McGreer, A. Mesinger and V. D'Odorico,
Model-independent evidence in favour of an end to reionization by $z \approx 6$,
Mon Not R Astron Soc **447** (2015) 499, arXiv: 1411.5375 (cit. on p. 71).
- [358] E. Sobacchi and A. Mesinger,
The clustering of Lyman α emitters at $z \approx 7$: implications for reionization and host halo masses,
Mon Not R Astron Soc **453** (2015) 1843, arXiv: 1505.02787 (cit. on p. 71).
- [359] B. Greig et al.,
Are we witnessing the epoch of reionisation at $z = 7.1$ from the spectrum of J1120+0641?,
Mon Not R Astron Soc **466** (2017) 4239, arXiv: 1606.00441 (cit. on p. 71).

- [360] F. B. Davies et al., *Quantitative Constraints on the Reionization History from the IGM Damping Wing Signature in Two Quasars at $z > 7$* , *Astrophys J* **864**, 142 (2018) 142, arXiv: 1802.06066 (cit. on p. 71).
- [361] M. McQuinn and P. R. Upton Sanderbeck, *On the intergalactic temperature-density relation*, *Mon Not R Astron Soc* **456** (2016) 47, arXiv: 1505.07875 (cit. on p. 72).
- [362] J. Schaye et al., *The thermal history of the intergalactic medium*, *Mon Not R Astron Soc* **318** (2000) 817, eprint: astro-ph/9912432 (cit. on p. 72).
- [363] J. S. Bolton et al.,
A first direct measurement of the intergalactic medium temperature around a quasar at $z = 6$, *Mon Not R Astron Soc* **406** (2010) 612, arXiv: 1001.3415 (cit. on p. 72).
- [364] G. D. Becker et al.,
Detection of extended He II reionization in the temperature evolution of the intergalactic medium, *Mon Not R Astron Soc* **410** (2011) 1096, arXiv: 1008.2622 (cit. on p. 72).
- [365] A. Garzilli et al., *The intergalactic medium thermal history at redshift $z = 1.7 - 3.2$ from the Ly α forest: a comparison of measurements using wavelets and the flux distribution*, *Mon Not R Astron Soc* **424** (2012) 1723, arXiv: 1202.3577 (cit. on p. 72).
- [366] J. S. Bolton et al.,
A consistent determination of the temperature of the intergalactic medium at redshift $z = 2.4$, *Mon Not R Astron Soc* **438** (2014) 2499, arXiv: 1308.4411 (cit. on p. 72).
- [367] E. Boera et al., *The thermal history of the intergalactic medium down to redshift $z = 1.5$: a new curvature measurement*, *Mon Not R Astron Soc* **441** (2014) 1916, arXiv: 1404.1083 (cit. on p. 72).
- [368] A. Lidz and M. Malloy,
On Modeling and Measuring the Temperature of the $z \sim 5$ Intergalactic Medium, *Astrophys J* **788**, 175 (2014) 175, arXiv: 1403.6350 (cit. on p. 72).
- [369] A. Rorai et al., *A new measurement of the intergalactic temperature at $z \sim 2.55 - 2.95$* , *Mon Not R Astron Soc* **474** (2018) 2871, arXiv: 1711.00930 (cit. on p. 72).
- [370] E. Boera et al., *Revealing reionization with the thermal history of the intergalactic medium: new constraints from the Lyman- α flux power spectrum*, ArXiv e-prints (2018), arXiv: 1809.06980 (cit. on p. 72).
- [371] H. Hiss et al.,
A New Measurement of the Temperature-density Relation of the IGM from Voigt Profile Fitting, *Astrophys J* **865**, 42 (2018) 42, arXiv: 1710.00700 (cit. on p. 72).
- [372] M. Walther et al.,
New Constraints on IGM Thermal Evolution from the Ly α Forest Power Spectrum, ArXiv e-prints (2018), arXiv: 1808.04367 (cit. on p. 72).
- [373] S. Gallerani et al., *Glimpsing through the high-redshift neutral hydrogen fog*, *Mon Not R Astron Soc* **386** (2008) 359, arXiv: 0706.1053 (cit. on p. 77).
- [374] D. Syphers and J. M. Shull, *Hubble Space Telescope/Cosmic Origins Spectrograph Observations of the Quasar Q0302-003: Probing the He II Reionization Epoch and QSO Proximity Effects*, *Astrophys J* **784**, 42 (2014) 42 (cit. on p. 81).

-
- [375] G. Kulkarni, G. Worseck and J. F. Hennawi,
Evolution of the AGN UV luminosity function from redshift 7.5, ArXiv e-prints (2018),
arXiv: 1807.09774 (cit. on p. 87).
- [376] J. D. Hunter, *Matplotlib: A 2D graphics environment*,
Computing In Science & Engineering **9** (2007) 90 (cit. on p. 119).
- [377] S. v. d. Walt, S. C. Colbert and G. Varoquaux,
The NumPy array: a structure for efficient numerical computation,
Computing in Science & Engineering **13** (2011) 22 (cit. on p. 119).
- [378] F. Pedregosa et al., *Scikit-learn: Machine learning in Python*,
Journal of Machine Learning Research **12** (2011) 2825 (cit. on p. 119).
- [379] E. Jones, T. Oliphant, P. Peterson et al., *SciPy: Open source scientific tools for Python*,
[Online; accessed <today>], 2001, URL: <http://www.scipy.org/> (cit. on p. 119).
- [380] M. J. Turk et al., *yt: A Multi-code Analysis Toolkit for Astrophysical Simulation Data*,
The Astrophysical Journal Supplement Series **192**, 9 (2011) 9,
arXiv: 1011.3514 [astro-ph.IM] (cit. on p. 119).

List of Figures

1.1	Map of the cosmic microwave background as reconstructed by the <i>Planck</i> satellite . . .	2
1.2	Evolution of baryon, radiation and dark energy density across cosmic time	7
1.3	Galactic rotation curve from MOND and Λ CDM	8
1.4	Simulated dark matter density and galaxy distribution	11
1.5	Evolution of the linear power spectrum and assembly bias signal	12
1.6	High-redshift quasar spectra from SDSS	15
1.7	Effective optical depth of HI and HeII	17
1.8	Constraints on the average neutral hydrogen fraction across cosmic time	18
1.9	Peano-Hilbert space-filling curve and AMR structure	20
1.10	Nested initial conditions	26
2.1	Dark-matter, gas and stellar distributions in one ZOMG simulation	31
2.2	Evolution of distance, mass and radial phase space of two satellites	34
2.3	Radial phase space distribution at $z = 0$ of satellite particles	35
2.4	Uninvolved and evolved cumulative subhalo mass functions	39
2.5	Radial distributions of substructures and matter	40
2.6	Baryonic Tully-Fisher relation for the ZOMG subhaloes	41
2.7	1D stellar velocity dispersion and stellar mass fraction	42
2.8	Mass fraction locked in resolved substructures	43
2.9	Substructure accretion time distribution	43
2.10	Substructure trajectories	44
2.11	Probability density function of normalized radial velocities	46
2.12	Anisotropy parameter of the Milky Way, simulated haloes and Milky Way-like objects	47
2.13	Satellite orbital angular momentum projection	50
2.14	Satellite angular position at accretion and accretion time distribution	51
2.15	Alignment, planarity and distance for L -clusters satellites	52
3.1	Observed and simulated satellites in the RAR plane	57
3.2	Likelihood of the RAR parameters	58
3.3	Evolution of the RAR parameters	59
3.4	Evolutionary tracks of the RAR, total mass, stellar mass and radius of satellites	61
4.1	Quasar luminosity function	66
4.2	Overdensity, temperature, and ionised fractions of a slice through the simulation box	69
4.3	Volume rendering of the ionization front	70
4.4	Ionized fraction evolution in the quasar-dominated model	71
4.5	Thomson optical depth in the quasar-dominated model	72
4.6	IGM temperature at mean density evolution in the quasar-dominated model	73
4.7	HI effective optical depth evolution	74

List of Figures

4.8	HeII effective optical depth evolution	75
4.9	Cumulative distribution of HI effective optical depth	76
4.10	Shape properties of the HI Lyman- α forest	78
4.11	Shape properties of the HeII Lyman- α forest	79
4.12	Fraction of dark gaps and flux transmission windows in the Lyman- α forest	80
4.13	Column-density ratio evolution	81

List of Tables

2.1	Properties of the ZOMG haloes at $z = 0$	32
2.2	Spatial flatness of substructure groups	49

Acknowledgements

This Thesis is the culmination of a long – and somewhat troubled – journey, and many people deserve to be mentioned here.

First and foremost, I wish to thank my life partner Lisa, that selflessly encouraged me to pursue my dreams and has since shared with me the costs of a long-distance relation.

This journey would not have been possible without my family, that gave me the freedom to find my way, never failed to support my decisions and cultivated my interest in science. For this, I wish to wholeheartedly thank them. I want to explicitly thank my sister Alice, for keeping alive my inner child.

I would be ungrateful if I did not mention here my uncle Andrea and the Italian astrophysicist Margherita Hack, that sparked in me the curiosity for Nature, and my high-school teachers Federica Mazzilli and Neri Anna Grazia for their enthusiasm and stubbornness in teaching physics and math to a bunch of adolescents.

During the Ph.D. I met many people that, in a way or the other, shaped my path. I want to start by thanking my supervisor Cristiano Porciani, that has always been available to discuss, explain and help. I owe him a large share of the scientist I will be.

Emilio and Joseph, for once let me put all jokes aside. Work and life would have been much more boring and much harder without your friendship, and for this I will always be grateful to you.

A big thank goes to Mikolaj, Victoria and Rishi, that shared the office with me and have always been available – being it for a coffee or for a scientific discussion.

My gratitude goes also to the ‘lunch group’ – Carlo, Alberto, Lorenzo, Luca Bene and Luca Male – that transformed the lunch break in an amusing moment of my daily routine, and to the other Italians in Bonn – Alberto, Emiliano, Sara, Monica, Julia, Emilio, Giovanna, Elisabetta, Gabriele and Andrea – for bringing Italy a little closer.

Many other friends – Eugenio, Giacomo, Ana, Christos, Maitraiye, Devina, the 5B LST and many more – have been part of this journey in many different ways, and I wish to thank them all.

My scientific work would have not been possible without the help of countless individuals across the Globe that developed and maintain many open-source community software. In particular Matplotlib [376], NumPy [377], scikit-learn [378], SciPy [379] and yt [380].

Finally, I acknowledge the financial support I received through the SFB 956 ‘The Conditions and Impact of Star Formation’, sub-project C4 by the Deutsche Forschungsgemeinschaft (DFG), the International Max Planck Research School (IMPRS) for Astronomy and Astrophysics at the Universities of Bonn and Cologne and the Bonn-Cologne Graduate School (BCGS) of physics and astronomy.